STUDY OF COLOR COHERENCE EFFECTS IN $\overline{p}p$ COLLISIONS AT $\sqrt{s}$ = 1.8 TeV

A Dissertation

Submitted to the Graduate School

of the University of Notre Dame

in Partial Fulfillment of the Requirements

for the Degree of

Doctor of Philosophy

by

James J. Jaques, B.S., M.S.

Randal C. Ruchti, Director

Department of Physics

Notre Dame, Indiana

October, 1996

STUDY OF COLOR COHERENCE EFFECTS

IN $\overline{p}p$ COLLISIONS AT $\sqrt{s}$ = 1.8 TeV

Abstract

by

James J. Jaques

Particle distribution patterns are measured in W+jets events using calorimeter tower information as a means of studying color coherence effects in $p\overline{p}$ interactions. Angular distributions of towers with E_T>250 MeV around both the W and the leading jet in these events are measured and compared with similar distributions from PYTHIA W+jets simulations with various color coherence implementations. Color interference effects are observed in the data as determined by the agreement with PYTHIA simulations with full interference implementation.

To my wife, Kelly

TABLE OF CONTENTS

LIST OF FIGURES vii

LIST OF TABLES xv

ACKNOWLEDGEMENTS xvi

1 INTRODUCTORY DISCUSSIONS 1

1.1 Order from Chaos - The Eightfold Way and the Quark Model . 1

1.2 The Standard Model 4

1.3 Introduction to Quantum Chromodynamics 5

1.3.1 Group Representation 8

1.3.2 The QCD Lagrangian 9

1.3.3 Renormalization and the Running Coupling Constant . . 10

1.4 Introduction to Color Coherence 12

1.5 Introduction to the Analysis 13

1.5.1 Previous Experiments 15

1.5.2 W+jets as a Probe of Color Coherence 17

2 THEORETICAL OVERVIEW OF COLOR COHERENCE 20

2.1 Soft Gluon Emission in Hadronic Scattering 20

2.2 Color Flow Pattern in Leading Order $W + Jet$ Processes 24

2.3 Angular Ordering Approximation 32

2.4 Nonperturbative Effects 35

2.4.1 String Fragmentation 36

2.4.2 Independent Fragmentation 40

2.5 Monte Carlo Simulation 41

2.6 Color Coherence Study 43

3 THE TEVATRON AND THE DØ DETECTOR 45

3.1 The Fermilab Tevatron 45

3.2 Coordinate Systems 48
3.3 The DØ Detector 50
3.4 Tracker 52
3.4.1 Vertex Drift Chamber (VTX) 52
3.4.2 Transition Radiation Detector (TRD) 54
3.4.3 Central Drift Chamber (CDC) 55
3.4.4 Forward Drift Chambers (FDC) 57
3.5 Calorimeter 58
3.5.1 Calorimeter Structure 63
3.5.2 Central Calorimeter (CC) 64
3.5.3 Endcap Calorimeters (EC) 66
3.5.4 Intercryostat Detector (ICD) and Massless Gap (MG) . . 67
3.5.5 Calorimeter Readout 69
3.5.6 Calorimeter Performance 69
3.6 Muon System 71
3.7 Data Acquisition 73
3.7.1 Level 0 73
3.7.2 Level 1 75
3.7.3 Level 2 76

4 ACQUIRING THE DATA SETS 77
4.1 The W Decay Mode Selection 77
4.2 Offline Reconstruction and Streaming 79
4.2.1 Jet Reconstruction 79
4.2.2 Electron Reconstruction 81
4.2.3 Missing E_T 82
4.2.4 Streaming the Data 84
4.3 The $W + jets$ Data Set 85
4.3.1 Main Ring Contamination 85
4.3.2 Jet Quality Cuts 88
4.3.3 Electron Quality Cuts 90
4.3.4 $\not{E}_T$ Cut 94
4.3.5 W Reconstruction 95
4.4 Analysis Requirements 96
4.4.1 Multiple Interactions 96

4.4.2 W Boson Transverse Momentum 99
4.4.3 Vertex Position 99
4.4.4 W-Jet Azimuthal Correlation 100
4.4.5 Rapidity Restriction 101
4.5 Summary 102

5 CORRECTIONS TO THE DATA 104
5.1 Pedestal Offsets 104
5.1.1 Pileup Energy 105
5.1.2 Luminosity Dependence 106
5.1.3 Pileup Correction 107
5.2 Zero Suppression 109
5.2.1 Zero Suppression Correction 110
5.3 Combined Results 111
5.4 Offset Vertex Correction 112

6 ANALYSIS OF THE DATA 114
6.1 Overview 114
6.2 Construction of the Variables 114
6.2.1 Particles in the Calorimeter 114
6.2.2 Annular Regions 117
6.2.3 The β Variable 120
6.2.4 The β Distribution 121
6.3 Results from Data 123
6.3.1 Minimum Bias Comparison 127
6.4 PYTHIA Monte Carlo Simulation 130
6.4.1 Detector Simulation 131
6.5 Analysis of PYTHIA Events 134
6.5.1 Kinematic Comparison with Data 134
6.5.2 Calorimeter noise 135
6.6 Results from PYTHIA 137
6.6.1 Particle-Level Measurement 139
6.6.2 Particle-Calorimeter Comparison 143
6.7 Color Coherence in the Collider Data 143
6.8 Threshold Dependence 146

6.9 Systematic Uncertainties 149
6.9.1 Background Contamination 150
6.9.2 Pileup and Zero Suppression 153
6.9.3 Calorimeter Response 154
6.9.4 Luminosity Dependence 156
6.9.5 W Boson Rapidity 159
6.9.6 Summary of Systematics 161

7 SUMMARY AND CONCLUSION 162

A Useful Kinematic Quantities for W Bosons 167
A.1 Transverse Mass 167
A.2 Transverse Momentum 167
A.3 Azimuthal Angle 167
A.4 Rapidity 168

B A Sample W+jets Event in the Detector 170

C Post-Mortem Analysis 174
C.1 Comparison of Data and PYTHIA 174
C.2 Minimum Bias Dijet Events 175

BIBLIOGRAPHY 179

LIST OF FIGURES

1.1 Baryon octets 2

1.2 Modified baryon octets 4

1.3 Feynman/color flow diagrams for $q\overline{q}\rightarrow q\overline{q}$ 12

1.4 Angular ordering 14

1.5 e^+e^- color flow 15

1.6 Diagrams for $W + jet$ production 17

1.7 Color flow in $W + jet$ events 18

2.1 Emission cone around parton i as defined by partons i and j. Maximum probability for emission from parton i occurs when gluon is radiated between i and j. 24

2.2 a) Feynman diagram and b) color flow diagram for $q\overline{q}\rightarrow Wg$ . . 25

2.3 Orientation of $q\bar{q} \rightarrow Wg$ event for calculation of $\mathbf{P}(E_{g'}, \Omega)$ . . . 27

2.4 Soft gluon radiation pattern $(E^2_{T(g')}/N_c)\mathbf{P}(\Omega)$ around the gluon jet for the process $q\overline{q}\rightarrow Wg$ with $\eta_{Jet} = 0.0$. 28

2.5 Soft gluon radiation pattern $(E^2_{T(g')}/N_c)\mathbf{P}(\Omega)$ around the W boson for the process $q\overline{q}\rightarrow Wg$ reaction with $\eta_W = 0.0$. 29

2.6 Soft gluon radiation pattern $(E^2_{T(g')}/N_c)\mathbf{P}(\Omega)$ around the gluon jet for the process $qg \rightarrow Wq$ reaction with $\eta_{Jet} = 0.0$ 31

2.7 Soft gluon radiation pattern $(E^2_{T(g')}/N_c)\mathbf{P}(\Omega)$ around the W boson for the process $qg \rightarrow Wq$ reaction with $\eta_W = 0.0$ 32

2.8 Example of angular ordering of successive gluon branchings. . . 34

2.9 Description of color string stretched between a separating $q\overline{q}$ pair. A string break is shown in the middle accompanied by the production of a new $q\overline{q}$ pair. 37

2.10 Hadron formation from a chain of quark-antiquark pairs created along a $u\overline{u}$ color string. 38

2.11 Visual description of String model. One-dimensional string spans all color-connected partons following cascade process from a $q\overline{q}$ pair. The light gray circles represent a $q\overline{q}$ pair being pulled from the vacuum along a string. 39

3.1 Fermilab accelerator complex 46

3.2 Overview of the DØ detector 51

3.3 DØ Tracking System 52

3.4 FDC chambers 57

3.5 The DØ calorimeter 59

3.6 Unit calorimeter cell 60

3.7 Calorimeter towers 64

3.8 The DØ muon system 72

4.1 E_T near Main Ring 88

4.2 Electron E_T distribution for candidate W boson events from the HLP stream. 90

4.3 Missing E_T distribution for candidate W boson events from the HLP stream. 95

4.4 W boson transverse mass distribution for all events in which a W could be reconstructed. The lines at 45 GeV/c^2 and 105 GeV/c^2 represent the M_T^W restrictions on the data. 96

4.5 a) Distribution of MI Flag values for surviving event candidates. b) Average MI Flag value as a function of $\mathcal{L}$. 99

4.6 Distribution of p_T^W in $W + jets$ events, after the 10 GeV/c cut. . 100

4.7 Mismatch between physics η and detector η as a function of z component of the event vertex for $\mid z_{vertex} \mid < 90$ cm. Differences are plotted for $\eta_{det} = 0.0$ and $\eta_{det} = 3.0$ for comparison. 101

4.8 Azimuthal separation of W boson and tagged jet in W+jets events. Note the strong peak at π, which is represents the kinematically most probable configuration, even in the absence of a tight back-to-back restriction. 102

5.1 Pedestal energies 109

5.2 Corrected Data 112

6.1 Residual tower energy from zero bias data for all towers in a)the Central Calorimeter and b)the Endcap Calorimeters. 116

6.2 Kinematics and variables relevant for energy flow analysis 118

6.3 Distribution of $\Delta\phi_{Jet,W}$ separation in $W + Jets$ sample. The distribution peaks at π, but extends out to the limits imposed on the data of $\pi/2$ and $3\pi/2$. 120

6.4 Calorimeter view of energy flow variables 122

6.5 Number of towers above 250 MeV E_T threshold, normalized to the total number of towers, for a) the tagged jet region, and b) the W boson region. These plots are averaged over the whole analysis sample. 124

6.6 Division of jet and W patterns, illuminating differences in energetic tower distributions as a function of the angular variable β. 125

6.7 Rapidity difference between W boson and jet. Negative entries indicate events in which the tagged jet is more forward than the W boson, while positive entries signify events in which the W boson is more forward. 126

6.8 Hard (a) and soft (b) $\overline{p}p$ scattering. 128

6.9 a)Distribution of $\Delta\phi$ for the W boson and jet for W+jets (solid line) and fake W+jets locations from min bias (dashed line) data. b)Distribution of $\mid y_W \mid - |\eta_{Jet}|$ for W+jets (solid) and min bias (dashed) data. Negative values in second plot indicate events in which the tagged jet was more forward than the W boson, and vice versa for positive values. 129

6.10 Distribution of towers above threshold around the tagged jet divided by the distribution around the W boson in W+jets data (open circles) as compared to the distribution of towers above threshold around the "jet" divided by the distribution around the "W" in min bias data (closed circles). 130

6.11 Schematic depiction of layer structure in IETA of calorimeter towers (1/2 of detector shown). 133

6.12 Comparisons of data (solid line) with Monte Carlo events (dashed line) for **a)**Electron E_T, **b)**$\not{E}_T$, **c)**Tagged jet η, and **d)**W boson rapidity. 135

6.13 Comparisons of data (solid line) with Monte Carlo events (dashed line) for **a)**Azimuthal separation of W boson and tagged jet, **b)**Rapidity separation of W boson and tagged jet, **c)**W boson p_T, and **d)**Tagged jet E_T. 136

6.14 Comparisons of data (solid line) with Monte Carlo events (dashed line) after new tagged jet E_T cut for **a)**W boson p_T and **b)**tagged jet E_T. 137

6.15 Divisional β distribution for PYTHIA samples – a)**Sample I** (angular ordering and string fragmentation), b)**Sample II** (no angular ordering, but still with string fragmentation), c)**Sample III** (no angular ordering and independent fragmentation), and d)**All** samples overlayed. 138

6.16 E_T distribution for a)all particles and b)particles with a matched tower above 250 MeV in E_T. 140

6.17 Distribution of particles with E_T>500 MeV for all three PYTHIA samples. 141

6.18 Distribution of particles for various E_T cuts in Sample I. 142

6.19 Comparison of particle-level β distributions (closed circles) and Shower Library β distributions (open circles) for a) Sample I, b)Sample II, and c)Sample III. All distributions are normalized to equal area. 144

6.20 Energetic tower distribution in data with new changes (closed circles) and without new changes (open circles). 145

6.21 Comparison of normalized β distributions for data and PYTHIA Sample I (angular ordering and string fragmentation). 146
6.22 Comparison of normalized β distributions for data and PYTHIA Sample II (no angular ordering, but with string fragmentation). 147
6.23 Comparison of normalized β distributions for data and PYTHIA Sample III (no angular ordering and independent fragmentation).148
6.24 Variation in β distribution for tower E_T thresholds of a)0 MeV to 150 MeV and b)200 MeV to 350 MeV. 149
6.25 Variation in β distribution for tower E_T thresholds of 0 MeV, 150 MeV, and 250 MeV in Sample I from PYTHIA. 149
6.26 Example of fake W boson reconstruction from a dijet event in the ϕ plane (beam direction perpendicular to page). 151
6.27 Distribution in β of simulated background sample. 153
6.28 Effect of approximated background subtraction in β measurement.153
6.29 β distribution for nominal pedestal offset and zero suppression corrections compared with a)$\pm$50% in the pedestal offset correction and b)$\pm$50% in the zero suppression (ZSP) correction. . . . 154
6.30 β distribution with nominal calorimeter response compared with distribution with corrective factors for a)Data and b)PYTHIA Sample I (Samples II and III give similar results). 155
6.31 Dependence of the signal in data on event luminosity. 157
6.32 Dependence of the signal in data on event luminosity, second comparison. 157

6.33 Comparisons with wider rapidity window. a)β distribution with rapidity window of ± 0.5 (closed circles) and ± 0.7 (open circles). b)Dependence of the signal on event luminosity for wider rapidity window. 158

6.34 β distribution from data for calculated W boson rapidity (open circles) and random W boson rapidity (closed circles). 160

6.35 β distribution for calculated W boson rapidity (open circles) and random W boson rapidity (closed circles) from a)PYTHIA Sample I and b)PYTHIA Sample II. 160

6.36 Comparison of data with a)PYTHIA Sample I and b)PYTHIA Sample II when the W boson rapidity is randomly generated. . 161

7.1 Divisional comparison of β measurements in data and PYTHIA with angular ordering (AO) and string fragmentation (SF). . . . 163

7.2 Divisional comparison of β measurements in data and PYTHIA without angular ordering, but with string fragmentation. 164

7.3 Divisional comparison of β measurements in data and PYTHIA without angular ordering and with independent fragmentation (IF). 164

B.1 Side view of event. 171

B.2 End view of event. 172

B.3 Calorimeter towers in (η,ϕ) plane. 173

C.1 Comparison of normalized β distributions for data and PYTHIA Sample I (angular ordering and string fragmentation) for the wider rapidity window. 175

C.2 Comparison of normalized β distributions for data and PYTHIA Sample II (no angular ordering, but with string fragmentation) for the wider rapidity window. 176

C.3 Comparison of normalized β distributions for data and PYTHIA Sample III (no angular ordering and independent fragmentation) for the wider rapidity window. 177

C.4 Divisional β distribution for W+jets data (closed circles) as compared to minimum bias dijet data (open squares). 178

LIST OF TABLES

1.1 Known elementary particles in the Standard Model and their electric charges. 6

3.1 Parameters for DØ Vertex Drift Chamber 53

3.2 Parameters for DØ Transition Radiation Detector 55

3.3 Parameters for DØ Central Drift Chamber 56

3.4 Parameters for DØ Forward Drift Chambers 58

3.5 Parameters for DØ Central Calorimeter 65

3.6 Parameters for DØ Endcap Calorimeters 68

3.7 Resolution parameters for some calorimeter modules 70

4.1 Summary of cuts used in acquiring W+jets events for the analysis 103

ACKNOWLEDGEMENTS

It is, of course, impossible to mention by name every person who contributed to the successful completion of this thesis. Literally hundreds of people, both within and outside of the collaboration, have supported this analysis and document in some way and I am grateful to you all. Although it is my name on this dissertation, its development over the years has been in every way a collaborative effort. With that in mind, however, there are several people which I would like to recognize here for their special efforts.

I first would like to thank my advisor, Randy Ruchti, who has assisted me both intellectually and financially during my time at Notre Dame. He taught me much about high energy physics in the classroom and introduced me to the work of a physicist in the lab. He further allowed me the freedom to pursue a risky thesis analysis and supported that analysis to the end. Randy has also been extremely generous with computing resources when I have needed them, and has spent much time with me in preparing talks for conferences and especially in preparing this document. In all, I have learned much and enjoyed my time in his tutelage, and I consider it an honor to have been his student. Thank you also to the rest of my thesis committee – Mitch Wayne, Nripen Biswas and Samir Bose, for reading the thesis and providing comments.

The person who worked with me the closest during the course of this analysis was Dr. Nikos Varelas, and I cannot possibly express my gratitude for

his presence. Nikos and I have worked together almost daily for the past two-and-a-half years struggling to make some sense of many, many strange–looking distributions. Together, we have sweated, argued, laughed and wrestled this analysis to completion. He has been my mentor at DØ as well as a friend and, more than anyone else, has taught me how to be an experimental physicist. My sincerest thanks, Nikos, for your unending support and wisdom, and for the occasional push from behind. I only regret that I caused you to lose a bit more hair than you otherwise would have.

I am also very grateful to my editorial board for their help in guiding this study through our bi–weekly meetings. Harry Melanson, Norman Graf, Sharon Hagopian, and Dave Cutts have always been patient and understanding, even when I showed up several minutes late and then presented "disturbing" results (both of which happened more times than I care to admit!). They consistently gave insightful comments and new perspectives and provided an amicable forum for me to discuss my latest successes and failures. I want to give special mention to Norman Graf, who went to great lengths to help me acquire my event samples and who was always willing to take the time to discuss anything from the analysis to my thesis to the weather in Rome in May.

There are several theorists whom I have been privileged to have contacted on many occasions concerning the finer (and not so fine) details of color interference. They are Bo Andersson, Brian Webber, Steve Ellis, David Soper, and especially the author of PYTHIA, Torbjörn Sjöstrand. Thank you all for allowing me to harrass you repeatedly.

Many thanks also to Jerry Blazey, who suggested this topic to me, helped me get it started over a period of several months, and then continued to offer advice and assistance when it was most needed. The rest of the QCD group

at DØ was also very helpful along the way, especially Harry Weerts, Andrew Brandt, Brad Abbott, Brent May, Freedy Nang, and Rob Snihur. Thanks for your suggestions and discussions.

There have been other colleagues at DØ who I have received help from as well. Tacy Joffe–Minor kindly estimated my background fraction for me. Steve Linn processed my Monte Carlo with plate–level GEANT. Jerry Guglielmo processed additional Monte Carlo with Shower Library. Joan Guida taught me volumes about the calorimeter and its high voltage system. Terry Geld and Alan Jonckheere took care of the many disks I stored data on and kept me sane when they repeatedly crashed. Jon Kotcher helped me develop my cell energy corrections.

My friend, neighbor, and partner in crime, David Cullen–Vidal, has been in the front seat with me during the roller coaster ride from the start. His color coherence study has helped me understand my own, and I hope the reverse has been true as well. I hope you finish soon, David, and I wish you all the best. Kelly and I have enjoyed spending time with you and Eneida, and we will miss you when we leave.

There have been other Oak Park neighbors who have been a large part of my life both at and away from Fermilab. Dylan Casey, his wife Brenda, and their son Simon have been the best friends I could have hoped for. Dylan has patiently listened to all my complaints, concerns, and questions about physics and the world in general during our long commute each day. We have had long conversations about our analyses over morning coffee, during dinners, and during many walks to Starbucks. He has become one of my closest friends over the past two years. I hope you and Brenda and Simon will remember us when we move to the land of Rude People. Thanks also to Gian Di Loreto for being

a friend and for proving that you can have fun while being a grad student. I hope you finish the noise correction before Run II. Kelly and I will miss you and Beth also.

I must also thank the rest of my friends at DØ for support and for giving me something to do other than work — Cary Yoshikawa, Tom Fahland, Freedy Nang, Bryan Lauer, Kathy Fatyga, Brad Abbott, Jadzia Warchol, and Oliver Bardon (see you in Boston!). Thank you to Bob Kehoe for everything as well.

I have had many other friends back at Notre Dame who deserve mention for making those gray South Bend winters almost bearable, especially Court Walpe and his wife, Amy. They are two reasons it will be hard to leave the Midwest. Court has been a good friend since we both started at Notre Dame. I will also miss my other friends in the Physics department and former roommates, Sydney Taegar and Ma'an Qazzaz. With the four of us and a couple of unusually entertaining cats, there was never a dull moment at University Park. I should also acknowledge the High Energy Physics secretary, Lesley Krueger, for always making sure I was registered and for kindly sending my check to me without fail. You saved my life more than once, Lesley.

Although it did not seem like it at times, I did have a life beyond the Physics community. Through the Notre Dame Martial Arts Institute and Billy Powell's Way of Kenpo dojo in Chicago, I have been able to pursue my second calling. I thank all of my former teachers and students at NDMAI for giving me an outlet for that passion (and occasionally for some frustrations, as well). In particular, I would like to recognize Sensei Denis McCarthy and Sensei Drew Sandler for understanding me as both a graduate student and a martial artist. Also following into this category are former students Jennifer Kovass and John Roussalis, who carried the Notre Dame club when I could not be there. Special

mention goes to Sensei Billy Powell, who taught me that today is a gift – that's why it's called the Present. Thank you Billy, for tearing down my illusions and showing me what is really important. Believe it or not, this thesis would not have been the same without you. Thank you also to the rest of my martial arts friends in Chicago and South Bend. I will be back regularly to throw you around.

I reserve separate mention among my martial arts colleagues for Sensei Jim Hoff and Sensei Jason Thomas. Both fellow graduate students, they provided friendship, sympathy, and plenty of bruises to make me forget about physics for a time. Thanks, Jim, for appreciating my analysis from the outside. Thanks, Jason, for giving me a place to stay in South Bend so many times.

I thank my parents for raising me to be curious and for giving me a sound work ethic. They have been a constant source of love and support. Thanks Mom and Dad, for having faith in me and for giving me such great examples to live up to.

Lastly, I wish to recognize the one person who did the most for me over the past few years. My wife, Kelly, has been my best friend and the person I leaned on the most as a graduate student, particularly while writing this thesis. She never complained when I worked late and on weekends, and she allowed me the freedom to concentrate on writing by taking care of virtually everything else in our lives. Thank you, Kelly, for your patience, love and kindness in dealing with me during this extremely stressful time. You should probably receive a psychology degree for your experience with my manic–depressive behavior as my signal disappeared and reappeared at least a hundred times. Your presence in my life has made this all worthwhile.

CHAPTER 1

INTRODUCTORY DISCUSSIONS

High energy particle physics concerns itself with the fundamental nature of matter. The challenge is to understand the particles that form the building blocks of matter and the forces that govern their interactions. The two complementary methods by which this understanding is advanced are the development of models that explain the existence of particles and their interactions, and the experimental verification (or disproval) of these models.

This dissertation is concerned with an experimental analysis of a model within particle physics. The model studied will be described in later sections. Preceding its introduction is a brief description of high energy particle physics.

1.1 Order from Chaos - The Eightfold Way and the Quark Model

In 1960, the field of particle physics was approaching maturity. Many particles had been discovered and had been loosely organized into groups based on their masses: leptons (electrons, muons, neutrinos), mesons (pions, kaons), and baryons (protons, neutrons). Mesons and baryons were further classified as hadrons, particles that can interact through the strong force. Yukawa had formulated a theory for strong interactions, describing it as the force that binds protons and neutrons to each other in an atomic nucleus and having influence only over a very short distance. However, there was no structured relationship

among the known particles except through the conserved quantum numbers (e.g. charge, lepton number, baryon number, strangeness[1]). Further, there was little justification for the mass groupings.

Much of this confusion was dispelled in 1961 with the introduction of the *Eightfold Way* by Gell-Mann and Ne'eman[1]. The Eightfold Way classified the known particles by arranging them in two-dimensional geometric patterns. One of these is shown in Fig. 1.1, the ground-state (s-wave) baryon octet.

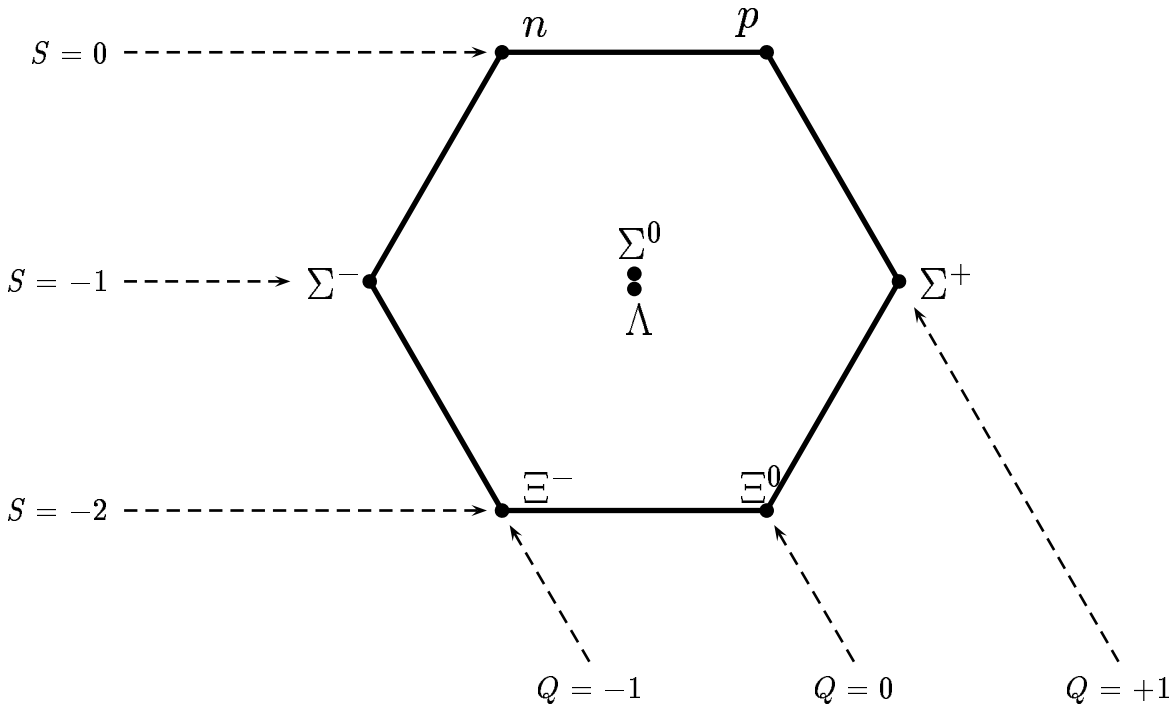

Figure 1.1. Baryon octet. Other representations exist for baryons and mesons, as well (e.g. baryon decuplet, meson nonet)

This configuration relates strangeness (S) and charge (Q) for the lightest baryons. Similar configurations were developed for the lightest mesons. Other

[1]Strangeness is a quantum number introduced by M. Gell-Mann in 1953 to describe particles that were produced via strong interactions, but decayed slowly through weak interactions (e.g. K mesons). Each such particle is assigned a strangeness of ± 1. Strangeness was found *not* to be conserved in weak interactions.

patterns existed also, such as the baryon decuplet for heavier baryons. The baryon decuplet, in fact, led Gell-Mann to predict the existence of the Ω^- which was found three years later[2].

The Eightfold Way did not, however, provide rationale for these geometric relationships among the hadrons. That reasoning came in 1964, from Gell-Mann[3] and Zwieg[4], with the Quark Model. They proposed that all hadrons were composites of more fundamental particles, which Gell-Mann termed quarks[2]. The Quark Model asserted that baryons were comprised of three quarks, antibaryons were comprised of three antiquarks, and mesons were made up of one quark and one antiquark. Three such quarks were theorized: the up (u), down (d), and strange (s) quarks. Each has fractional charge; $Q = -\frac{1}{3}$ for the d and s quarks and $Q = +\frac{2}{3}$ for the u quark (the charges are reversed for the antiquarks). Each quark has a baryon number (B) of $\frac{1}{3}$. The s quark also has strangeness $S = -1$, while the other two have $S = 0$. With this model in hand, the baryon octet created by the Eightfold Way can be reinterpreted in terms of quark constituency (see Fig. 1.2).

The Quark Model lacked experimental support until 1968, when experiments at the Stanford Linear Accelerator (SLAC) using e^-p collisions verified that the proton was a composite object and not a point particle. The term *parton* was used to identify the substructure, however, instead of quark, indicating some lack of confidence in the Quark Model. The discovery of the J/ψ particle[5][6] in 1975 led to the introduction of the *charm* (c) quark[3] into the model. With this new quark, the Quark Model predicted new baryons and mesons which would contain the charm quark. Many of these new states were

[2]The term *quark* comes from a line in James Joyce's novel *Finnegan's Wake*.

[3]The existence of the charm quark was actually proposed in 1964 by Bjorken and Glashow[7].

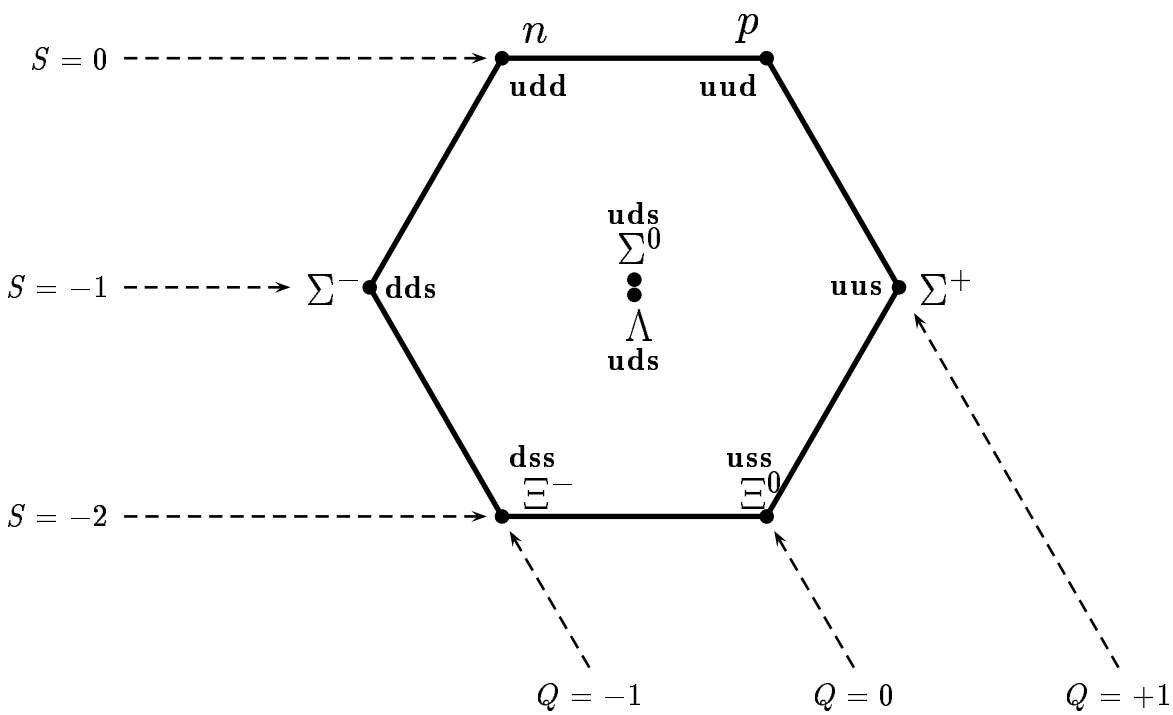

Figure 1.2. Modified baryon octet. Here, the quark composition for each baryon is shown with the baryon symbol. Notice that the number of s quarks scales with strangeness and the number of u quarks scales with charge

.

subsequently observed in the following years, providing further support for the Quark Model. Thus far, quarks have been observed only in bound state, not as free objects.

1.2 The Standard Model

In order to obtain a theory for weak interactions capable of finite calculations, it is necessary to have a model which contains the same number of quarks as leptons. In 1974, this was the case; there were four known quarks (u, d, s, and c) and four known leptons (e, ν_e, μ, and ν_μ). However, the observation of the τ lepton in 1975[8] destroyed this equilibrium. A fifth quark, the *bottom* (b), was

added to the mix in 1977 with the discovery of the upsilon particle, a bound state of a b and a $\bar{b}$. However, restoration of the desired quark-lepton symmetry had to wait until 1995, when the discovery of a sixth quark, the *top* (t) quark, was confirmed simultaneously by the DØ[11] and CDF[12] experiments after many years of searching.

Quarks and leptons interact with each other through four known fundamental forces: electromagnetic, strong, weak, and gravity. Interactions occur through the exchange of mediating *vector bosons.* The mediating bosons for the four forces are, respectively, the photon (γ), the gluon (g), the $W^{\pm}$ and Z bosons, and the graviton. The graviton has not been observed, and gravity has traditionally been ignored in the study of particle physics due to its extreme weakness ($\sim 10^{33}$ times weaker than the weak force). For reasons that will be discussed later, free gluons have never been directly observed, but substantial evidence supports their existence (such as the experimental observation of three-jet events in e^+e^- collisions at PETRA in 1979). The three weak bosons ($W^{\pm}$ and Z) were first observed at CERN in 1983[9][10].

This set of elementary particles and fundamental forces currently form the Standard Model for particle physics. The Standard Model describes all of the currently recognized elementary particles (quarks, leptons, and vector bosons) and their interactions. It also makes predictions for additional particles yet to be observed (such as the Higgs boson). The currently known members of the Standard Model are listed in Table 1.1.

1.3 Introduction to Quantum Chromodynamics

The quantum field theory describing strong interactions is called Quantum Chromodynamics (QCD). In direct analogy with Quantum Electrodynamics

Table 1.1. Known elementary particles in the Standard Model and their electric charges.

Quarks	Q	Leptons	Q
u	$+\frac{2}{3}$	e	-1
d	$-\frac{1}{3}$	ν_e	0
c	$+\frac{2}{3}$	μ	-1
s	$-\frac{1}{3}$	ν_μ	0
t	$+\frac{2}{3}$	τ	-1
b	$-\frac{1}{3}$	ν_τ	0
Bosons	**Q**		
γ	0		
g	0		
W^+	$+1$		
W^-	-1		
Z	0		

(QED), where charged particles interact through photon exchange, QCD describes quark interactions through the exchange of massless gluons, which are the charge carriers for the strong force. Unlike QED, which delineates two electromagnetic charges (positive and negative), QCD provides for *three* charges, called color, carried by both quarks and gluons in strong interactions. The quark color charges are named "red", "green", and "blue" [4]. Antiquarks carry anti-color charges; "anti-red", "anti-green", and "anti-blue". Gluons carry one color and one anti-color, in contrast with photons, which are uncharged. Like the electromagnetic charge, color charge is a conserved quantum number.

The color quantum number was postulated[13] to solve the spin-statistics problem created by the discovery of the Δ^{++} particle. The Δ^{++} is a baryon composed of three apparently identical u quarks, each with spin$=+\frac{1}{2}$, in an s-wave bound state. Such a state appears to violate the Pauli exclusion principle, whereby no fermions in the same state may have identical quantum numbers.

[4]This is nomenclature only. There is no connection with the visible light spectrum.

The invocation of the color quantum number, however, solves this problem by assigning each quark in the baryon a unique color charge. Quarks, then, can have any of three color charges - in the $SU(3)$ terminology of QCD, they are color triplets. Quark bound states (baryons and mesons), on the other hand, are required by theory to have no net color charge and to have completely symmetric wavefunctions with respect to color (i.e. they are color singlets). The quark configuration for the Δ^{++}, properly symmetrized, is written

$$\begin{aligned}\Delta^{++} = \frac{1}{\sqrt{6}}[&|\mathrm{u_R u_G u_B}\rangle + |\mathrm{u_B u_R u_G}\rangle + |\mathrm{u_G u_B u_R}\rangle \\ &-|\mathrm{u_G u_R u_B}\rangle - |\mathrm{u_B u_G u_R}\rangle - |\mathrm{u_R u_B u_G}\rangle]\end{aligned} \tag{1.1}$$

The existence of the quark color charge was supported by various experiments which measured quantities sensitive to color charge multiplicity. One such experiment was the measurement of the $\pi^o \to \gamma\gamma$ decay rate. The decay rate is given by (with $\hbar = c = 1$)

$$,(\pi^o \to \gamma\gamma) = (\frac{\alpha}{2\pi})[N_c(e_u^2 - e_d^2)]^2 \frac{M_\pi^3}{8\pi f_\pi} \tag{1.2}$$

where N_c is the number of colors, $e_{u,d}$ are the electromagnetic charges of the u and d quarks, M_π is the π^o mass, and f_π is the pion decay constant. For $N_c = 1$ and $N_c = 3$, the predicted decay rates are

$$\begin{aligned} ,(\pi^o \to \gamma\gamma) &= 0.86eV \quad (N_c = 1) \\ ,(\pi^o \to \gamma\gamma) &= 7.75eV \quad (N_c = 3) \end{aligned} \tag{1.3}$$

The measured[15] value is

$$, (\pi^o \rightarrow \gamma\gamma) = (7.86 \pm 0.54)eV, \tag{1.4}$$

which is in very good agreement with the $N_c = 3$ predicted rate.

1.3.1 Group Representation

In group theory terminology, QCD is represented by the group $SU(3)$. This group has three degrees of freedom, corresponding to the three colors. The generators of the group are eight linearly independent hermitian 3×3 matrices with determinant = 1, known as the Gell-Mann matrices. They are numbered λ_1,...,λ_8. Together with the color eigenvectors, they generate the eight gluon color states[16]:

$$\begin{array}{ll} \frac{1}{\sqrt{2}}(R\overline{B} + B\overline{R}) & \frac{-i}{\sqrt{2}}(R\overline{G} - G\overline{R}) \\ \frac{-i}{\sqrt{2}}(R\overline{B} - B\overline{R}) & \frac{1}{\sqrt{2}}(B\overline{G} + G\overline{B}) \\ \frac{1}{\sqrt{2}}(R\overline{R} - B\overline{B}) & \frac{-i}{\sqrt{2}}(B\overline{G} - G\overline{B}) \\ \frac{1}{\sqrt{2}}(R\overline{G} + G\overline{B}) & \frac{1}{\sqrt{6}}(R\overline{R} + B\overline{B} - 2G\overline{G}) \end{array} \tag{1.5}$$

These eight states form the color *octet* representation for gluons. Quarks can only be represented by the three colors (or three anticolors for antiquarks), and are therefore represented as color *triplets*. There is a ninth possible gluon state,

$$\frac{1}{\sqrt{3}}(R\overline{R} + B\overline{B} + G\overline{G}) \tag{1.6}$$

but this state is actually a color *singlet* and carries no net charge. It would thus not interact with any other particles through the strong force. Its existence is therefore not postulated in current QCD theory.

In general, the matrix generators of $SU(3)$ do not commute with each other. The commutation of any two $SU(3)$ generators can be represented by[17]

$$[\lambda_i, \lambda_j] = i \sum_k f_{ijk} \lambda_k \tag{1.7}$$

where f_{ijk} are constants of the group, called structure constants. Because of the anticommutation, QCD is known as a non-Abelian theory. This feature has direct physical consequences in QCD, which can be seen in the evaluation of the QCD Lagrangian.

1.3.2 The QCD Lagrangian

The full QCD Lagrangian can be written[17]

$$\mathcal{L} = \bar{q}(i\gamma^\mu \partial_\mu - m)q - g(\bar{q}\gamma^\mu \frac{\lambda_a}{2} q)G^a_\mu - \frac{1}{4} G^a_{\mu\nu} G^{\mu\nu}_a. \tag{1.8}$$

The index a sums over the eight $SU(3)$ gluon color states, while the indices μ and ν sum over the space-time variables. There is an implied summation over the six quark flavors. The first term is the Dirac Lagrangian describing a free spin-$\frac{1}{2}$ particle (quarks and antiquarks). The second term is necessary to fulfill the requirement of *local gauge invariance*, whereby the Lagrangian must remain invariant under any local phase (gauge) transformation. A local phase transformation is one that has space-time dependence,

$$\psi(x) \rightarrow e^{i\alpha(x)} \psi(x) \tag{1.9}$$

(where $\alpha(x)$ contains the space-time dependence), in contrast to a *global* phase transformation, such as

$$\psi(x) \rightarrow e^{i\alpha}\psi(x), \tag{1.10}$$

in which α is a constant. The G^a_μ in the second term are the gluon fields. This term describes quark-gluon interactions with coupling strength g.

The last term is the free Lagrangian for the gluon fields. Unlike the free quark Lagrangian, there is no mass term, thus implying that gluons are massless. Each gluon field strength tensor $G^{\mu\nu}_a$ has the form[17]

$$G^{\mu\nu}_a = \partial_\mu G^a_\nu - \partial_\nu G^a_\mu - g f_{abc} G^b_\mu G^c_\nu. \tag{1.11}$$

The last term in the tensor equation is a direct result of the non-Abelian nature of QCD and it is this term that sets QCD apart from QED. When inserted into the Lagrangian, this term provides for self-interaction among gluons. Since gluons themselves carry color charge, they can couple to other gluons as well as quarks. This is in contrast to QED, where photon-photon coupling is not allowed (since photons carry no charge). Gluon self-coupling alters the nature of the strong force coupling strength, as described in the next section.

1.3.3 Renormalization and the Running Coupling Constant

In QCD, the presence of gluon self-interaction affects the nature of the effective strong force coupling. Known as a running coupling constant, it takes the approximate form[17]

$$\alpha_s(Q^2) \simeq \frac{12\pi}{(11N_c - 2N_f)\log(Q^2/\Lambda^2)}, \tag{1.12}$$

where Q is the momentum at which α_s is to be determined, N_c is the number of colors and N_f is the number of flavors. The parameter Λ^2 is the QCD scale parameter, a momentum scale defined as [17]

$$\Lambda^2 = \mu^2 \exp\left[\frac{-12\pi}{(11N_c - 2N_f)(\alpha_S(\mu^2))}\right]. \tag{1.13}$$

The parameter μ is a product of the calculation of $\alpha_s(Q^2)$ from perturbation theory. In attempting to evaluate interaction diagrams beyond leading order[5], divergences arise due to the inclusion of higher–order corrections. These divergences are removed through the technique of *renormalization*, through which they are replaced by finite integral evaluations. The parameter μ is a scale (of arbitrary value) used in the renormalization that remains in the final expression.

For low values of Q^2 or, equivalently, at large distances, $\alpha_s(Q^2)$ becomes large. This is the opposite effect seen in QED, in which the effective coupling decreases with increasing distance. This increased coupling in QCD is believed to explain the concept of quark and gluon *confinement*, which restricts quarks and gluons to reside in bound states. Confinement explains why free quarks and gluons have never been experimentally observed.

At very high values of Q^2 (very short distances), $\alpha_s(Q^2)$ becomes very small. In this limit, quarks and gluons can effectively be treated as free objects. Known as *asymptotic freedom*, this weakening of the strong force greatly simplifies calculations at high Q^2. This realm of QCD is called the perturbative region, and perturbative QCD calculations form the foundation of much of our

[5] A *leading order* diagram is one in which no secondary contributions (e.g. gluon bremsstrahlung and loop contributions) are considered.

knowledge of the partons (quarks and gluons).

The parameter Λ defines the momentum scale at which $\alpha_s(Q^2)$ becomes large and so perturbative QCD begins to lose validity. In other words, it (loosely) defines the demarcation between the perturbative and non-perturbative regions. This parameter cannot be predicted by theoretical calculation and must be measured experimentally. Its value is typically $\sim$ 200MeV.

1.4 Introduction to Color Coherence

In hadron–hadron collisions, interaction typically occurs between one parton from each hadron. A typical parton–parton interaction in a $\overline{p}p$ collision might be, for example, $q\overline{q}$ scattering through the exchange of a gluon. Since both quarks and gluons carry color charge, and color is a conserved quantity, it is possible to map the exchange, or flow, of color through these parton–parton interactions. This mapping is called a *color flow* diagram. A leading order Feynman diagram for the reaction $q\overline{q}\rightarrow q\overline{q}$ with an example color flow diagram is given in Fig. 1.3.

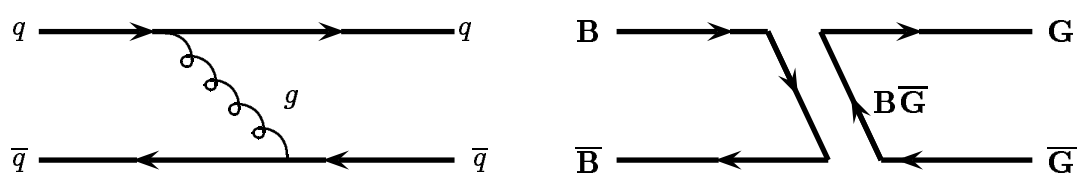

Figure 1.3. a) Feynman diagram and b) color flow diagram for $q\overline{q}\rightarrow q\overline{q}$

A leading order diagram does not account for higher order effects, such as gluon bremsstrahlung – each of the hard partons in such an event can radiate

numerous soft gluons[6]. These gluons can then create additional soft gluons and soft $q\overline{q}$ pairs, which can further radiate as well, in an iterative *cascade* process. The final distribution of partons emerges as hadrons at large distance scales from the interaction and are the objects actually observed in experimental detectors.

This soft parton distribution is not, in general, uniform in space. There are regions in which soft radiation is inhibited, resulting in local areas of lower multiplicity. This depletion is partially the result of interference of soft gluon amplitudes radiated from partons that are color-connected[18], a phenomenon known as *color coherence*. The regions of inhibitance are defined by the relative spatial orientation of the color-connected hard partons.

The local depletion due to gluon interference can be modelled by the *angular ordering* approximation of sequential parton emissions. To leading order in N_c (number of colors), angular ordering is the monotonic decrease in the emission angle for successive soft gluon radiation away from the interaction region[20]. Angular ordering will be described in detail in the next chapter. For now, Fig. 1.4 serves as a useful visual tool for understanding the effect. Consecutive gluon production is depicted to demonstrate the angular ordering restriction in an outgoing gluon cascade (note the successive angle reduction).

1.5 Introduction to the Analysis

The analysis described in this thesis is an attempt to observe the characteristic distribution of partons resulting from color coherence in $\overline{p}p$ reactions at the Fermilab Tevatron. One of the most important aspects of this study is that, while

[6] A *hard* parton is defined by the momentum scale $q^2 \sim Q^2$ and a *soft* parton is defined by $q^2 \ll Q^2$, where q is the parton momentum and Q is the momentum momentum scale of the interaction.

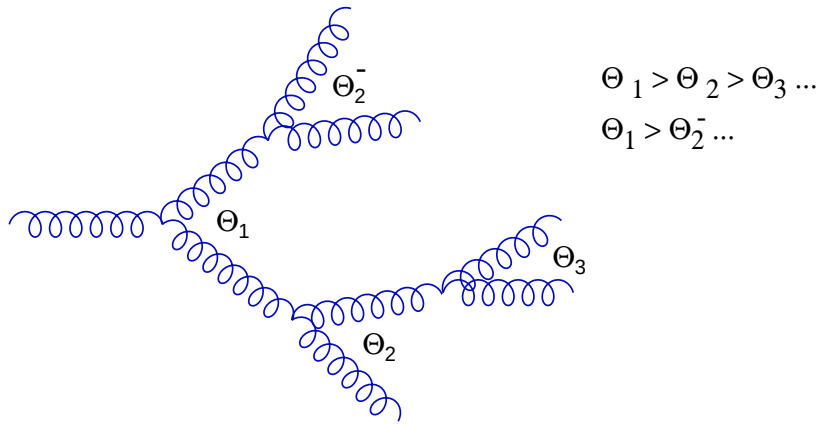

Figure 1.4. Example of angular ordering of successive gluon branchings. Notice that there is no direct relationship between Θ_2 and Θ_2'.

the color coherence patterns are constructed at the partonic level, observation of these patterns may only occur at the hadronic level. Belief in the observability of this effect rests on the hypothesis of Local Parton Hadron Duality (LPHD)[18]. LPHD proposes that general features of hadronic systems, such as particle multiplicity and angular distributions of particles, may be described analytically at the parton level using perturbative QCD calculations[18]. Thus, the observation of color coherence requires that the hadronization[7] process not destroy the interference patterns created by soft gluon radiation.

There may, in fact, be nonperturbative effects during hadronization that are qualitatively similar to perturbative color coherence effects. The relative contributions of these effects has direct implications for LPHD. The nonperturbative contributions are detailed in Chapter 2.

[7] *Hadronization* is the process in which partons emerging from a collision combine to form hadronic bound states.

1.5.1 Previous Experiments

Several studies of three-jet[8] events at e^+e^- colliders have shown clear evidence for color coherence effects in final-state partons[19]. In these studies, one of the jets is tagged as a gluon and the other two as a separating $q\overline{q}$ pair (see Fig. 1.5). The gluon is connected to each quark by a color line (indicating the flow of

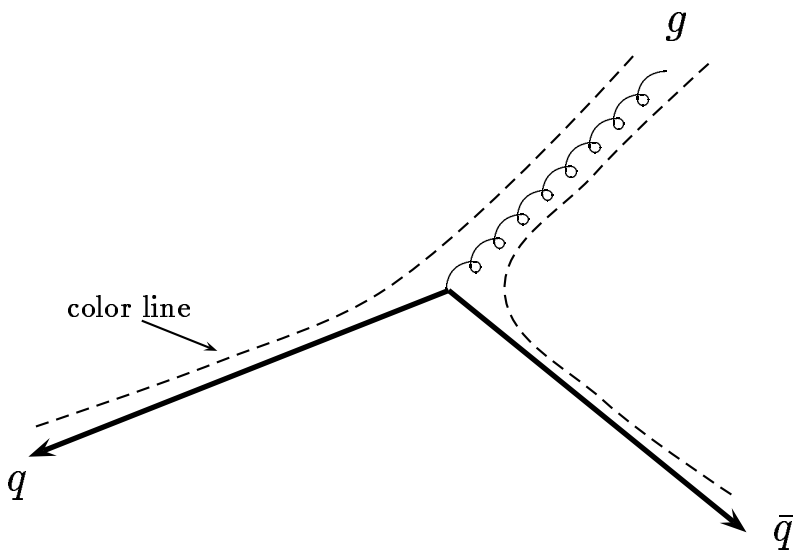

Figure 1.5. Color flow diagram for the $e^+e^- \rightarrow q\bar{q}g$ process.

color in the event). Enhancements in particle multiplicity are observed in the regions between the gluon jet and each of the quark jets, while a significant depletion is observed in the region between the quark jets.

This result is then compared with multiplicity distributions in events with two quark jets and a photon (in place of the gluon). In these events, the particle multiplicity is higher in the region between the two quarks than in either

[8]The frequently–used term *jet* refers to collimated streams of hadrons directed outward from a collision point and arising from multiple secondary emissions from an energetic parton. The definition of a jet at DØ will be more fully explored in Chapter 4.

region bordered by the photon and one of the quarks. Further, the multiplicity between the quarks is significantly higher for events with the photon when compared with events with the gluon. This is believed to be the result of a quark-antiquark color connection in the $q\overline{q}\gamma$ events which is not present in the $q\overline{q}g$ events (as shown in Fig. 1.5).

Such studies are more complicated at hadron colliders, however, due to the presence of colored constituents in the initial and final states. In addition to the large particle multiplicity from the hard scatter inherent in hadronic collisions, event-by-event fluctuations of the softer particle distribution produced by spectator[9] interactions further complicate experimental results. Recent studies by the DØ[20] and CDF[21] experiments have sought to minimize these effects by exploiting the Tevatron's high center-of-mass energy[10]. They search for two-jet events in which the coherent radiation is of sufficient energy to form a third, soft jet.

The angular distribution of the third jet in the data is compared with similar distributions in Monte Carlo simulations that incorporate color coherence effects and also with those that do not incorporate such effects. Angular ordering at the parton level is expected to result in third jet production preferentially between the second jet and the beam due to color connections. The distributions compare favorably with simulations that incorporate color coherence effects(JETRAD[22], HERWIG[23], and PYTHIA[24] with color coherence), while comparisons with simulations that do not incorporate color coherence reveal significant discrepancies in certain regions of phase space (ISAJET[25]

[9] *Spectator* partons are the proton and anti-proton remnant partons that do not participate in the hard interaction.

[10] The center-of-mass energy ($\sqrt{s}$) of the proton-antiproton beam at the Fermilab Tevatron is 1800GeV, currently the highest beam energy in the world.

and PYTHIA without color coherence).

1.5.2 W+jets as a Probe of Color Coherence

In this analysis, the color coherence pattern is studied through soft particle distributions rather than through jet distributions. The fine segmentation and good resolution of the DØ calorimeter systems allow for direct measurement of the energy depositions of the particles produced in hard scatterings. By accumulating statistics over many events (to reduce event-by-event fluctuations), the color coherence signal can be sought above the background energy (from spectator interactions and detector effects).

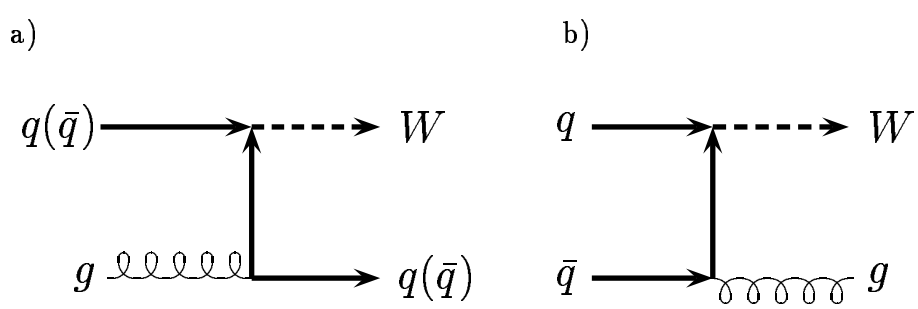

Figure 1.6. Leading order diagrams for a) $qg \to Wq$ and b) $q\overline{q} \to Wg$.

Events in which a W boson is produced along with an opposing quark or gluon (which then fragments into one or more hadron jets) are chosen for the particle flow study. The leading order Feynman diagrams for these events, called W+jets events, are shown in Fig. 1.6. Events of this kind can be divided into two spatial regions: one containing the W boson and one containing the opposing jet. W bosons are not carriers of color charge and therefore have no color connection with any parton in the event. The opposing parton, however,

is color-connected to the initial-state partons. The pattern of soft particles on the parton side of the event, therefore, is expected to be very different from that on the W boson side of the event due to interference effects between the initial-state and final-state color connections. W+jets events are very useful in this regard for measuring color coherence effects in hadronic collisions. The W boson, in effect, provides a convenient template against which soft particle patterns around the opposing jet may be observed. Such a measurement would be much more difficult with the multijet events used in the other DØ color coherence study due to the high particle multiplicity expected throughout such events. There is thus no region in these events expected to be relatively free of particles from the hard interaction. The leading order color flow diagrams for W+jets production are shown in Fig. 1.7 in the center-of-mass frame.

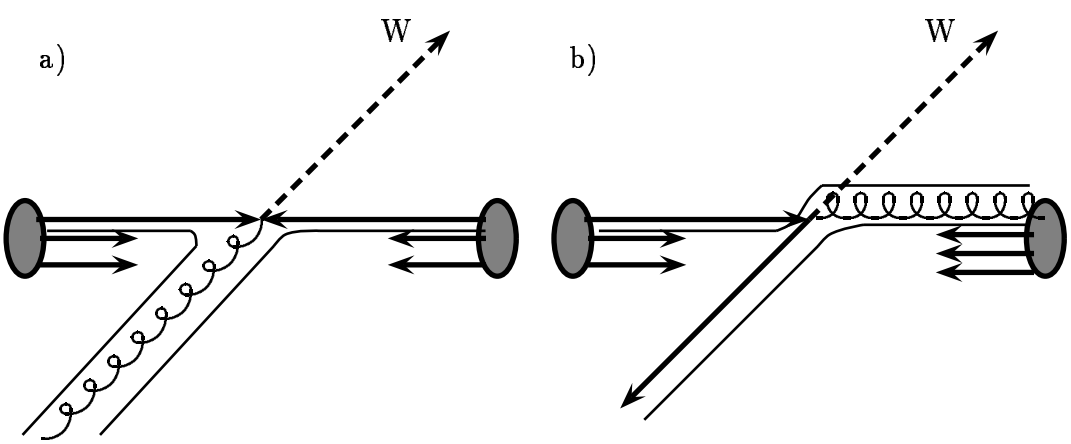

Figure 1.7. Color flow diagrams for a) $q\overline{q} \rightarrow Wg$ and b) $qg \rightarrow Wq$ in the center-of-mass frame. Thin solid lines represent the flow of color charge from the initial state partons to the final state partons.

The study of color coherence effects is interesting and important as a source of insight into the relationship between the perturbative and nonperturbative QCD realms. Hard scattering at the parton level can be reasonably described using analytical models, and predictions can be made using perturbative calculations. Descriptions at the nonperturbative/hadron level, however, must rely on phenomenological models. It is therefore important to know what effects at the parton level survive the hadronization phase, which is a probe of the LPHD hypothesis. A more complete treatment of color coherence follows in the next chapter.

CHAPTER 2

THEORETICAL OVERVIEW OF COLOR COHERENCE

In this chapter the phenomenon of color coherence is developed analytically, beginning with well-known leading order (LO) 2→2 processes. The derivation relies on matrix element factorization, applicable to additional radiation in the soft limit. The procedure is applied to processes which result in a $W + jet$ final state so that interference effects relevant to this analysis may be understood. This is followed by a discussion of the *angular ordering approximation*, which results from a simplification of the analytical color coherence expressions. Next, nonperturbative effects which are qualitatively similar to color coherence are described, and lastly the implementation of color coherence and related nonperturbative effects in Monte Carlo event simulation is presented, specifically the implementation within the PYTHIA event generator, which is used in this study for comparisons with collider data.

2.1 Soft Gluon Emission in Hadronic Scattering

In general, the description of additional gluon radiation in a hadronic 2→2 process

$$parton(1) + parton(2) \rightarrow parton(3) + parton(4) \tag{2.1}$$

requires a next-to-leading order (NLO) calculation of the 2→3 process

$$parton(1) + parton(2) \rightarrow parton(3) + parton(4) + gluon(5) \tag{2.2}$$

However, in the soft limit ($p_5 \rightarrow 0$), the calculation of the process 2.2 reduces to the description of the LO process 2.1 with *additional* terms describing the soft gluon radiation ($q \equiv p_5$ in the soft limit) from each hard parton (q_1, q_2, q_3, q_4)[26]. This statement is also true for the more relevant process

$$parton(1) + parton(2) \rightarrow Boson + parton(3) \tag{2.3}$$

with additional soft gluon production. Since the boson (e.g. W, Z or γ) is non-colored, it does not contribute to a description of gluon emission, thereby simplifying the calculation. The matrix amplitude $\mathbf{H}(q_1, q_2, q_3, q)$ for process 2.3 can be factorized (in the soft gluon limit) as[27][28][29]

$$\mathbf{H}(q_1, q_2, q_3, q) \simeq g_s \mathbf{h}(q_1, q_2, q_3) \cdot \mathbf{J}(q) \tag{2.4}$$

where g_s is the strong force coupling, $\mathbf{h}(q_1, q_2, q_3)$ is the matrix amplitude for the hard scattering process 2.1 and $\mathbf{J}(q)$ is the non-abelian semiclassical current for the soft gluon emission, defined as[26][29]

$$\mathbf{J}^{b,\mu}(q) = -\left(\frac{q_1^\mu}{q_1 \cdot q}\right) \mathbf{t}_1^b - \left(\frac{q_2^\mu}{q_2 \cdot q}\right) \mathbf{t}_2^b + \left(\frac{q_3^\mu}{q_3 \cdot q}\right) \mathbf{t}_3^b \tag{2.5}$$

where b is the color and μ is the polarization of the emitted gluon, and $\mathbf{t}_i^b$ is the color matrix of parton i.

The probability distribution for the soft gluon is obtained through squaring the current, so that

$$\begin{aligned}\mathbf{J}^2(q) &= 2(\mathbf{t}_1 \cdot \mathbf{t}_2)\frac{q_1 \cdot q_2}{(q_1 \cdot q)(q_2 \cdot q)} - 2(\mathbf{t}_1 \cdot \mathbf{t}_3)\frac{q_1 \cdot q_3}{(q_1 \cdot q)(q_3 \cdot q)} \\ &\quad -2(\mathbf{t}_2 \cdot \mathbf{t}_3)\frac{q_2 \cdot q_3}{(q_2 \cdot q)(q_3 \cdot q)}\end{aligned} \tag{2.6}$$

which can be rewritten in the form

$$\mathbf{J}^2(q) = 2(\mathbf{t}_1 \cdot \mathbf{t}_2)W_{12} - 2(\mathbf{t}_1 \cdot \mathbf{t}_3)W_{13} - 2(\mathbf{t}_2 \cdot \mathbf{t}_3)W_{23} \tag{2.7}$$

with

$$W_{ij} \equiv \frac{q_i \cdot q_j}{(q_i \cdot q)(q_j \cdot q)} \tag{2.8}$$

Each W_{ij} term corresponds to the emission of a soft gluon from partons i and j as a pair. Their meaning, which is explored in more detail below, is that a soft gluon may not be emitted from any hard parton i independently, but rather is influenced by interference from the other hard partons.

In the limit of massless partons, Eq. 2.8 may be rewritten as

$$W_{ij} \simeq \frac{1}{E_q^2}\frac{\alpha_{ij}}{\alpha_{iq}\alpha_{jq}} \tag{2.9}$$

where

$$\alpha_{ij} = 1 - \cos\theta_{ij} \qquad \alpha_{iq} = 1 - \cos\theta_{iq} \tag{2.10}$$

In the massless limit, therefore, the emission amplitudes W_{ij} are seen to depend only upon the gluon energy and simple angular relationships among the partons i and j and the gluon. To further elucidate the interference inherent in the W_{ij} amplitudes, they may be expanded and separated into components, such as

$$
\begin{aligned}
(E_q^2)W_{ij} &= \frac{\alpha_{ij}}{\alpha_{iq}\alpha_{jq}} + \frac{1}{\alpha_{iq}} - \frac{1}{\alpha_{iq}} + \frac{1}{\alpha_{jq}} - \frac{1}{\alpha_{jq}} && (2.11)\\
&= \frac{1}{2\alpha_{iq}}\left[1 + \frac{\alpha_{ij} - \alpha_{iq}}{\alpha_{jq}}\right] + \frac{1}{2\alpha_{jq}}\left[1 + \frac{\alpha_{ij} - \alpha_{jq}}{\alpha_{iq}}\right] && (2.12)\\
&\equiv (E_q^2)(W_{ij}^i + W_{ij}^j) && (2.13)
\end{aligned}
$$

In the above expressions, the W_{ij} amplitudes have been split into individual components for each parton, W_{ij}^i and W_{ij}^j. The component W_{ij}^i may be thought of as describing the emission of a gluon from parton i in the pair (i,j) (and similarly for W_{ij}^j). In this form, several interesting details regarding soft gluon emission are illuminated. It is instructive to consider the term W_{ij}^i written as

$$
W_{ij}^i = \frac{1}{2}\left[\frac{1}{\alpha_{iq}} + \frac{\alpha_{ij} - \alpha_{iq}}{\alpha_{iq}\alpha_{jq}}\right] \tag{2.14}
$$

The first term in brackets $(1/\alpha_{iq})$ corresponds to independent emission of a gluon from parton i. It contains no dependence on the azimuthal angle ϕ around that parton and exhibits a singularity at $\theta_{iq} = 0$. The second term accounts for interference from parton j. To first order, it contains no singularities. Azimuthal dependence arises in this second term due to the angle θ_{jq} in the α_{jq} term (for a fixed θ_{iq}, the angle θ_{jq} varies with ϕ_{iq}). Thus, the probability amplitude for soft gluon emission from parton i is, in general, *not* uniform in ϕ and depends upon the angle between the emitted gluon and the

parton j.

When $\theta_{iq} < \theta_{ij}$, the interference term in W^i_{ij} is positive, corresponding to constructive interference. In fact, W^i_{ij} achieves its maximum value inside the cone $\theta_{iq} < \theta_{ij}$ and when the gluon lies in the plane defined by i and j (which minimizes θ_{jq}). This configuration is shown below in Fig. 2.1, where the gluon g is emitted in the plane of the page between the partons i and j. Outside of the cone ($\theta_{iq} > \theta_{ij}$), the interference term in W^i_{ij} is negative, leading to a suppression of gluon emission[30].

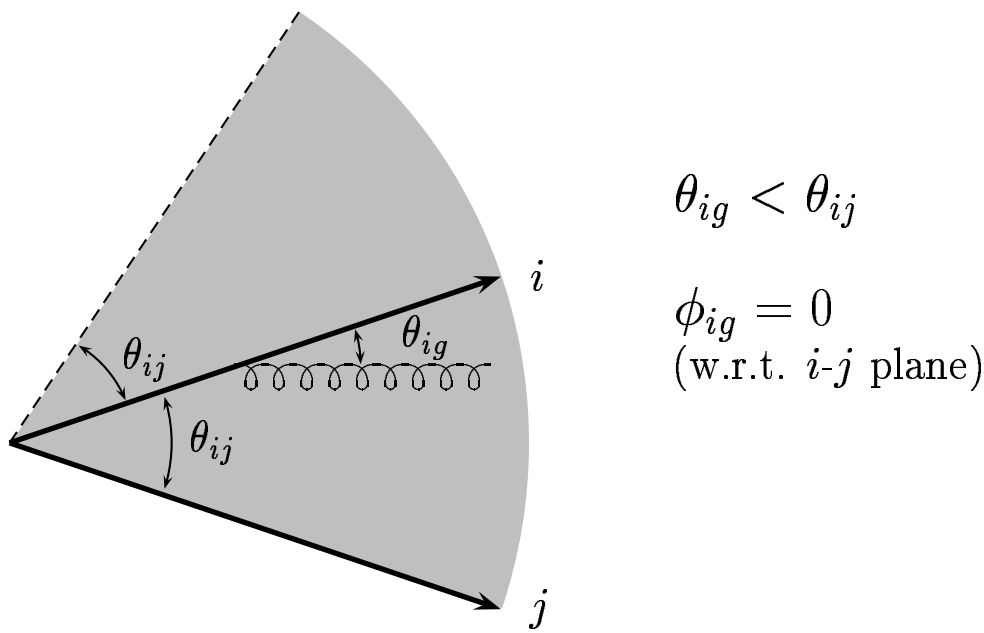

Figure 2.1. Emission cone around parton i as defined by partons i and j. Maximum probability for emission from parton i occurs when gluon is radiated between i and j.

2.2 *Color Flow Pattern in Leading Order W + Jet Processes*

The total probability amplitude $\mathbf{J}^2(q)$ may be expressed in terms of the individual amplitudes to calculate the full soft gluon radiation pattern[28] once the

color matrices have been evaluated. For a $q\overline{q} \rightarrow Wg$ event, for example, the pattern is

$$\mathbf{J}^2 = 2C_F(W^q_{qg} + W^{\overline{q}}_{\overline{q}g}) + C_A(W^g_{qg} + W^g_{\overline{q}g}) + \frac{1}{N_c}(W^q_{qg} - W^q_{q\overline{q}} + W^{\overline{q}}_{\overline{q}g} - W^{\overline{q}}_{q\overline{q}}) \quad (2.15)$$

where $C_F = (N_c^2 - 1)/N_c$ is the squared color charge for a quark and $C_A = N_c$ is the squared color charge for a gluon[28]. The leading order color flow for this process, in Feynman diagram form, is

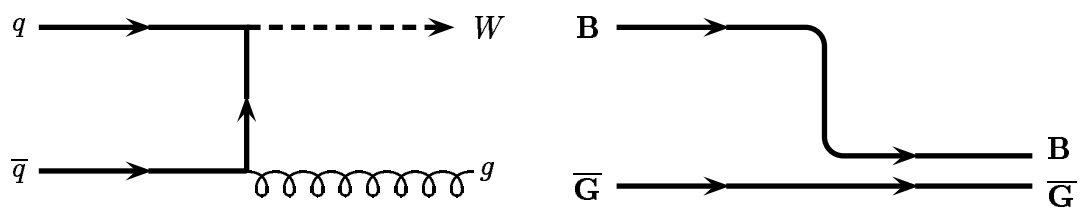

Figure 2.2. a) Feynman diagram and b) color flow diagram for $q\overline{q} \rightarrow Wg$

The first term in Eq. 2.15 (with the coefficient $2C_F$) describes soft gluon emission from the quark and the antiquark due to the quark-gluon and antiquark-gluon color-connected pairs, respectively. It includes contributions due to independent emission from the quark/antiquark and interference from the hard gluon color partner. The second term (with the coefficient C_A) similarly describes soft emission from the hard gluon that forms the two color-connected pairs. The last term contains higher-order interference contributions between the quark and antiquark, which are not color-connected in leading order (see Fig. 2.2b). This muddles the overall pattern somewhat, since this term does not exhibit the uncomplicated behavior of the first two. In particular, all of the leading singularities cancel, leaving only the interference terms. This can

be seen clearly by rewriting the four individual amplitudes from this last term in the form of Eq. 2.14:

$$\begin{aligned}\mathbf{J}^2_{(1/N_c)} &\equiv \frac{1}{E_{g'}^2}\frac{1}{N_c}\left[\left(\frac{1}{\alpha_{qg'}}+\frac{\alpha_{qg}-\alpha_{qg'}}{\alpha_{qg'}\alpha_{gg'}}\right)-\left(\frac{1}{\alpha_{qg'}}-\frac{\alpha_{q\overline{q}}-\alpha_{qg'}}{\alpha_{qg'}\alpha_{\overline{q}g'}}\right)\right.\\ &\quad\left.+\left(\frac{1}{\alpha_{\overline{q}g'}}+\frac{\alpha_{\overline{q}g}-\alpha_{\overline{q}g'}}{\alpha_{\overline{q}g'}\alpha_{gg'}}\right)-\left(\frac{1}{\alpha_{\overline{q}g'}}+\frac{\alpha_{q\overline{q}}-\alpha_{\overline{q}g'}}{\alpha_{\overline{q}g'}\alpha_{qg'}}\right)\right] \qquad (2.16)\end{aligned}$$

In this expression, the subscript g refers to the hard gluon, and g' refers to the soft gluon. The result is

$$\begin{aligned}\mathbf{J}^2_{(1/N_c)} &= \frac{1}{E_{g'}^2}\frac{1}{N_c}\left[\frac{1}{\alpha_{gg'}}\left(\frac{\alpha_{qg}}{\alpha_{qg'}}-1\right)-\frac{1}{\alpha_{\overline{q}g'}}\left(\frac{\alpha_{q\overline{q}}}{\alpha_{qg'}}-1\right)\right.\\ &\quad\left.+\frac{1}{\alpha_{gg'}}\left(\frac{\alpha_{\overline{q}g}}{\alpha_{\overline{q}g'}}-1\right)-\frac{1}{\alpha_{qg'}}\left(\frac{\alpha_{q\overline{q}}}{\alpha_{\overline{q}g'}}-1\right)\right] \qquad (2.17)\end{aligned}$$

At first glance, the coefficients for each of the parenthetical expressions appears to contain a leading singularity. However, as the singularity is approached, the corresponding parenthetical expression approaches zero, resulting in an indeterminate form. Although the application of L'Hospital's Rule is appropriate, it is simpler to just ignore the entire $\mathbf{J}^2_{(1/N_c)}$ expression by remembering that a) there are no leading singularities, and b) this expression is suppressed by two factors of N_c relative to the first two terms in $\mathbf{J}^2$. This is known as the *leading-order* N_c approximation. So, to leading order in N_c, the soft gluon radiation pattern is given by

$$\mathbf{J}^2 = 2C_F(W^q_{qg}+W^{\overline{q}}_{\overline{q}g})+C_A(W^g_{qg}+W^g_{\overline{q}g})+\mathcal{O}\left(\frac{1}{N_c}\right) \qquad (2.18)$$

A more intuitive feel for the radiation pattern can be obtained by diagram-

ing the radiation pattern $\mathbf{J}^2$ for a soft gluon of fixed energy $E_{g'}$ as a function of solid angle (Ω). For such a calculation, it is simpler to write $\mathbf{J}^2$ in terms of the color-pair amplitudes $W_{ij}(=W_{ij}^i + W_{ij}^j)$, resulting in

$$\begin{aligned} \mathbf{J}^2 &= N_c(W_{qg} + W_{\overline{q}g}) && (2.19) \\ &= \frac{N_c}{E_{g'}^2}\left(\frac{\alpha_{qg}}{\alpha_{qg'}\alpha_{gg'}} + \frac{\alpha_{\overline{q}g}}{\alpha_{\overline{q}g'}\alpha_{gg'}}\right) && (2.20) \\ &\equiv \mathbf{P}(E_{g'}, \Omega) && (2.21) \end{aligned}$$

to leading order in N_c, where the Ω dependence in $\mathbf{P}$ is defined by the W_{ij} amplitudes.

To further simplify the calculation for diagrammatic purposes, consider the case in which the W boson and the opposing hard gluon jet are oriented orthogonal to the beam direction (defined by q and $\overline{q}$), as shown below in Fig. 2.3. In this configuration, $\alpha_{qg} = (1 - \cos\theta_{qg}) = 1$ and $\alpha_{\overline{q}g} = (1 - \cos\theta_{\overline{q}g}) = 1$.

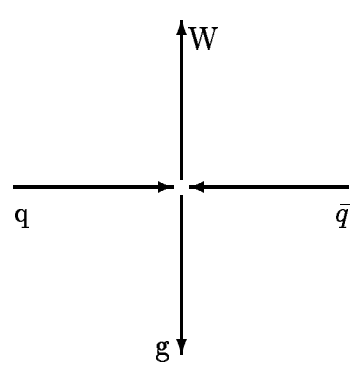

Figure 2.3. Orientation of $q\bar{q} \to Wg$ event for calculation of $\mathbf{P}(E_{g'}, \Omega)$

One further modification can be made to $\mathbf{P}(E_{g'}, \Omega)$ so that it matches DØ

experimental variables. The change in variable is $E_{g'} \rightarrow E_{T(g')}(= E_{g'} \sin\theta_{g'\overline{q}})$, where $E_{T(g')}$ is the energy of the soft gluon transverse to the initial state partons (a Lorentz invariant quantity). The radiation pattern for a soft gluon of fixed E_T is then

$$\mathbf{P}(E_{T(g')}, \Omega) = (\sin^2\theta_{g'\overline{q}}) \frac{N_c}{E^2_{T(g')}} \left(\frac{1}{\alpha_{qg'}\alpha_{gg'}} + \frac{1}{\alpha_{\overline{q}g'}\alpha_{gg'}} \right) \tag{2.22}$$

Figs. 2.4 and 2.5 below depict the relative gluon emission probability for the process $q\overline{q} \rightarrow Wg$ in the vicinity of the hard gluon jet and W boson, respectively. Axes represent the distance in azimuth ($\Delta\phi$) and *pseudorapidity* ($\Delta\eta$) from the

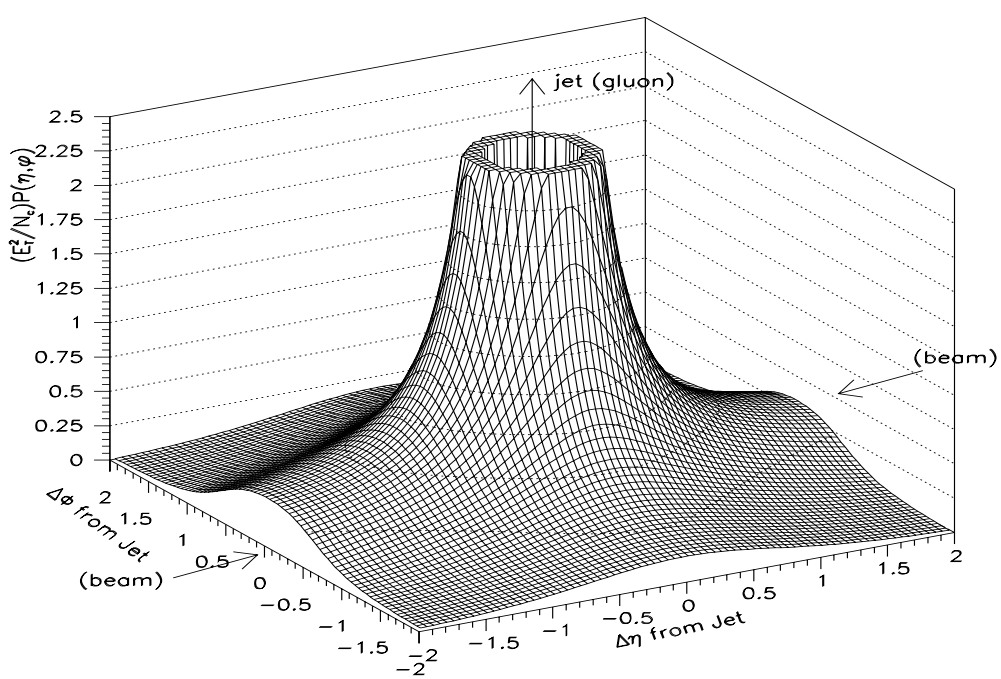

Figure 2.4. Soft gluon radiation pattern $(E^2_{T(g')}/N_c)\mathbf{P}(\Omega)$ around the gluon jet for the process $q\overline{q} \rightarrow Wg$ with $\eta_{Jet} = 0.0$.

W or gluon, where $\eta \equiv -\log(\tan\theta/2)$ is a measure of the polar angle *theta* of the W/gluon with respect to the initial-state partons. Labels indicate the locations of the intial state partons and final state hard gluon and W boson. The overall scale in each figure is not relevant - the shapes of the distributions contain the salient features. The most prominent feature in (Fig. 2.4) is the

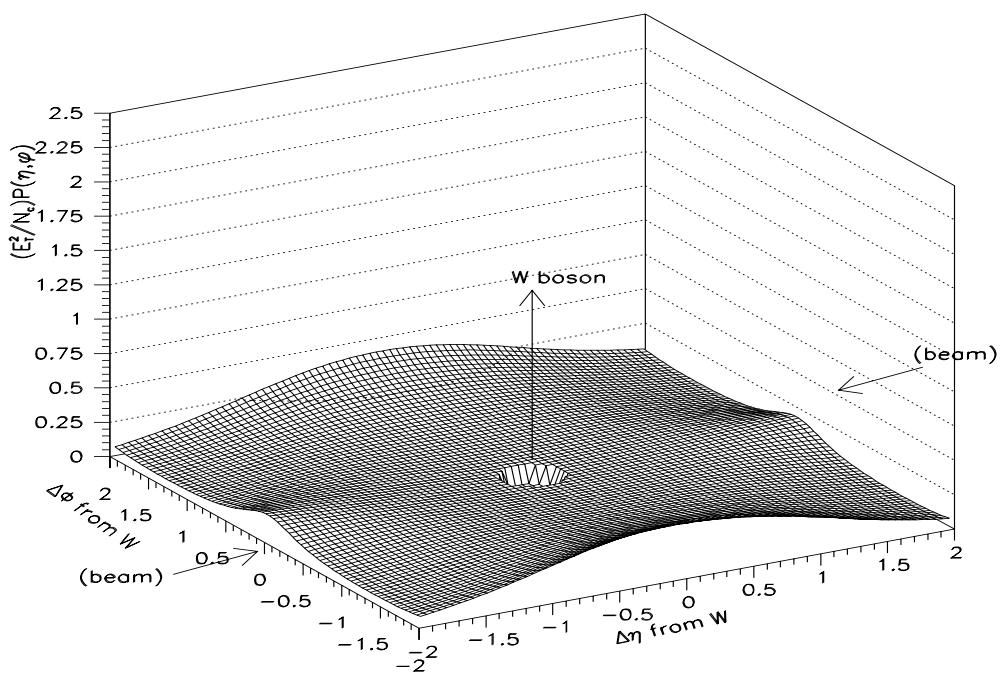

Figure 2.5. Soft gluon radiation pattern $(E^2_{T(g')}/N_c)\mathbf{P}(\Omega)$ around the W boson for the process $q\overline{q}\rightarrow Wg$ reaction with $\eta_W = 0.0$.

singularity at the hard gluon[1] (truncated in this picture). Of more importance, however, is the pattern at some fixed radius from the gluon jet. The combined probability amplitude is seen to reach a maximum in the plane of the event as defined by the gluon, the initial-state quark and the initial-state antiquark. This is the same effect described previously in Fig. 2.1. Interference effects

[1]Singularities exist at the quark and antiquark, as well, but these are are truncated in the figures and additionally suppressed by the $\sin^2\theta_{g'\overline{q}}$ term.

are maximized in the event plane. By contrast, the probability amplitude is at a minimum *transverse* to the event plane, and falling with increasing radius $R = \sqrt{\Delta\eta^2 + \Delta\phi^2}$ from the jet. It should be noted that, for the configuration in which all of the color partners are at right angles to each other, there is no region of phase space in which all interference terms are negative. However, their combined contributions are at a minimum in the transverse plane.

The distribution in the vicinity of the W boson (Fig. 2.5), by comparison, is topologically featureless. The pattern is flat over most of phase space (the central hole is an artifice used to indicate the location of the W boson), with slight rises at the edges. These rises are due to proximity with the initial-state partons and the hard gluon. Within a radius R=1.5 from the W boson, however, these contributions are extremely small relative to the jet side pattern.

The other LO process resulting in a $W + jet$ final state is $qg \rightarrow Wq$. The leading-N_c emission pattern for this process is described by

$$\mathbf{P}(E_{T(g')}, \Omega) = (\sin^2 \theta_{g'g}) \frac{N_c}{E^2_{T(g')}} \left(\frac{\alpha_{q_i g}}{\alpha_{q_i g'} \alpha_{gg'}} + \frac{\alpha_{q_f g}}{\alpha_{q_f g'} \alpha_{gg'}} \right) \tag{2.23}$$

where $q_{i(f)}$ refers to the initial-state(final-state) quark. The pattern for this process is shown in Figs. 2.6 and 2.7.

The difference in this process is that there is now a leading order color connection between the initial-state partons (quark and gluon). There is *not*, however, a leading order color connection between the initial-state quark and final-state quark. The effect is to skew the emission pattern in the direction of the initial-state gluon. This can be seen clearly in Fig. 2.6, which depicts the emission amplitude in the vicinity of the quark jet for the $qg \rightarrow Wq$ process. There is a leading order color connection between the final-state quark and the

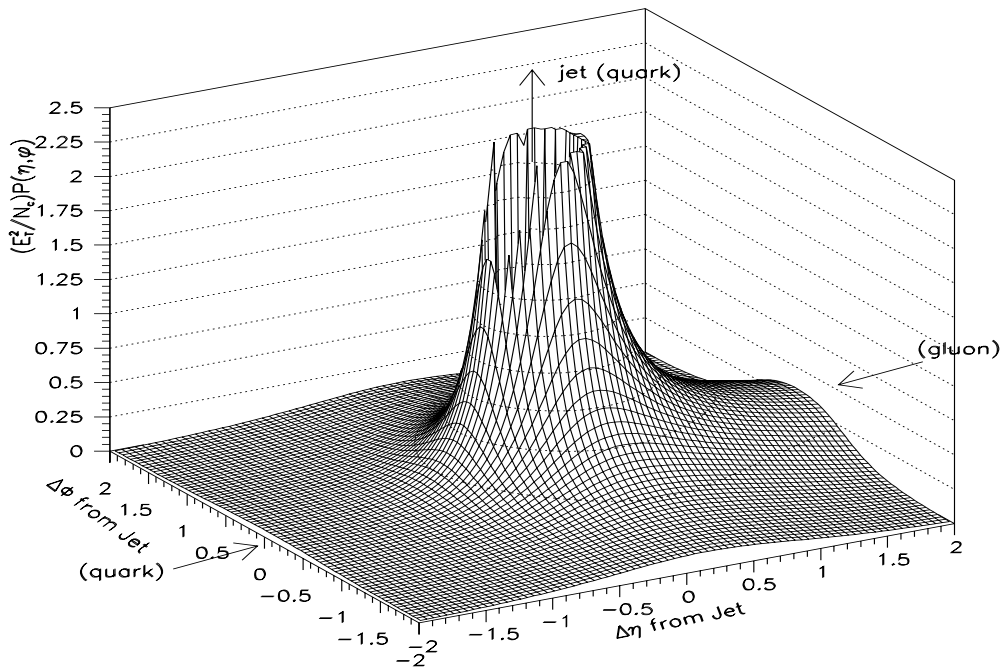

Figure 2.6. Soft gluon radiation pattern $(E^2_{T(g')}/N_c)\mathbf{P}(\Omega)$ around the gluon jet for the process $qg \to Wq$ reaction with $\eta_{Jet} = 0.0$

initial-state gluon, leading to constructive interference in the region between them. Interference between initial-state and final-state quarks, however, is suppressed by $1/N_c^2$ and thus does not contribute to the leading N_c calculation in Eq. 2.23.

The pattern around the W boson is shown in Fig. 2.7. There are clear differences between this pattern and W-side pattern for the $q\overline{q} \to Wg$ process due to the presence of the hard gluon in the initial state in Fig. 2.7. This gluon forms color pairs with each quark in the hard scatter. Both color pairs ($q_i - g$ and $q_f - g$) contribute in the region of the initial-state gluon, whereas the $q_i - g$ pair dominates in the region of the initial-state quark, thus resulting in the

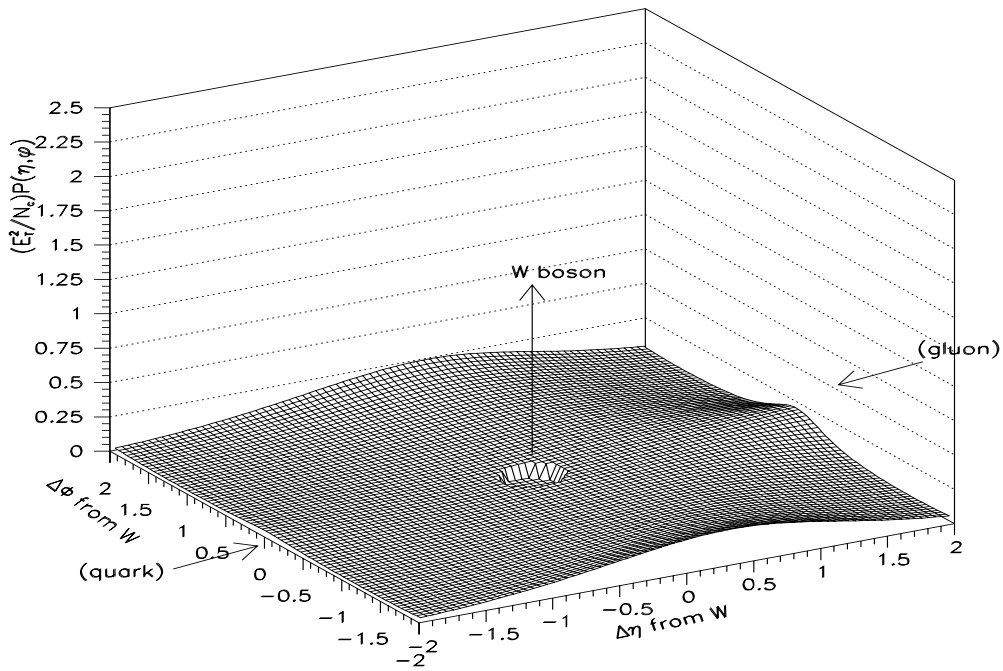

Figure 2.7. Soft gluon radiation pattern $(E^2_{T(g')}/N_c)\mathbf{P}(\Omega)$ around the W boson for the process $qg \to Wq$ reaction with $\eta_W = 0.0$

asymmetric pattern.

Figs. 2.4 – 2.7 provide a useful visual representation of the leading-N_c behavior of the soft emission amplitude in $W + jet$ production resulting from matrix element factorization. This amplitude may be incorporated into Monte Carlo simulations to model higher-order processes such as multiple consecutive gluon emission. This requires a further modification of the amplitude appropriate to the Monte Carlo technique. This modification, the *angular ordering approximation*, is described next.

2.3 Angular Ordering Approximation

Monte Carlo simulation of physics processes makes use of randomly generated event attributes weighted by known probability distributions. Nonnegative

probabilities are thus required. Unfortunately, the leading-N_c probability distribution for color coherence effects, Eq. 2.18, is not suitable for Monte Carlo simulation due to the interference terms in the individual amplitudes (W^i_{ij} terms). Recall the expression for these terms as given by Eq. 2.14. When a soft gluon with momentum q is emitted from parton i of the color pair (i,j) such that $\theta_{iq} > \theta_{ij}$, the interference term $(\alpha_{ij} - \alpha_{iq})/(\alpha_{iq}\alpha_{jq})$ is negative[28][30]. Thus, the amplitude W^i_{ij} is not positive-definite outside the cone $\theta_{iq} < \theta_{ij}$ centered on parton i (see Fig. 2.1). However, by integrating over the azimuthal angle ϕ, the amplitude reduces to[28][26][30]

$$\langle W^i_{ij} \rangle = \int \frac{d\phi_i}{2\pi} W^i_{ij} = \frac{1}{E_q^2 \alpha_{iq}} \Theta(\theta_{ij} - \theta_{iq}) \tag{2.24}$$

which is positive-definite.

This is the definition of the *angular ordering approximation.* The implication of this expression is that, when $\theta_{iq} < \theta_{ij}$, the parton i may emit a soft gluon independently of parton j, thus resulting in a uniform ϕ distribution within the emission cone. Outside the emission cone ($\theta_{iq} > \theta_{ij}$) the emission probability vanishes. The W^i_{ij} amplitude has therefore been reduced to a nonnegative form which is appropriate for Monte Carlo simulation of color coherence effects.

An improvement is possible to the angular ordering approximation that allows for interference effects on the ϕ distribution of the gluon while retaining the nonnegative requirement. This improvement is to simply apply the full amplitude W^i_{ij} within the emission cone (where the interference term is positive) and require that it vanish outside the emission cone. This restriction is just[28]

$$W^i_{ij} \rightarrow W^i_{ij} \Theta(\theta_{ij} - \theta_{iq}) \tag{2.25}$$

The effect of angular ordering (AO) on parton shower evolution following a hard scatter was briefly discussed in Chapter 1 and depicted in Fig. 1.4. Another description is shown below for a shower originating from a color-connected $q\overline{q}$ pair.

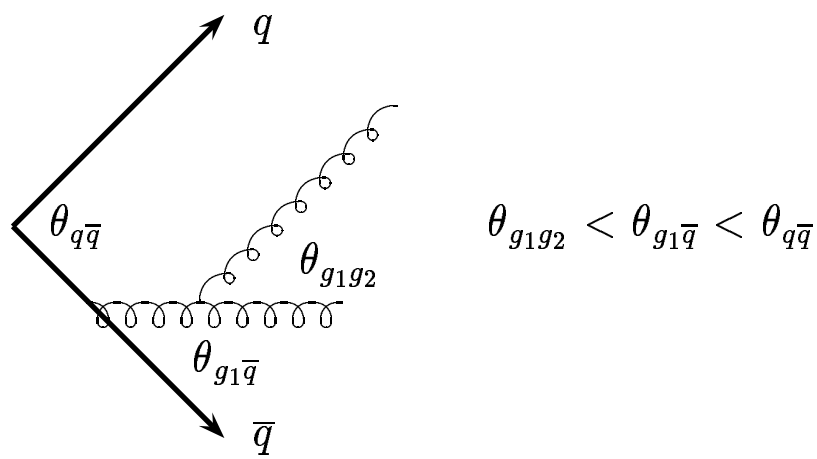

Figure 2.8. Example of angular ordering of successive gluon branchings.

AO is an iterative process that dictates the maximum opening angles for consecutive soft gluon emission in a parton cascade. For the first gluon, Eqs. 2.24 and 2.25 require that the opening angle for the gluon emission be less than the angle between the originating color-connected partons. Once a branching has occurred, the emitted gluon forms two new color-connected parton pairs, one with each of the parent partons, and the process is repeated. The second gluon may be emitted either from the $q_1 - g$ pair or the $g_1 - \overline{q}$ pair (g_1 denotes the first gluon). If emitted from the $g_1 - \overline{q}$ (as shown), the probability amplitude is nonvanishing only if $\theta_{g_1 g_2} < \theta_{g_1\overline{q}}$. If emitted from the $q_1 - g$ pair, the corresponding amplitude is nonvanishing for $\theta_{g_1 g_2} < \theta_{g_1 q}$. Therefore, for successive parton branchings, the opening angles are expected to decrease

sequentially.

The final distribution of partons (upon reaching the cascade cutoff point[2]) is seen to be confined by AO to specific regions defined by the originating partons. The principle of LPHD states that this distribution ought to be unaltered at the hadron level, as described in Chapter 1. However, there can be contributions to the hadron distribution due to nonperturbative fragmentation. In particular, certain fragmentation schemes can mimic color coherence/AO effects.

2.4 Nonperturbative Effects

Parton shower evolution proceeds, beginning from the hard scattering partons, until some cutoff limit is reached. This does not end the description of the process, however, because the resulting partons must combine to create color-singlet bound states (hadrons). The formation of hadrons from partons (known as *fragmentation* or *hadronization*) is a poorly understood process, however, from the standpoint of analytical calculations. Perturbative QCD, which describes hard interactions so well and which is the foundation for the development of AO, is not useful in this regime. The coupling strength α_s is large enough to make higher-order terms in perturbative expressions relevant, causing the calculations to break down. At the moment, no proven system based on first principles has risen to describe the nonperturbative evolution of partons to hadrons.

Several phenomenological schemes exist for modelling the fragmentation/hadronization[3] process which have been tuned to reproduce various experi-

[2]This is the energy limit below which partons are not evolved further. It is not unique and varies for different simulation programs

[3]These two terms are generally used interchangeably in QCD literature, although they are not strictly the same thing. Fragmentation refers to additional parton shower evolution

mental distributions. The three most common are the Lund String Fragmentation model[33], the Cluster Fragmentation model[34], and the Independent Fragmentation[35] model. The String and Independent Fragmentation models are studied explicitly in this analysis.

2.4.1 String Fragmentation

The Lund String Fragmentation model is founded on the notion of linear confinement, whereby the color field potential between a QCD charge and anticharge (e.g. a color-connected $q\overline{q}$ pair) increases linearly with spatial separation of the charges[36] [37]. As the charges move apart, the color potential energy between them increases. The String model invokes the concept of a one-dimensional *string*, stretched between the charges, to represent the field. The energy stored within this string (κ) is assumed to be uniform in length, with magnitude

$$\kappa \simeq 1\text{GeV/fm}. \tag{2.26}$$

As the potential energy between the charges increases, there is a finite probability that the string may *break* through the creation from vacuum of a quark-antiquark pair $q'\overline{q'}$. Two string segments are thus created, one for the $q\overline{q'}$ pair and one for the $\overline{q}q'$ pair (see Fig. 2.9

The quarks may continue to move apart and, with sufficient potential energy in either string segment, another $q\overline{q}$ string break may occur. This process repeats until no more string breaks are possible.

The probability for creation of a new $q\overline{q}$ pair with accompanying string

beyond the perturbative scale, while hadronization refers to the subsequent formation of hadrons from these partons and the decay of unstable particles which then follows. It is fragmentation which is of primary importance to this analysis, however, and this term will thus be used from here on.

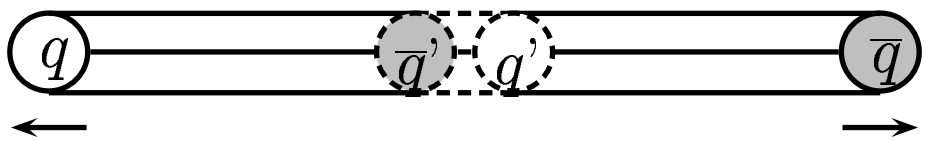

Figure 2.9. Description of color string stretched between a separating $q\overline{q}$ pair. A string break is shown in the middle accompanied by the production of a new $q\overline{q}$ pair.

break is governed by the mass and transverse momentum of the pair[36][37][38],

$$P(m, p_T) \propto \exp\left(-\frac{\pi m^2}{\kappa}\right) \exp\left(-\frac{\pi p_T^2}{\kappa}\right) \tag{2.27}$$

The transverse momentum of the quark and antiquark are determined by a Gaussian distribution, subject to the constraint that $p_T^q + p_T^{\overline{q}} = 0$ (i.e. there is no transverse motion allowed for the string). There is also a small ($\sim 10\%$) probability that, rather than producing a quark-antiquark pair at a string break, a diquark-antidiquark pair may be created[36]. In such a case, each diquark and antidiquark is treated as if it were a single parton for the purposes of mass and p_T distributions.

Once the string fragmentation has been completed, the picture is one of a linear chain of quark-antiquark pairs, joined by short string segments and bounded by the original $q\overline{q}$ separating pair. Mesons are created from these pairs in color-singlet states. Baryons can be created by either joining three quarks along the chain or by joining a quark with a diquark. As with mesons, color-singlet states must result. This scheme is shown below in Fig. 2.10[36].

The p_T of each hadron is the sum of the p_T's of its constituent partons.

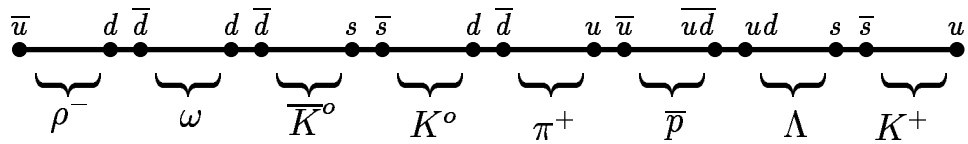

Figure 2.10. Hadron formation from a chain of quark-antiquark pairs created along a $u\overline{u}$ color string.

The energy E and longitudinal momentum p_z are determined in an iterative fashion, beginning with the leftmost (or rightmost) hadron and working right (or left). Each hadron takes some fraction z of the total $E+p_z$ remaining from the original $q\overline{q}$ system, so that this total decreases successively for each hadron along the chain. The z fraction is determined from the distribution[37]

$$f(z) = N\frac{(1-z)^a}{z}\exp\left(-\frac{bm_T^2}{z}\right) \tag{2.28}$$

where m_T is the hadron's transverse mass, while N, a, and b are free parameters. For the i'th hadron, E and p_z are then determined by the following expressions[37]:

$$(E+p_z)_i = (1-z)(E+p_z)_{i-1} \tag{2.29}$$

$$(E-p_z)_i = (E-p_z)_{i-1} - \frac{m_T^2}{z(E+P_z)_{i-1}} \tag{2.30}$$

The end result for a single string is an assortment of hadrons oriented along the string's length, each with known momentum relative to the string. For a system of partons resulting from a hard scatter and shower evolution, the picture is conceptually the same. Each color connection among the partons

results in a one-dimensional string drawn between them. Each gluon, having two color connections, gives rise to two string segments. This can be seen in Fig. 2.11, which shows one possible string arrangement for a system of partons in an event.

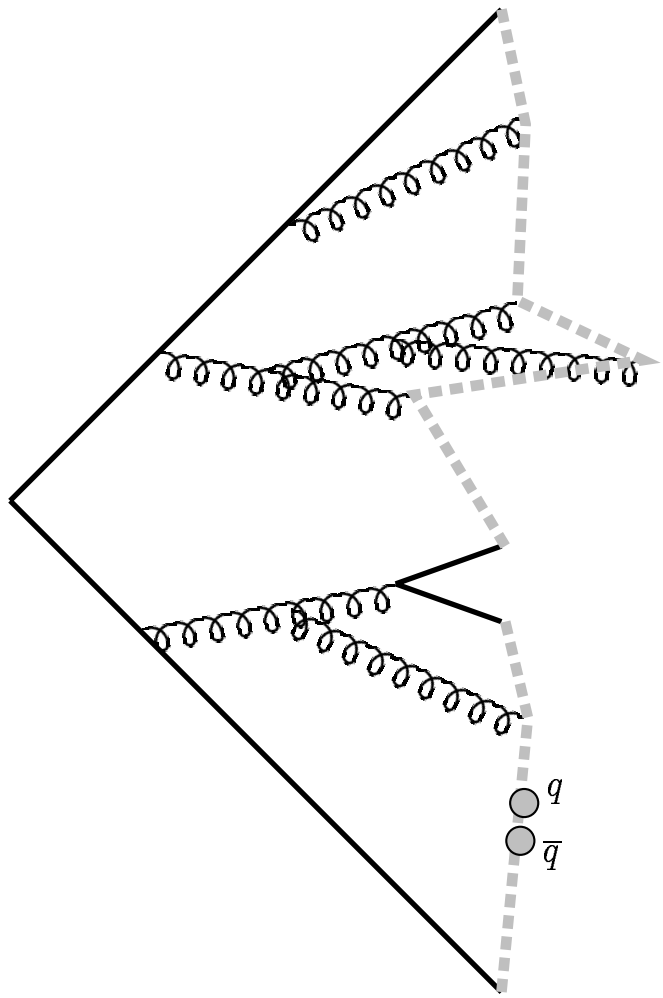

Figure 2.11. Visual description of String model. One-dimensional string spans all color-connected partons following cascade process from a $q\overline{q}$ pair. The light gray circles represent a $q\overline{q}$ pair being pulled from the vacuum along a string.

Each string segment is treated separately. The fragmentation is performed in the center-of-mass system of the string, such that the end partons are mov-

ing in the $\pm z$ directions. Following the fragmentation procedure, the resulting hadrons are then boosted back into the lab frame. If the hadron momenta relative to the string are much smaller than the boost, their trajectories will follow the string direction. Since the string direction was determined during the partonic shower evolution, it is greatly influenced by color coherence effects. Therefore, by accounting for color connections among the partons, the String Fragmentation scheme may produce hadrons in a pattern similar to the partonic pattern created by angular ordering. In effect, the String model treats each color-connected parton pair as a dipole, much the same as for the leading-N_c interference calculations. The contribution of String Fragmentation relative to AO in hadron distributions is an interesting attribute of hadronic physics to study. It has never been explicitly tested in a hadron-hadron collider.

2.4.2 Independent Fragmentation

The Independent Fragmentation model assumes that each parton in an event fragments independently of all other partons. There is therefore no conceptual picture of a string or any other connection with surrounding partons. Furthermore, the fragmentation takes place for all partons in the center-of-mass frame of the event, as opposed to the frame of the string in the String model.

A quark q in the Independent Fragmentation model fragments into a $q\overline{q_1}$ pair and a remainder quark q_1, where the pair $q_1\overline{q_1}$ is pulled from the vacuum. As with String fragmentation, the p_T of each member of the pair is generated from a Gaussian distribution and the requirement of no net p_T for the pair is imposed. The energy and longitudinal momentum with respect to the original quark are also chosen as in the String model, with the splitting fraction z following the distribution given by Eq. 2.28. The remainder quark is then

fragmented into another $q_2\overline{q_2}$ pair and another remainder quark q_2. This process is iterated until the remainder quark no longer has sufficient energy to fragment. Baryons are formed using the same method as the String model.

No unique procedure exists for the fragmentation of gluons. The most common method is to split the gluon into a $q\overline{q}$ pair and then fragment the quark and antiquark separately. The two partons would share the total gluon energy according to the Altarelli-Parisi splitting function[39].

The Independent Fragmentation model leads to hadron trajectories that closely follow the original parton direction. This is in contrast to the String model, which populates the region between color-connected partons as well. Studies of the *string effect* (described in Chapter 1) in e^+e^- experiments have shown that the string picture more accurately reproduces the particle distributions in data, but this has never been explicitly tested at a hadronic collider[4].

2.5 Monte Carlo Simulation

The implementation of color coherence in a Monte Carlo simulator is of prime importance in this analysis. Of the many available simulations available today, only the PYTHIA program allows a user to explicitly test angular ordering and fragmentation separately in a consistent manner. This is because PYTHIA allows the user to turn angular ordering on or off and also to choose between string and independent fragmentation. Based on the above discussions, a sample of $W+jet$ events simulated with angular ordering and string fragmentation is expected to exhibit a very different pattern of particles than one with no angular ordering and independent fragmentation.

[4]Color coherence studies of three-jet events at DØ (described in Chapter 1) have shown insufficient sensitivity to fragmentation effects to compare different models, an interesting result in its own right.

For final-state soft radiation in parton shower evolution, soft gluon emission is governed in PYTHIA by the improved angular ordering approximation (Eq. 2.25), thereby leading to nonisotropic azimuthal gluon distributions in consecutive branchings. The parton shower evolves according to the Altarelli-Parisi equations[37][40] with evolution variable $Q^2 = m_a^2$, where m_a is the mass of the parent parton a in a branching $a \to bc$. The branching products each get a fraction of the parent energy, defined by the splitting variable z such that $E_b = zE_a$ and $E_c = (1-z)E_a$. The masses of the branching products are required to be monotonically decreasing at each branching, so that $m_b + m_c < m_a$. This may or may not lead to a decrease in opening angle for consecutive branchings, but PYTHIA ensures this through angular ordering – if parton b in the $a \to bc$ branching then branches as $b \to de$, angular ordering requires that $\theta_{de} < \theta_{bc}$, where $\theta_{bc(de)}$ is the opening angle for branching products b and c (d and e). The azimuthal angle ϕ for each branching is chosen by Eq. 2.25 using a standard rejection method. Parton branching continues until the mass of each branching product is below the minimum mass $m_{min} = 1$GeV.

For initial-state radiation, the backward evolution procedure is used[31], whereby the branching process proceeds backwards from the scattering partons toward the original parton/antiparton. Initial-state partons have space-like virtuality ($m^2 < 0$). The virtuality $Q^2 = -m^2$ is the evolution variable for the Altarelli-Parisi equations governing the shower development – it is highest at the interaction point and decreases backwards toward the parent hadron. Consecutive branchings are therefore required to have strictly decreasing virtualities.

At first glance, it appears that initial-state parton evolution is just the time-reversal of final-state evolution. However, there are two significant differences.

First, coherence influences the branching process much less for initial-state radiation than for final-state radiation due to the kinematics of initial-state radiation[32]. This is because, for time-like showers ($m^2 > 0$), both energies and masses decrease as the shower evolves. Emission angles, which are approximately the ratio of p_T over energy, behave approximately as mass over energy, and thus a priori can go either way. Coherence here makes a big difference, since kinematics have little influence over the emission angles. In space-like branchings, on the other hand, energies are still decreasing toward the interaction but Q^2 increasing, so emission angles also tend to increase as the initial-state hard parton approaches the scattering region. Ordering in Q^2 therefore, usually ensures angular ordering without the need for coherence contributions[41]. The second difference is that, for branchings from the initial-state partons, ϕ is chosen randomly, without the inclusion of interference effects. This is a characteristic of the current version of PYTHIA (v5.7) and not due to any theoretical considerations.

Some inconsistency therefore exists in the treatment of the two forms of radiation in PYTHIA. However, each gluon emitted from the space-like initial-state partons can then initiate its own shower, just as gluons emitted from the final-state parton can. These secondary emissions are treated as time-like, and interference effects therefore contribute.

2.6 Color Coherence Study

This analysis is an attempt to observe the various effects described in this chapter using $W + jet$ data from the DØ detector. Global event shapes in the data will be compared with $W + jet$ events simulated by the PYTHIA simulation package with the implementation of both perturbative effects (angular order-

ing) and nonperturbative effects (fragmentation) toggled to determine what combination is most consistent with the data, if any. The following chapter is the first step in the process, in which the Fermilab accelerators and the DØ experimental apparatus are described.

CHAPTER 3

THE TEVATRON AND THE DØ DETECTOR

The DØ detector is located at the Fermi National Accelerator Laboratory (Fermilab) in Batavia, Illinois. It is a complex, multipurpose device, enabling the study of many aspects of particle physics. Collisions are provided by the Fermilab Tevatron, the highest-energy hadron collider in the world, with a center-of-mass energy of 1800 GeV. A brief description of the Tevatron precedes a more detailed description of the detector.

3.1 The Fermilab Tevatron

The Fermilab accelerator complex (shown below in Fig. 3.1) actually consists of five separate accelerators working in concert, culminating in the Tevatron. The high energy required for the colliding beams necessitates several stages of acceleration.

The proton and antiproton beams which collide in the Tevatron are created by very different, complicated processes. The proton beam originates as hydrogen ions (H^-), delivered in 18 KeV pulses from a plasma source[42]. The first stage of acceleration is a Cockcroft-Walton generator, which uses an electrostatic field to increase the kinetic energy of the ions to 750 KeV[43]. The beam of ions is then sent to a 150 m long linear accelerator, or linac, where it is accelerated to an energy of 400 MeV[42]. Then the beam is passed through a

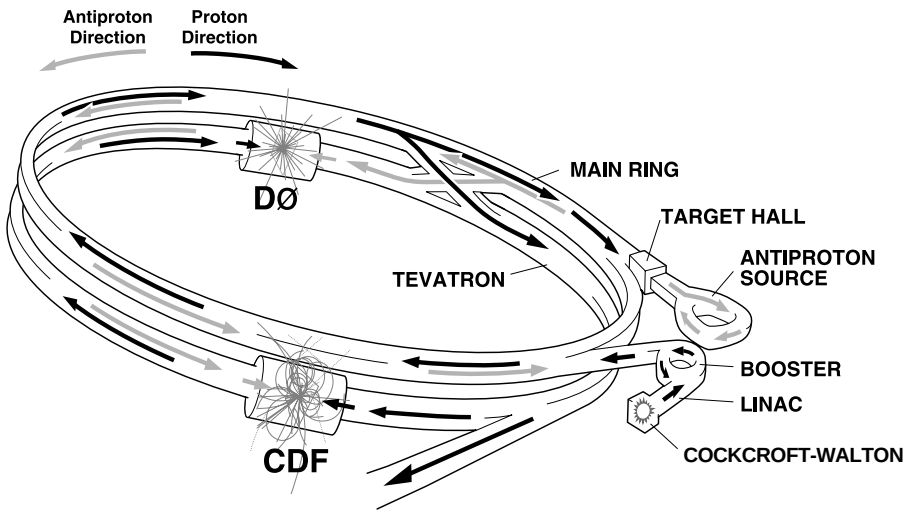

Figure 3.1. Schematic view of the Fermilab accelerator complex with the DØ and CDF detectors.

thin carbon target, which strips off the electrons, leaving a pure proton beam. The proton beam is further accelerated in the Booster Ring, a 151 m diameter synchrotron in which the beam achieves an energy of 8 GeV. The beam is then injected into the Main Ring, a 1 km radius synchrotron composed of conventional copper-coiled magnets that lies directly above the Tevatron. The Main Ring has two functions - to serve as an injector for the Tevatron and as a proton source for antiproton production (described below). As an injector, the Main Ring accelerates the beam to 150 GeV, with a structure of six antiproton bunches[42]. These bunches are then injected into the Tevatron, the final synchrotron. The Tevatron uses superconducting magnets operating at a temperature of 4.7 Kelvin and producing a maximum magnetic field of 4 Tesla[42]. This field is sufficient to hold 900 GeV protons and antiprotons in a circular orbit of 1 km radius[43].

When acting as a proton source for antiproton production, the Main Ring

accelerates the proton beam to 120 GeV. The beam is then extracted from the Main Ring and focused on a copper/nickel target. Approximately 20 antiprotons are created for every 10^6 incident protons[42]. These newly formed antiprotons have a wide range of momenta and large angular dispersion. To reduce this dispersion, they are passed through a cylindrical region of lithium containing a strong electric current which acts as a lens, focusing the antiprotons into a manageable beam[42]. The beam is sent into the first of two storage rings, the Debuncher. In the Debuncher, stochastic cooling processes occur, employing sensors which measure the beam orbit and momentum spread relative to the desired orbit and momentum spread and which activate kicker electrodes which gradually adjust the beam with each orbit as necessary[43]. The beam is then transferred to the Accumulator, a storage ring inside the Debuncher. The beam is cooled further in the Accumulator and stored there while new antiprotons are created from the Main Ring proton beam. When enough antiprotons have been collected in the Accumulator (typically $50 - 100 \times 10^{10}$, requiring several hours of accumulation[42]), the beam is transferred back to the Main Ring in the direction opposite the protons, where it is accelerated to 150 GeV bunches and injected into the Tevatron.

In the Tevatron, proton and antiproton beams counter-rotate, held apart by electrostatic separators. At two collision points (the sites of the DØ and CDF detectors), the beams are narrowly focused with quadrupole magnets so that the bunch diameter is about $40\mu m$ (the mean length of the bunches is ~ 30 cm). Bunch crossings occur about once every $3.5\mu s$. Once collisions begin, the beam typically lasts from 10 to 20 hours. Antiproton accumulation continues during this time so that enough antiprotons will be available when a new beam is required.

3.2 Coordinate Systems

A detailed description of the DØ detector would be awkward without some discussion of the many coordinate systems used in the experiment. There are no less than four coordinate systems in use at DØ - Cartesian (x, y, z), cylindrical (r, ϕ, z), spherical (r, ϕ, θ), and the (η, ϕ) system, a special subset of the spherical coordinate system. The origin for all of these systems is the geometric center of the detector. The positive z-axis is aligned with the proton beam direction, while the positive y-axis points vertically upward. The demand for a right-handed coordinate system requires, then, that the positive x-axis point radially outward from the center of the Tevatron ring. The azimuthal variable ϕ is defined such that $\phi = 0$ is aligned with the positive x-axis and $\phi = \pi/2$ is aligned with the positive y-axis. The polar variable θ is defined such that $\theta = 0$ is aligned with the positive z-axis (the direction of the proton beam) and $\theta = \pi/2$ is aligned with the positive y-axis.

The (η, ϕ) coordinate system is based on the *rapidity* variable, y. Rapidity is defined as

$$y = \frac{1}{2} \ln \frac{E + p_z}{E - p_z}, \tag{3.1}$$

where E and p_z refer to the energy and longitudinal (z) component of momentum of a particle or group of particles. This variable is useful in describing particle distributions due to the fact that its differential is Lorentz invariant, so that the shape of the rapidity distribution does not change with a boost in the longitudinal direction.

With the approximation that p>>m (particle momenta are much greater than their rest mass, which is reasonable for most particles at Tevatron ener-

gies), then $E \simeq p$, so that the rapidity may be rewritten as

$$y \simeq \frac{1}{2} \ln \frac{1 + E_z/E}{1 - E_z/E}. \tag{3.2}$$

With the definition $\cos\theta = E_z/E$, this becomes

$$y \simeq \frac{1}{2} \ln \frac{\cos^2(\theta/2)}{\sin^2(\theta/2)} = -\ln[\tan(\theta/2)] \equiv \eta \tag{3.3}$$

The variable η, called *pseudorapidity*, is typically used with ϕ to measure particle distributions in the DØ detector. Since momentum is not measured at DØ (as explained below), η is used rather than y.

The coordinates η and ϕ just described are known as *detector coordinates*, because they use the detector center as their origin. During beam crossings, however, collisions typically occur at some distance in z away from the center $z = 0$. In fact, the interaction vertex can occur as far away as 40 cm or more from $z = 0$. The vertex can also be displaced in x and y. When this happens, new coordinates need to be defined relative to the vertex instead of the detector center. The new, vertex-corrected η and ϕ are called *physics coordinates*. The distinction between detector and physics coordinates is very important when calculating such quantities as E_T , as will become evident in the analysis discussion in Chapter 6.

The notations E_T and p_T are used frequently when describing physics in a hadronic collider. They refer to the energy and momentum, respectively, of a

particle or jet *transverse* to the beamline. Transverse energy is defined as

$$E_T = E\sin(\theta) \tag{3.4}$$

where θ is the polar angle previously defined.

3.3 The DØ Detector

The design of the DØ detector was optimized for the study of high-p_T physics in hadronic collisions at Tevatron energies. Emphasis was placed on the identification of energetic electrons/positrons and muons, the measurement of the energy and direction of high-p_T jets, and the measurement of missing E_T ($\not{E}_T$), which aids in the identification of neutrinos[44].

The design philosophy dictated that no central magnetic field be provided in the detector. Due to the high transverse momentum of the objects studied at DØ , energy measurement by calorimetry is superior to momentum measurement by track curvature[44]. Further, the absence of a magnet in the central part of the detector allows for compression of the tracking chambers, leaving more volume in the detector for calorimetry.

Note that, in the absence of a central magnetic field, it is not possible to differentiate electromagnetic charge states for electrons/positrons and other charged particles (except muons, as explained in Sec. 3.6). For simplicity, therefore, the term electron will refer generically to electrons and positrons for the remainder of the dissertation.

A cutaway view of the detector is shown in Fig. 3.2. It is very large, measuring about 13m in height and 20m in length, and weighing approximately 5500 tons[44]. The Tevatron beamline passes through the center of the detector,

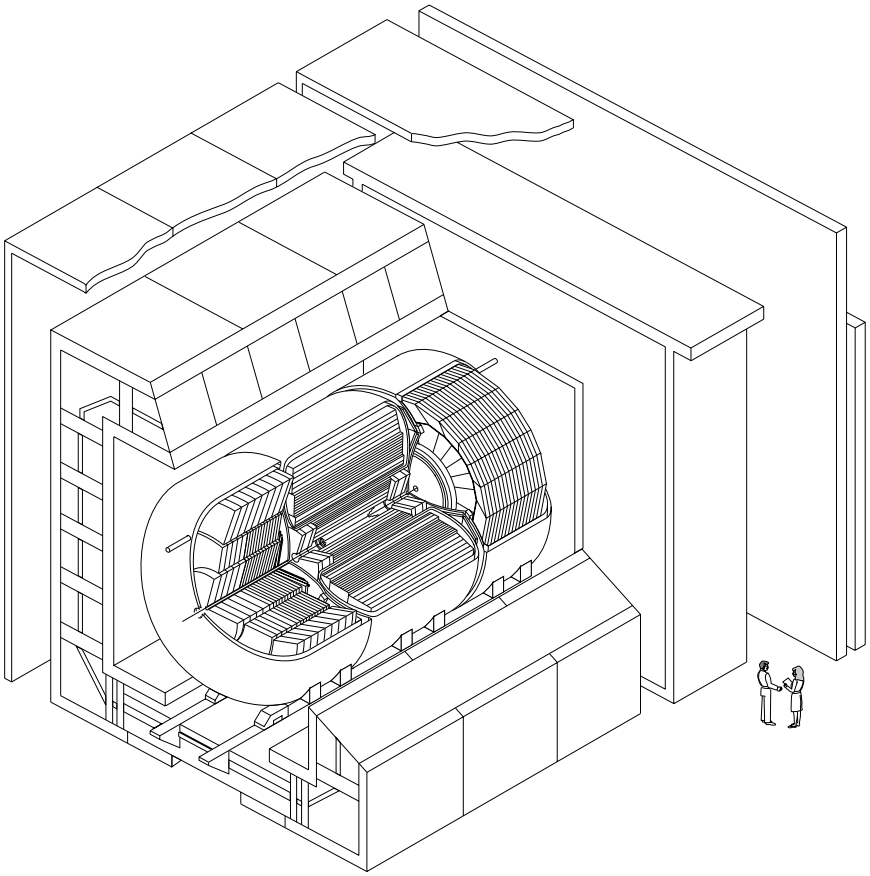

DØ Detector

Figure 3.2. Overview of the DØ detector

while the Main Ring beamline passes through the upper portion. The many detector systems that comprise the DØ detector can be broadly divided into three categories - the tracker, the calorimeter, and the muon system. Each of these systems is described in the sections that follow, with particular attention paid to the calorimeter, which is the most crucial element of both the detector and this analysis. A section detailing the data acquisition system is also included.

3.4 Tracker

The DØ tracking system (commonly termed the Central Detector, or CD) is comprised of four detector subsystems - the Vertex Drift Chamber (VTX), the Transition Radiation Detector (TRD), the Central Drift Chamber (CDC), and two Forward Drift Chambers (FDC). The orientation of these subsystems is depicted in Fig. 3.3. The overall length of the CD is 270 cm, centered at the point $z = 0$. The inner radius of the CD is 3.7 cm from the beamline and the outer radius is 78 cm[44]. Tracking design was influenced by the absence of a

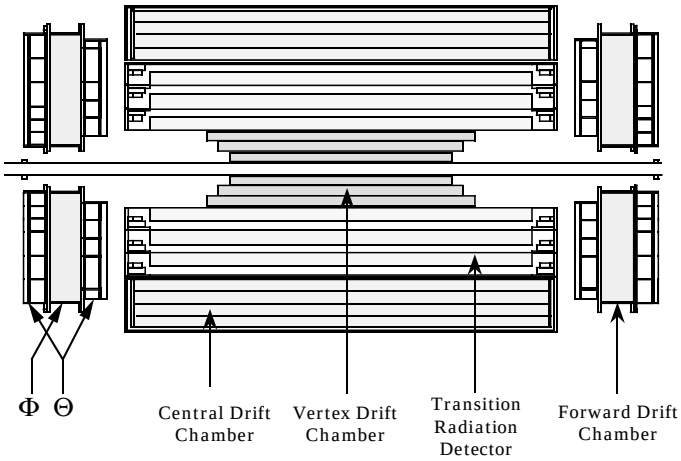

Figure 3.3. Side view of the Central Detector (tracking system)

central magnetic field, which necessitated high space-point position resolution, good ionization energy measurement (dE/dx) to differentiate electrons from photon conversion pairs, and good two-track resolving power[45].

3.4.1 Vertex Drift Chamber (VTX)

The VTX is the tracking chamber closest to the beamline, with an inner radius of 3.7 cm, an outer radius of 16.2 cm, and a length of 116.8 cm[44]. The VTX consists of three concentric, cylindrical layers of drift chambers. The inner

layer contains 16 drift chamber cells - covering the full range in ϕ, while each of the outer layers contains 32 cells. The cells are staggered in ϕ for each layer to avoid dead regions. There are 8 sense wires mounted in each cell. Each cell is filled with a gas mixture of CO_2 (95%) and ethane (5%)[44], with a small amount of H_2O (0.5%)[46]. A charged particle passing through the drift chamber ionizes the medium. Due to the presence of a strong electric field ($\langle \vec{E} \rangle \simeq$ 1kV/cm) and sense wires at positive high voltage (2.5kV), the electrons from the ionization drift towards the sense wires, with an average drift velocity of 7.3μm/ns. Near the sense wires, the electrons have sufficient energy to induce an avalanche, whose accumulated charge is then collected on the sense wire and read out at either end. The $r\phi$ position of a hit is determined using the drift time measurement and knowledge of the wire location[47]. The z position of a hit is determined by a charge division technique using the pulse measurements at either end of the sense wire[47]. The VTX parameters are summarized in Table 3.1[44][46].

Table 3.1. Parameters for DØ Vertex Drift Chamber

Parameter	**Specification**
Radius	3.7 cm - 16.2 cm
Overall Length	116.8 cm
Number of Layers	3
Number of Cells	16,32,32 (for Layers 1,2,3)
Number of Sense Wires	8 per cell (640 total)
Sense Wire Voltage	+2.5kV
Drift Field	1kV/ cm
Gas Type	95% CO_2+5% ethane+0.5% H_2O
Gas Gain	4×10^4
Spatial Resolution	$r\phi \simeq 60\mu$m, $z \simeq 1.5$ cm

3.4.2 Transition Radiation Detector (TRD)

The TRD is situated just outside the VTX, spanning the radial interval from r=17.6 cm to r=47 cm, and having a length of 165 cm[44]. Its function is to provide discrimination between electrons and pions.

When an ultrarelativistic particle crosses the boundary between two different dielectric media, small amounts of transition radiation in the X-ray range are emitted in the direction of the particle. By crossing several of these boundaries in succession, the particle can produce sufficient transition radiation to be detected. The amount of radiation produced at each boundary is proportional to $1/(mc)^2$, so that the measured radiation can be used to discriminate low-mass objects (such as electrons) from higher-mass objects (such as pions and other hadrons), which produce less radiation.

The TRD consists of three concentric layers, with each layer containing a chamber in which the transition X-rays are radiated and a chamber in which these X-rays are detected. The radiation region of each layer contains 393 18μm thick polypropylene foils, concentrically arranged and spaced by 150μm[47]. The spacings are filled with nitrogen gas. The detection chamber consists of two-stage drift chambers filled with a Xenon gas mixture. These chambers span the length of the TRD and are sectioned in ϕ, with the inner two layers containing 256 readout wires and the outer layer containing 512 readout wires[44]. The detector chamber is separated from the radiation chamber by two concentric mylar sheets. The gap between the sheets is filled with CO_2 to prevent the nitrogen from contaminating the xenon gas mixture[48].

X-rays produced in the radiation chamber pass radially outward into the first stage of the drift chambers. Here most of the X-rays convert, and the

conversion electrons drift radially outward, through a grid of ground wires, to the second stage. Additional electrons are produced through ionization of the medium by the particle passing through the drift chambers (similar to the VTX). The electrons induce avalanches in the second stage, where charge is collected on the sense wires. Copper strips, helically arranged on the drift chamber wall, are used to measure the z position of the particle[44].

Time and charge measurements are used in the identification of isolated electrons. The TRD gives an electron-to-pion rejection of 50. Some TRD parameters are listed in Table 3.2[44][47].

Table 3.2. Parameters for DØ Transition Radiation Detector

Parameter	**Specification**
Radius	17.6 cm - 47 cm
Overall Length	165 cm
Number of Layers	3
Number of Sense Wires	256,256,256 (for Layers 1,2,3)
Sense Wire Voltage	+1.6 kV
Drift Field	0.7 kV/cm
Gas Type	Radiation Chamber - N_2
	Gap - CO_2
	Drift Chamber - 95% Xe+7% CH_4+2% C_2H_6
X-ray energy	$<$ 30keV

3.4.3 Central Drift Chamber (CDC)

The CDC is the outermost of the central tracking chambers, residing radially between the TRD and the Central Calorimeter cryostat. Like the VTX and TRD, the CDC is cylindrical in shape, 184 cm in length and extending radially outward from z=49.5 cm to z=74.5 cm. It provides charged-particle track coverage out to $|\eta|$=1.2[44].

The CDC contains four layers of structurally-independent drift chamber modules, with each layer consisting of 32 modules arranged in ϕ. The modules are offset in ϕ by one-half of a module from layer to layer to improve track resolution. Each module contains 7 sense wires, aligned radially and running the length of the CDC, which are read out at one end[45]. Adjacent wires are staggered in ϕ by $\pm 200\mu$m (to further improve track resolution). Each module also contains two delay lines, one at either end of the sense wire array (embedded in the module wall) and oriented parallel to the sense wires[45]. These are read out at both ends. When an avalanche occurs in the vicinity of the sense wires at either end of the sense wire array, a pulse is induced in the corresponding delay line. The timing of this pulse is used to measure the z coordinate of the hit. The $r\phi$ coordinate of a hit is measured by the drift time and sense wire position, similar to the VTX. The CDC parameters are listed in Table 3.3[44][47].

Table 3.3. Parameters for DØ Central Drift Chamber

Parameter	**Specification**
Radius	51.8 cm - 71.9 cm
Overall Length	179.4 cm
Number of Layers	4
Number of Cells	32 per layer
Number of Sense Wires	7 per cell (896 total)
Sense Wire Voltage	+1.45 kV (inner sense wires)
	+1.58 kV (outer sense wires)
Drift Field	620V/cm
Drift Velocity	34μm/ns
Gas Type	93% Ar+4% CH_4+3% CO_2 +0.5% H_2O
Gas Gain	2×10^4 (inner sense wires)
	6×10^4 (outer sense wires)
Spatial Resolution	$r\phi \simeq 180\mu$m, $z \simeq 2.9$ mm

3.4.4 *Forward Drift Chambers (FDC)*

The FDC extends the tracking capabilities down to $\theta \simeq 5°$ with respect to the beamline, corresponding to $|\eta| \simeq 3.1$[47]. The FDC is made of a set of three drift chambers oriented perpendicular to the beam line (and also perpendicular to the rest of the tracker). There are two of these sets, one located at either end of the central tracker in z. The layout of the chambers is shown in Fig. 3.4.

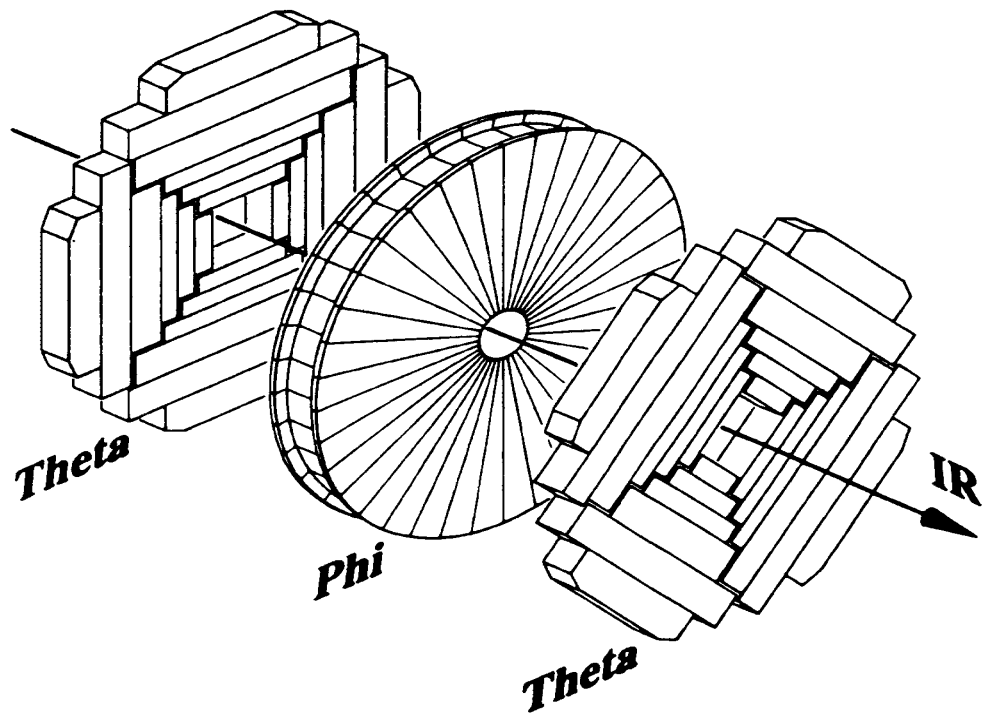

Figure 3.4. Layout of one set of FDC chambers

The Φ module is separated into 36 cells in ϕ, each cell containing 16 sense wires extending radially outward from the beam line[44]. The Θ modules are comprised of four independent chambers. Each chamber has six cells, and each cell has eight sense wires that are oriented perpendicular to the Φ module sense

wires. As in the CDC, adjacent sense wires are offset by 200μm[45]. Each cell in the Θ module also contains one delay line to provide additional position information along the length of the cell[47].

The gas mixture in the FDC is the same as in the CDC, with similar drift field and gas gain. The FDC parameters are summarized below in Table 3.4[44][47].

Table 3.4. Parameters for DØ Forward Drift Chambers

Parameter	**Specification**
Radius	11 cm - 62 cm
Overall Length	$z = \pm$(104.8 cm - 135.2 cm)
Number of Modules	6 (4 Θ, 2 Φ)
Number of Cells	24 in each Θ module
	36 in each Φ module
Number of Sense Wires	8 per cell in each Θ module
	16 per cell in each Φ module
Sense Wire Voltage	+1.55 kV Θ modules
	+1.66 kV Φ modules
Drift Field	1kV/cm
Drift Velocity	40μm/ns Θ modules
	37μm/ns Φ modules
Gas Type	93% Ar+4% CH_4+3% CO_2 +0.5% H_2O
Gas Gain	2.3×10^4 inner Θ sense wires
	5.3×10^4 outer Θ sense wires
	3.6×10^4 Φ sense wires
Spatial Resolution	$\theta \simeq 300\mu$m, $\phi \simeq 200\mu$m

3.5 Calorimeter

The DØ calorimeter is the set of detectors used to measure the energies of particles produced in the hadronic collisions. Good calorimetry is essential to DØ in the absence of a central magnetic field. The calorimeter energy measurements provide all of the kinematic information for electrons, photons, jets,

and neutrinos. Additional information related to the development of particle showers within the calorimeter is also used in the identification of electrons, photons, jets, and muons[44]. A cutaway view is shown in Fig. 3.5.

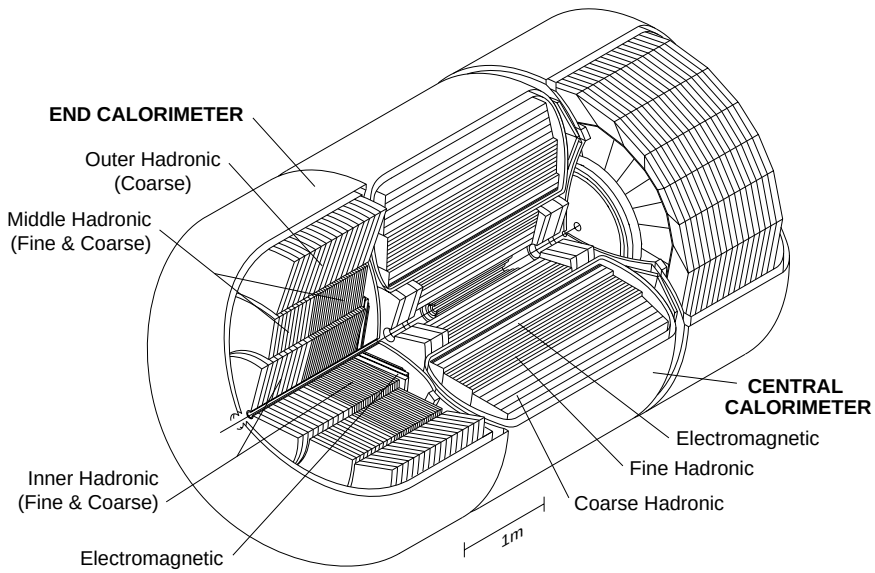

Figure 3.5. The DØ calorimeters, showing the central and the two end-cryostats and the various calorimeter subsystems.

The DØ calorimeter is a *sampling* calorimeter, which means that particle energies are not directly measured in whole, but rather are inferred from a series of measurements of samples of particle energies. This is accomplished through consecutive layers of dense (high Z) absorbing material, in which a traversing particle loses much of its energy, separated by some ionizing medium, in which a fraction of the remaining energy is measured. At DØ the absorbing material is typically Uranium, and the ionizing medium is liquid Argon. Fig. 3.6 depicts the standard configuration for calorimeter cells.

A unit calorimeter cell consists of one absorber plate (thickness varies), fol-

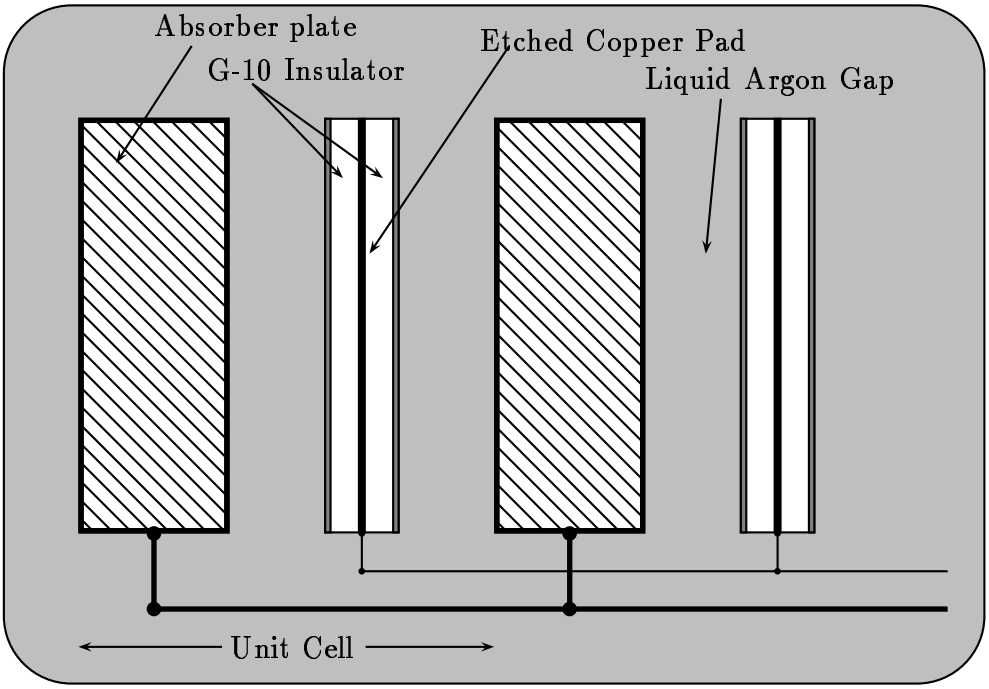

Figure 3.6. Unit calorimeter cell

lowed by a liquid Argon gap of 2.3 mm, followed by a readout board, and lastly another 2.3 mm liquid Argon gap[49]. The readout board is constructed of two G-10 sheets glued together. The outside of each sheet is coated with resistive epoxy. The inside of one sheet is copper-clad, with a fine grid pattern milled into the copper (the other sheet is bare on the inside). The absorber plates are grounded, while the resistive coating is charged to $\sim$2.0 kV. A particle traversing the calorimeter passes through the absorber, where low-energy secondary particles are emitted through interaction with the Uranium. This process is called *showering*. These shower particles then ionize the liquid Argon as they cross the gap to the next absorber plate. The ionization electrons drift toward

the readout board, where the charge is collected on the copper cladding and read out. Each square on the copper cladding, as defined by the grid pattern, helps define the location, in (η, ϕ) space, of the shower. A square in a particular readout board is typically ganged together with the square in the same location on one or more consecutive readout boards to form a *readout cell.*

The fraction of energy that is measured by the readout cells is known as the *sampling fraction.* Sampling fractions were measured for each layer of readout cells in a test beam, yielding values of 1-10%. The energy of a particle or group of particles is reconstructed by multiplying the energy in the readout cells by the appropriate sampling weight and then summing the depositions in several layers of readout cells.

High energy electrons and photons interact within the absorbers primarily through bremsstrahlung and pair production. These processes are complementary, meaning that bremsstrahlung results in photons which then undergo pair production and pair production results in electrons and positrons which then undergo bremsstrahlung. With each interaction, the particle multiplicity increases and the mean energy per particle decreases. At sufficiently low energies, ionization losses dominate for electrons and Compton scattering dominates for photons. The showers resulting from these processes are called *electromagnetic*, or EM, showers. The energy loss of an EM particle is exponential as a function of longitudinal distance d traversed, and is expressed by[50]

$$E(d) = E_0 e^{-\frac{d}{X_0}}, \tag{3.5}$$

where E_0 is the initial particle energy, X_0 is the *radiation length*, a constant of the material. For Uranium, $X_0 \simeq 3.2$ mm.

High energy hadrons, unlike electrons and photons, interact within the absorbers through inelastic collisions with the Uranium nuclei, producing secondary particles which also undergo such inelastic collisions. The resulting shower is called a *hadronic* shower. The energy loss of a hadron over some distance d is expressed by[50]

$$E(d) = E_0 e^{-\frac{d}{\Lambda_I}}, \tag{3.6}$$

where Λ_I is the *nuclear absorption length*, which for Uranium has a value of $\simeq 10.5$ cm.

Since $X_0 < \Lambda_I$, the EM showers develop over a much shorter distance than hadronic showers do. For this reason, the first several layers of the calorimeter are closely spaced and are designed for accurate measurement of EM energy. The outer layers are spaced farther apart and are used to measure hadronic energy.

The response of the calorimeter to electromagnetic energy as compared to the response to hadronic energy is called the e/π ratio. Ideally, this ratio should equal 1. This is desirable because, in any hadronic cascade passing through the calorimeter, there is likely to be some EM component to due neutral pions which decay into photon pairs. Therefore, deviations of the e/π ratio from 1 degrade the energy resolution. In general, the response of the calorimeter to electrons and photons is higher than the response to hadrons, so that $e/\pi > 1$. This is partly due to the negative binding energy of the nuclei that the hadrons collide with, and partly due to the fact that some of the secondary particles produced in these collisions, such as muons and neutrinos, cannot be measured by the calorimeter[50]. At DØ this problem is corrected partially by

the Uranium itself (energy is released through nuclear fission) and partially by varying the ratio of absorber thickness to argon gap thickness. The e/π ratio at DØ is about 1.11 for 10 GeV energies, falling to 1.04 for 150 GeV energies[44].

3.5.1 Calorimeter Structure

The presence of liquid argon (T = 78 K) necessitates the use of stainless steel cryostats to house all of the calorimeter. Since the calorimeter completely envelopes the tracking system (see Fig. 3.5) and access to the tracker must be allowed, the calorimeter system is divided into three structurally independent cryostats[44]. There is one Central Calorimeter cryostat and two Endcap Calorimeter cryostats. Overall, the calorimeter is about 8m in length and 5m in diameter. The cryostats are all welded shut, so there is no access to calorimeter components during running. Each cryostat has four insulated feedthrough ports for the passage of the signal cables and two feedthrough ports for the passage of high voltage, temperature, and purity-monitoring cables.

The cell structure of the calorimeter can be seen in Fig. 3.7. Readout cells are aligned in projective towers, as shown by the alternating grey and white coloring of the cells in the figure. These projections point back toward the detector center, at z=0.0. The cell sizes are determined by this geometry and by shower depth, so that the EM cells are ~1-2 cm across while the hadronic cells increase in size up to ~10 cm across. It is more convenient to measure in units of η and ϕ, however. Each cell typically measures 0.1 units of η by 0.1 radians in ϕ, written as $\Delta\eta \times \Delta\phi = 0.1 \times 0.1$. Therefore, each tower also measures 0.1×0.1 in (η, ϕ) space. The scale of numbers on the border of Fig. 3.7 shows units of η, and therefore the locations of the towers as a function of η. For every 0.1 division of η there are 64 towers covering the full range of ϕ.

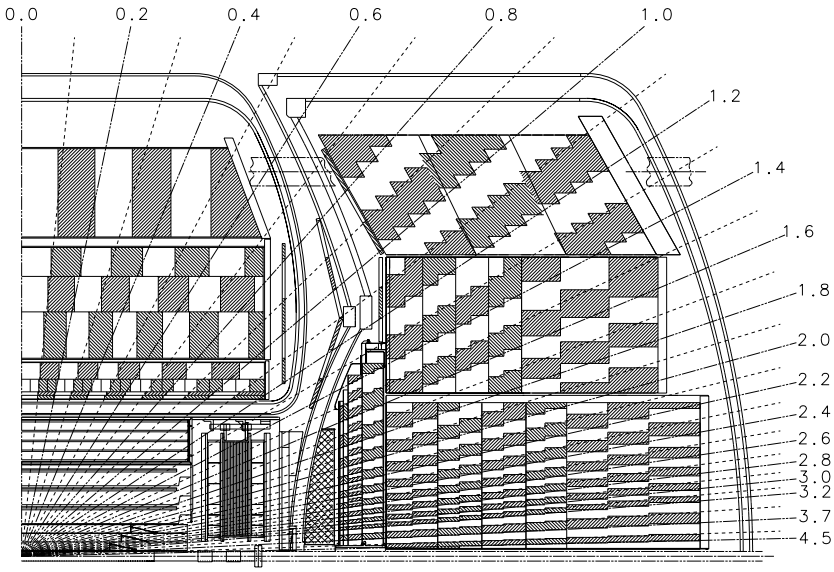

Figure 3.7. Side view of one-fourth of the calorimeter, showing projective cell structure for successive layers.

Specifics of the Central Calorimeter and Encap Calorimeters are discussed in the following sections.

3.5.2 Central Calorimeter (CC)

The CC is the calorimeter system surrounding the Central Tracker. It provides coverage out to $|\eta| \leq 1.0$. Its shape is approximately cylindrical, with readout layers stacked in r (concentric). The first four layers of the CC (closest to the beam pipe) are devoted to EM measurement. They are placed at depths of 2, 4, 11, and 21 X_0 interaction lengths, respectively, from the inner cryostat wall[44]. The layers are all segmented into cells of 0.1×0.1, with the exception of the third layer. The third layer is where the maximum shower development occurs, and so the segmentation is increased to 0.05×0.05 to allow for more accurate measurement of the location and shape of the shower. The absorbers

in the EM layers are 3mm thick Uranium plates[44]. The total material depth of the EM layers is $21X_0$, which is about $0.76\Lambda_I$[47].

Following the EM layers radially are the Fine Hadronic (FH) layers. There are three readout layers, with thicknesses of 1.3, 1.0, and 0.9 nuclear absorption lengths, respectively[44]. The segmentation in all layers is 0.1×0.1. The FH layers use 6mm thick absorber plates of Uranium doped with 1.7% niobium[47]. The total depth of the FH section is $3.2\Lambda_I$[47].

The last layer is the Coarse Hadronic (CH) layer. It is a single readout layer, $3.2\Lambda_I$ in thickness[44]. Its primary goal is to provide total absorption of the particles within the calorimeter volume and measure the tail of the calorimeter shower. The absorber used in the CH layer is 46.5mm thick copper instead of Uranium, to conserve cost[44].

Table 3.5. Parameters for DØ Central Calorimeter

Module Type	**EM**	**FH**	**CH**
Rapidity Coverage	$\pm\,\|1.2\|$	$\pm\,\|1.0\|$	$\pm\,\|0.6\|$
Absorber Material	Ur	Ur (1.7%Nb)	Cu
Absorber Thickness	2.3 mm	2.3 mm	46.5 mm
Number of Readout Layers	4	3	1
Depth per Readout Layer	2, 2, 7, 10 X_0	1.3, 1.0, 0.9 Λ_I	$3.2\Lambda_I$
Total Radiation Lengths (X_0)	21	96	33
Total Nuc. Abs. Lengths (Λ_I)	0.76	3.2	3.2
Sampling Fraction	11.79%	6.79%	1.45%
Segmentation ($\Delta\eta\times\Delta\phi$)	0.1×0.1 (Layers 1,2,4) 0.05×0.05 (Layer 3)	0.1×0.1	0.1×0.1
Total Number of Channels	10,368	3000	1224

3.5.3 Endcap Calorimeters (EC)

The Endcap Calorimeters are located fore and aft of the CC and provide coverage in the range $1.1<|\eta|<4.0$. Like the CC, the EC contains separate layers for EM and hadronic calorimetry. The EC structure is very different from the CC, however, in that the layers are stacked in z instead of r. Thus, the geometry of the EM and hadronic layers differs from their CC counterparts.

The modules containing the EM layers (ECEM) are disk shaped, placed facing the CC, with an inner radius of 5.7cm and an outer radius of 104cm[49]. The absorbers for the EM layers are 4mm thick Uranium plates[49]. There are four readout layers with thicknesses of 0.3, 2.6, 7.9, and 9.3 X_0, respectively[44]. In general, the cell segmentation for layers 1, 2, and 4 is $\Delta\eta \times \Delta\phi = 0.1\times0.1$, while the third layer is segmented more finely, 0.05×0.05. However, at higher values of $|\eta|$, cell sizes become too small to permit this. Beyond $|\eta| = 2.6$, the segmentation of the third layer is increased to the same size as the other three as a result. Beyond, $|\eta| = 3.2$, the segmentation increases again, to 0.2×0.2, for all layers. This increase continues for successively higher values of $|\eta|$ to 0.4×0.4 at $|\eta|=4.0$, the farthest extent of the ECEM. The total depth of the ECEM is $\sim$20 X_0[47].

Directly behind the ECEM is the inner hadronic module. It is shaped like a cylinder, with the layers facing perpendicular to the beamline. The inner radius of the structure is 3.92 cm and the outer radius is 86.4 cm[49]. There are five readout layers in this module, four fine hadronic layers (IFH) and one coarse hadronic (ICH) layer. The IFH layers each use two semiannular absorber plates of 6mm thick Uranium infused with a small amount of Niobium[49]. The absorbers in consecutive layers are rotated by $\pi/2$ in ϕ to avoid dead regions.

The layer thickness is about $1.1\Lambda_I$ for each layer, for a total of $4.4\Lambda_I$ for the whole IFH[49]. The single ICH layer is about $4.1\Lambda_I$ deep and uses 46.5mm thick stainless steel plates as the absorber. The ICH serves the same purpose as the CCCH, to contain particles within the calorimeter and complete the energy measurement.

Surrounding the inner hadronic module in ϕ is the middle hadronic module. Its structure is very similar to the inner hadronic module, having four readout layers of fine hadronic calorimetry (MFH) and one for coarse hadronic calorimetry (MCH). The absorbers are similar to the inner hadronic module as well.

The outermost module in ϕ is the outer hadronic module, or OH. It contains three layers of coarse hadronic calorimetry. Steel absorber plates are used for all layers. This is the only module in which the layers are not oriented perpendicular to the beam axis. Rather, they are inclined at an angle of about 60° with respect to the beam axis to provide better coverage in η. See table 3.6 for general parameters relating to the Endcap Calorimeters[44][49][47].

3.5.4 Intercryostat Detector (ICD) and Massless Gap (MG)

Examination of the module structure in Fig. 3.7 reveals a large gap in calorimeter coverage in the region between the CC and EC. This is due primarily to the cryostat walls, module endplates, and support structures. This uninstrumented region begins near $|\eta|$=0.8, where the CCFH coverage begins to fall away, and extends to $|\eta|$=1.4 where the CCEM begins. While there is no point in this region at which there is *no* coverage, nevertheless the ability to accurately measure particle energies there is sufficiently compromised as to warrant the inclusion of additional calorimetry measures to compensate for the gaps.

Table 3.6. Parameters for DØ Endcap Calorimeters

Module Type	**ECEM**	**IFH**	**ICH**
Rapidity Range	$\pm\ \lvert 1.3\text{–}4.1 \rvert$	$\pm\ \lvert 1.6\text{–}4.5 \rvert$	$\pm\ \lvert 2.0\text{–}4.5 \rvert$
Absorber Material	Ur	Ur (1.7%Nb)	Steel
Thickness (mm)	4.0	6.0	46.5
Number of Layers	4	4	1
Total Depth	20 X_0	4.4 Λ_I	4.1 Λ_I
Sampling Fraction	11.9%	5.7%	1.5%
Total Number of Channels	7488	5216[1]	
Module Type	**MFH**	**MCH**	**OH**
Rapidity Range	$\pm\ \lvert 1.0\text{–}1.7 \rvert$	$\pm\ \lvert 1.3\text{–}1.9 \rvert$	$\pm\ \lvert 0.7\text{–}1.4 \rvert$
Absorber Material	Ur (1.7%Nb)	Steel	Steel
Absorber Thickness (mm)	6.0	46.5	46.5
Number of Layers	4	1	3
Total Depth	3.6 Λ_I	4.4 Λ_I	4.4 Λ_I
Sampling Fraction	6.7%	1.6%	1.6%
Total Number of Channels	1856[2]		960

One of these measures is the addition of two disk-shaped scintillation counter arrays mounted on the outside surface of inner EC cryostat walls (visible in Fig. 3.7). Since they are located in the region between the EC and CC cryostats, they are termed the Intercryostat Detectors, or ICD's. There is one ICD for each EC. Each array is constructed of Bicron-408 tiles[44], cut to match the projective cell structure so that each tile is of dimension $\Delta\eta \times \Delta\phi = 0.1 \times 0.1$. Each tile has three or four 3mm grooves milled into the surface, in which bundles of 200μm diameter polystyrene fibers are placed[44]. These fibers act as wave-shifters and waveguides, carrying the scintillation light to phototubes mounted behind the tiles.

The other addition is a set of extra readout boards mounted within the cryostats, the Massless Gaps. The MG readout boards are of standard DØ construction, but there are no absorber plates. Each MG consists of two such

boards, with standard corresponding cell structure (0.1×0.1), separated by a liquid argon gap. The two boards are ganged together to form one readout layer. There are a total of six MG structures, three in each half of the detector. There is one MG mounted on each end of the CCFH module, one on the inner wall of each ECMH module (radially just outside the EM disks), and one on the inner wall of each OH module. Each MG, like all other calorimeter sections, wraps around the beam to cover the entire range of ϕ.

3.5.5 Calorimeter Readout

Signals from the calorimeter modules are transmitted via coax cables to the four feedthrough ports in each cryostat. Charge-sensitive preamplifiers mounted on the cryostats receive the signals from the ports and send them to baseline subtraction circuit (BLS) modules. The BLS shapes the signal, amplifies it by either $\times8$ or $\times1$ (depending on signal size), and splits it into two components, one fast and one slow. The signals from the readout cells in the fast component are summed to form 0.2×0.2 signal towers. Only EM and FH signals are used for these towers. This portion of the signal is then used in event selection (see section 3.7). The slow component is sent to the ADC circuits, where it is digitized for readout to tape.

3.5.6 Calorimeter Performance

The performance of the calorimeter modules was studied extensively with test beam pions and electrons of energies from 10 GeV to 150 GeV. The full CC was tested with cosmic rays before the final detector assembly.

For energies measured in GeV, the energy resolution of the calorimeter can

be parameterized as[44]

$$(\frac{\sigma_E}{E})^2 = C^2 + \frac{S^2}{E} + \frac{N^2}{E^2}, \tag{3.7}$$

where C represents a constant error due to calibration errors, deviation of the e/π ratio from unity, and inhomogeneities in the calorimeter, S represents sampling fraction errors, and N represents error due to noise. For low energies, the noise term dominates. At higher values of energy, the sampling fraction dominates, and the resolution is improved. The resolution continues to improve as the energy rises further, until the sampling fraction and noise contributions are effectively zero. At the highest energies, the best attainable resolution is dictated by the value of C.

The resolution parameters for a selection of calorimeter modules are shown in table 3.7 and are representative of the calorimeter as a whole[44][47][49].

Table 3.7. Resolution parameters for some calorimeter modules

Module	**C**	**S**	**N**
CCEM	0.003±0.004	0.162±0.011	0.14
ECEM	0.003±0.003	0.157±0.006	0.29
MFH	0.047±0.005	0.439±0.006	1.28

Position resolution in the calorimeter is also very important at DØ, particularly in the study of electromagnetic objects such as electrons and photons. The shape of particle showers in the EM layers of the calorimeter is used to distinguish electrons from highly electromagnetic jets and to distinguish direct photons from neutral pions that have undergone conversion in flight. The position resolution in the EM layers is 0.8-1.2 mm, varying approximately as

$1/\sqrt{E}$[44].

3.6 Muon System

Since, muons have relatively long lifetimes ($\sim$2.2μs), they are unlikely to decay within the volume of the calorimeter. They do not interact strongly, like hadrons do, and their large mass severely restricts their ability to induce an electromagnetic shower in the EM layers. Therefore, muons are likely to escape the calorimeter undetected (except as minimum ionizing particles) and so a separate detector, encompassing the calorimeter (and CD), is needed to identify them and measure their momenta.

The DØ muon system, shown in Fig. 3.8, uses a system of proportional drift tubes (PDT's) and track-bending magnets to locate muons emerging from the calorimeter[44]. There are three sets of PDT's. The first set consists of four readout layers and resides just outside the calorimeter. Its purpose is to determine the location and direction of emerging muons, using additional information provided by the central tracker and the vertex measurement[51].

Surrounding the first set of PDT's are five iron toroidal magnets, which provide a field strength of $\simeq$ 2T[51]. These provide the bend necessary to measure muon momenta. They also are used to absorb any hadrons that escape the calorimeter and induce hits in the first layer of PDT's.

Outside the magnets are two additional sets of PDT's, with three readout layers each. Tracks are measured in these PDT's and compared to the initial track from the first layers - the angular bend is used to calculate the muon

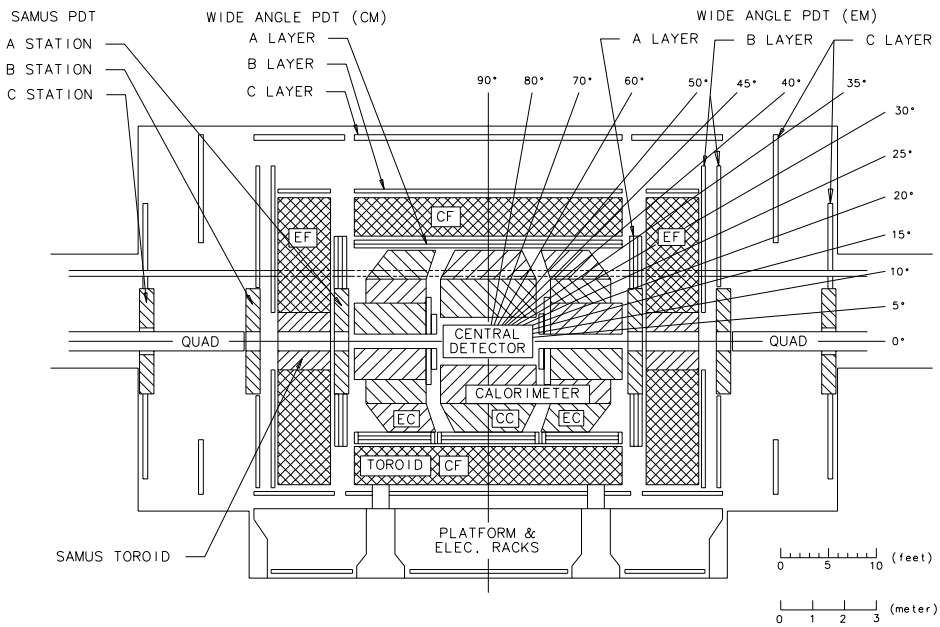

Figure 3.8. The DØ muon system

momentum. The momentum resolution is parameterized by[44]

$$(\frac{\delta p}{p})^2 = 0.18^2 + (0.01p)^2, \tag{3.8}$$

with p measured in GeV/c. The first term represents the contribution from the drift chamber resolution and dominates the expression for low momenta. The second term represents resolution limitations from multiple coloumb scattering in the iron toroid. This term degrades the overall resolution for higher muon momenta.

3.7 Data Acquisition

At the DØ interaction region, $\overline{p}p$ crossings occur about every 3.5 μs., or at a rate of ~285kHz[44]. At typical Run 1B luminosities [3], one or more $\overline{p}p$ collisions will occur at almost every crossing. Only a very small fraction of these collisions yield interesting events, however. Furthermore, the rate at which events can be written to tape is only a few Hz, far below the collision rate. Therefore, it is necessary to have some system for flagging only the interesting events to be read out and stored for analysis. DØ uses a complex, multi-tiered triggering system for this purpose. Each successive tier, or level, is increasingly sophisticated and reduces the event rate by vetoing candidate events against a collection of requirements. There are three levels in the trigger system, numbered 0, 1, and 2. There is also a Level 1.5 trigger system, a subset of the Level 1 trigger used for muons. Only events which pass the Level 2 triggers are kept. The individual level components are described briefly below.

3.7.1 Level 0

Mounted on the inner surface of each Endcap cryostat, at a distance of 140 cm from the center of the detector, are two sets of scintillation counters. These are square-shaped arrays that provide partial coverage in ϕ from $1.9 < |\eta| < 2.3$ (due to the square geometry) and full coverage from $2.3 < |\eta| < 3.9$[47]. Photomultiplier tubes are used for detection of scintillation light.

When an inelastic $\overline{p}p$ collision occurs during a beam crossing, spectator interactions result in high particle multiplicity in the far forward regions (high η). These particles are detected in the Level 0 counters, which signal the Level

[3] Luminosity is a measure of the event rate, adjusted for cross sections, written in units of $cm^{-2}s^{-1}$

1 trigger that an inelastic interaction has occurred.

The Level 0 counters are also used to make a preliminary measurement of the z vertex, by using the time difference between the signals from both ends of the detector. The signals from the PMT's are split into two paths. One path passes the signals to a digital TDC which makes a fast calculation of the z vertex. This measurement is obtained within 800 ns of the interaction and has a resolution of 15cm[44]. The second path is used to make a more careful, but slower, determination of the vertex. The slower z vertex is calculated within 2.1μs and has a resolution of 3.5cm[44]. The fast vertex is used to eliminate events triggered by the Level 0 counters that are due to beam-gas or beam-halo interactions. These types of events typically occur far from the detector center, so a cut of $|z| <$100 cm is used to remove them. The fast vertex measurement is also used by the Level 1 trigger system to compute relevant event parameters in physics coordinates (see section 3.2). The slow vertex measurement is used by the Level 2 system for the same purpose.

At high luminosities, there is a large probability that more than one inelastic collision will occur in a beam crossing. These are known as multiple interactions. At a luminosity of $1\times10^{31}\mathrm{cm}^{-2}\mathrm{s}^{-1}$ for example, the average number of inelastic collisions per crossing is 1.5[52]. When multiple interactions occur, the time difference information from the Level 0 scintillation counters is ambiguous, causing a multiple interaction flag to be set, which is then passed on to the other trigger systems.

The last utility of the Level 0 counters is the calculation of the luminosity. This is derived from the measurement of the rate of inelastic collisions and knowledge of the cross section for inelastic collisions.

3.7.2 Level 1

The Level 1 trigger system is a framework of hardware logic circuits controlled by software. It is designed to make requirements on all events passed to it from Level 0 and keep only those events that contain potentially interesting information. The event information comes from a coarse, fast reconstruction of the event based on calorimeter information from the BLS and on similar muon information. The decision time must be less than the time between beam crossings (3.5μs) to avoid deadtime.

The calorimeter cell information is reconstructed into coarse trigger towers of size $\Delta\eta \times \Delta\phi = 0.2 \times 0.2$[47]. The energy and E_T for each tower is computed, as well as the electromagnetic and hadronic components of each. The E_T sum of all trigger towers is used to make a rough determination of $\not{E}_T$ in the event. The muon PDT hit information is reconstructed into tracks in the muon system. Level 1 uses a list of requirements, called the trigger menu, to pass or veto an event. The trigger requirements can be changed easily by changing the trigger menu in the software. A typical trigger might require a trigger tower with at least 10 GeV of electromagnetic energy, for example, or $\not{E}_T$ >15 GeV.

If an event passes a Level 1 muon trigger, the muon information is passed to a special trigger subsystem, the Level 1.5 trigger. Muon momentum, which is too time-costly to be evaluated for every event, is calculated in the Level 1.5 system. An additional trigger menu is used at Level 1.5 based on muon momentum. Events which pass any of the Level 1 triggers (there are typically about 30 in the trigger menu) are passed to Level 2, where more exacting requirements are made.

3.7.3 Level 2

The Level 2 system consists primarily of a farm of 48 VAXstation nodes that work in parallel to reconstruct an event passed from Level 1[47]. Level 2 uses information from all detector systems in its reconstruction and attempts to roughly identify actual objects in an event, such as jets, electrons, photons and muons. Level 2 has its own trigger menu with which to make pass/fail decisions on candidate events. The Level 2 trigger menu is much larger than the Level 1 menu and is changed more frequently. There are about 90 sets of requirements (triggers) in the Level 2 menu. An example Level 2 trigger might be one that requires two reconstructed jets with E_T >40 GeV or one that requires a reconstructed electron and muon with E_T >20 GeV.

If an event passes at least one Level 2 trigger, the entire event is written to a temporary disk, from which it is copied to 8 mm tape. The events on tape are then fully reconstructed offline at a later time. A small fraction of the events, however, are reconstructed online and examined during running to monitor the event quality.

The requirements made of the data pertinent to this analysis, the selection of $W + jets$ candidates, are made offline and are discussed in the next chapter.

CHAPTER 4

ACQUIRING THE DATA SETS

Acquiring useful and manageable data for analysis requires many levels of processing. Raw data from the detector (containing information in the form of ADC counts, pulse heights, and the like) deemed interesting by the trigger framework are reconstructed offline into several useable formats. The data are then divided into subsets, or *streams*, each containing similar types of events, and stored on data tapes. Using a set of loose cuts, candidate events for the analysis are stripped from the appropriate streams and stored on disk. Lastly, a tighter set of cuts is used in the analysis software itself to identify the final list of events to be processed.

4.1 The W Decay Mode Selection

As stated in Chapter 1, this analysis uses events with a W boson and an opposing jet in the study of color coherence effects. Although the jet ensemble may be observed directly through calorimeter measurements, the W must be identified through its decay products. The primary W boson decay modes are

$$\begin{array}{l} W^{\pm} \rightarrow e^{\pm} + \nu \\ W^{\pm} \rightarrow \mu^{\pm} + \nu \\ W^{\pm} \rightarrow \tau^{\pm} + \nu \\ W^{\pm} \rightarrow q\bar{q}' \end{array} \tag{4.1}$$

The $W^{\pm} \rightarrow e^{\pm} + \nu$ decay mode is the only one used for the color coherence $W+$ *jets* data set. The third and fourth decay modes have associated *background* rates that are prohibitive, so that a reasonably pure sample of W boson events would not be attainable. The term *background* refers to events that do not contain some particular specific physics process (such as $W^{\pm} \rightarrow e^{\pm} + \nu$) but which can be experimentally indistinguishable from events that do. The most obvious background contribution for the third and fourth decay modes are QCD dijet events, in which two partons are produced directly from the hard collision, rather than from a W or τ decay, and then fragment into jets. Since these types of events are produced copiously in the Tevatron, there is likely to be an abundance of QCD dijet events that possess kinematics similar to jets resulting from W or τ decay.

The $\mu\nu$ decay mode has much lower background contribution than either $\tau\nu$ or $q\bar{q}'$, but it is nonetheless approximately four times higher than the $e\nu$ decay mode[53]. Furthermore, the DØ muon triggers are far less efficient than the electron triggers, resulting in a much smaller event sample. Lastly, the DØ muon system does not provide full coverage in ϕ, so that a sample of $W^{\pm} \rightarrow \mu^{\pm} + \nu$ events will not be distributed uniformly throughout the detector. The $W^{\pm} \rightarrow e^{\pm}\nu$ decay mode is therefore the logical choice for obtaining a useful and reasonably pure W boson sample with high statistics.

All of the data for this study are from the 1994-1995 Run 1B global event sample. The reconstruction and selection of these events is described in the following sections.

4.2 Offline Reconstruction and Streaming

The minimal reconstruction performed by the Level 2 trigger software[1] is sufficient only for determining which events merit further analysis and which may be discarded. Data that pass any of the Level 2 triggers are written to tape for full reconstruction offline.

The full reconstruction is performed by a farm of Silicon Graphics processors using the DØRECO software package. DØRECO reconstructs tracks in both the central tracker and muon system using pulse height information from the hit wires, reconstructs the event vertex (or vertices) using the Level 0 and tracking information, and converts all calorimeter cell information into energy units (GeV) and then uses the cells to form calorimeter towers (see Chapter 3 for tower description). DØRECO then uses all of this information to attempt to identify specific objects in the event, such as jet, muon, electron and photon candidates, with specific algorithms. The algorithms for jet, electron, and neutrino candidates are described here due to their relevance in the color coherence event selection.

4.2.1 Jet Reconstruction

Jet candidates are reconstructed using the DØ cone algorithm, an iterative algorithm that locates calorimeter energy clusters and calculates E_T-weighted centroids for them. The first step in the process is the formation of preclusters. Preclusters are found by locating all calorimeter towers with $E_T > 1GeV$ (called *seed towers*) and adding contiguous towers within a radius $R = 0.3$, with R

[1]See Chapter 3 for a description of the trigger framework

defined as

$$R = \sqrt{(\eta_{seed} - \eta_t)^2 + (\phi_{seed} - \phi_t)^2}. \tag{4.2}$$

In this expression, $(\eta_{seed}, \phi_{seed})$ defines the seed tower location and (η_t, ϕ_t) defines the locations of the rest of the precluster towers. All locations are expressed in physics coordinates. An E_T-weighted centroid, $(\eta_{clus}, \phi_{clus})$, is calculated for each precluster using the definitions[54]

$$\begin{aligned} \eta_{clus} &= \frac{\sum_i E_{T_i} \eta_i}{\sum_i E_{T_i}} \\ \phi_{clus} &= \frac{\sum_i E_{T_i} \phi_i}{\sum_i E_{T_i}} \end{aligned} \tag{4.3}$$

where i sums over all towers within the precluster.

A cone of radius R_{jet}, extending from the interaction vertex, is drawn around each precluster. At DØ four cone sizes are used for jet reconstruction: 0.3, 0.5, 0.7, and 1.0. For each precluster, the E_T is summed for all towers within the cone and a new $(\eta_{clus}, \phi_{clus})$ is calculated using Eqs. 4.3. New cones of radius R_{jet} are drawn around each new centroid and the process is repeated, resulting in another new set of precluster centroids. This process continues until successive iterations produce no centroid deviations, i.e. until the jet centers are all stable.

Upon completion of the cone iteration, the centroid for each precluster (now called jet candidates) is recalculated as[54]

$$\begin{aligned} \eta_{jet} &= -\ln[\tan(\theta_{jet}/2)] \\ \phi_{jet} &= \arctan \frac{\sum_i E_{y_i}}{\sum_i E_{x_i}} \end{aligned} \tag{4.4}$$

where

$$\begin{aligned}
\theta_{jet} &= \arctan \frac{\sqrt{(\sum_i E_{x_i})^2+(\sum_i E_{y_i})^2}}{\sum_i E_{z_i}} \\
E_{x_i} &= E_i \sin(\theta_i)\cos(\phi_i) \\
E_{y_i} &= E_i \sin(\theta_i)\sin(\phi_i) \\
E_{z_i} &= E_i \cos(\theta_i)
\end{aligned} \tag{4.5}$$

It is possible that two jets overlap, which occurs any time their centers are $< 2R_{jet}$ apart. In this instance, the E_T in the overlap region is compared to the E_T of the less energetic jet. If the overlap E_T is more than 50% of the jet E_T, the two jets are *merged*; that is, their towers are summed to form a single jet and a new jet center is calculated. If the overlap E_T is less than 50% of the jet E_T, the jets are *split*; all towers in the overlap region are assigned to the nearest jet and new jet centers are calculated for each.

Finally, an E_T cut is applied to all jet candidates. All candidates with E_T>8GeV are stored with the event - the rest are ignored.

4.2.2 Electron Reconstruction

Electron candidates are defined as calorimeter clusters with a large fraction of energy deposited in the electromagnetic layers and an associated reconstructed track pointing from the event vertex. For electron candidates, electromagnetic (EM) towers are used in cluster formation. EM towers are standard $\Delta\eta\times\Delta\phi = 0.1 \times 0.1$ calorimeter towers, but containing only information from the four EM layers and the first FH layer.

Clusters are formed using the *nearest neighbor* algorithm. All towers are ordered in E_T and the first (highest E_T) tower is taken as the seed for the first cluster. All towers adjacent to this tower with $E_T > 50$MeV are added into

the cluster. Next, all towers with $E_T > 50$MeV adjacent to those towers are added into the cluster. This process continues until there are no more adjacent towers above the 50MeV threshold. The highest E_T tower not already part of the first cluster is chosen as the seed for the second cluster, and the process of including adjacent towers above threshold is repeated. This process iterates until all towers above threshold are included in a cluster.

All clusters with total E_T <1.5GeV are discarded as candidates. Additionally, the highest-E_T tower in each cluster is required to comprise at least 40% of the cluster E_T. Each cluster is also required to have at least 90% of its energy contained in the EM layers. The cut is applied as

$$\text{EM Fraction} = \frac{\sum_i (E_{EM1} + E_{EM2} + E_{EM3} + E_{EM4})}{\sum_i (E_{EM1} + E_{EM2} + E_{EM3} + E_{EM4} + E_{FH1})} > 0.9 \qquad (4.6)$$

where i sums over all towers in the cluster.

Lastly, for each cluster to survive as an electron candidate, there must be an associated track from the central tracker. Clusters without such an associated track are stored as photon candidates, which are not used in this analysis.

4.2.3 Missing E_T

Neutrinos are not directly observed in the DØ detector, but are measured through a vector summation of all cells in the calorimeter. By applying conservation of momentum, the summation should ideally just be the negative of the missing momentum, which may be ascribed to the neutrino. However, this strategy is not fully applicable in a hadronic collider. Colliding partons, in general, have differing momentum fractions, resulting in a boosted system.

The boost destroys momentum conservation in the z direction, and so the summation of cells is not useful for measuring p_z^ν, the neutrino z-momentum.

However, the transverse momentum of the neutrino (p_T^ν) is Lorentz invariant and can therefore be determined through the cell summation. This quantity is normally termed missing E_T ($\not{E}_T$), which is just the transverse energy required to satisfy conservation of transverse energy/momentum in the event.

Missing E_T is determined as follows:

$$\begin{aligned} \not{E}_x &= -\sum_i^N E_{x_i} \\ \not{E}_y &= -\sum_i^N E_{y_i} \\ \not{E}_T &= \sqrt{\not{E}_x{}^2 + \not{E}_y{}^2} \end{aligned} \tag{4.7}$$

where i sums over all N cells in the event. Note that some amount of $\not{E}_T$ is present in almost every event and does not always signal the presence of a neutrino. Any mismeasurement of energy, due to errors in calorimeter response or particles impacting the calorimeter in uninstrumented regions, for example, will lead to a nonzero $\not{E}_T$. In general, however, these result in small values of $\not{E}_T$ ($\sim$ few GeV), whereas the $\not{E}_T$ for an actual neutrino from a W boson decay is much higher ($\sim$ 40 GeV).

It is also useful to know the azimuthal angle of the missing E_T, as will become apparent in the description of the W boson reconstruction. The azimuth, $\phi_{\not{E}_T}$, is defined as

$$\phi_{\not{E}_T} = \arctan \frac{\not{E}_y}{\not{E}_x} \tag{4.8}$$

4.2.4 *Streaming the Data*

To reduce the amount of data a physicist must sift through in order to find a particular event or group of events, collider data are divided into streams, groups of data with similar characteristics. Most streaming is done during data taking – events that pass Level 2 are written to specific tapes depending upon which Level 2 trigger they pass. For example, all events with two jet candidates are put into the QCD stream, whereas all events with a high-p_T photon candidate are put into the GAM (for gamma) stream. Frequently, events are put into more than one stream, so that an event with two jet candidates and a photon candidate will be inserted into both the QCD and GAM streams. In fact, there is a global event stream, the ALL stream, into which all events are copied regardless of trigger.

Streams that are created offline, after the events have been processed by DØRECO, are called *offline streams*. These streams are generally much more specific in their requirements for member events, so that a simple Level 2 trigger is insufficient. Offline streams are culled from ALL stream data, where there are no trigger requirements to bias the data. The $W + jets$ data used in this study was taken from the HLP offline stream. The member events of this stream are required to have one electron candidate with E_T>15GeV and $\not\!\!E_T$ >15GeV. There were 15 different Level 2 triggers represented by the events in the HLP stream, with ~120k total events from the Run 1B ALL stream data.

In spite of the many triggers represented in the HLP stream, all of the events for this analysis were required to originate from a single trigger, EM1_EISTRKCC_MS. The Level 1 requirement for this trigger was a single electromagnetic tower with

E_T>10GeV. The Level2 requirements were:

- One EM cluster with E_T>20GeV
- Loose isolation cut
- Loose track match requirement
- $\not\!\!E_T$ >15GeV

The efficiency of this trigger is 100% for reconstructed electron candidates with E_T>25GeV[63].

4.3 The $W + jets$ Data Set

To acquire a useful set of $W + jets$ events, several cuts were placed on all events in the HLP stream. These cuts were designed to remove events in which the detector had malfunctioned during data-taking, to reduce the number of background events, and to select events with the greatest probability for single interaction during a beam crossing. Requirements were made on the condition of the Main Ring during each event to avoid spurious energy measurements that would affect the $\not\!\!E_T$ determination. Also, cuts were imposed independently on the jet candidates, electron candidates, and $\not\!\!E_T$. Lastly, cuts were made on the ensemble of objects in each event, such as the reconstruction of the W boson and its location with respect to the jets.

4.3.1 Main Ring Contamination

During normal Tevatron operation, the Main Ring is used continuously in the production of antiprotons to replenish those being used in the $\overline{p}p$ collisions (see Chap. 1). The Main Ring passes directly through the Coarse Hadronic

modules of the DØ detector at $\phi \simeq 1.7$ radians. When protons circulating in the Main Ring pass through the detector, significant amounts of energy (known as the Main Ring blast) are measured in the CH modules in the ϕ regions surrounding the Main Ring beam pipe. If a triggered Tevatron beam crossing occurs in coincidence with this blast, the additional energy contamination is sufficient to obscure most physics measurements and render the event useless. If a Main Ring Blast occurs within a few μsec before a triggered event, then the calorimeter preamps will not have had time to recover before the physics event, and large amounts of negative energy are measured in the Main Ring region. This results in large values of $\not{E}_T$, sufficient to overwhelm the E_T of any actual neutrino in the event and give a false neutrino signal if none is present.

To avoid Main Ring contamination, many of the Level 1 triggers veto on the timing of the Main Ring beam. The times at which protons are injected into the Main Ring and the times at which proton bunches pass through the detector are known via timing signals fed to the DØ trigger system by the Accelerator. The Level 1 triggers that veto on Main Ring activity therefore reject events that occur within a window of $0.1 - 0.5$ sec of injection (called MRBS loss) and 800μsec of bunch passage through the detector (called microblanking) [56]. The effects on the calorimeter from MRBS loss are much greater than for microblanking, due to the greater beam dispersion at the time of injection into the Main Ring.

Most triggers veto on MRBS loss, but not all veto on microblanking. For example, since EM measurements are unaffected by Main Ring activity (scattering is limited to the CH layers and sometimes the outermost FH layer), the triggers that only require the presence of EM objects (electrons and photons) do not require the full Main Ring veto. On the other hand, some triggers

that require high $\not\!\!E_T$ do contain the full Main Ring veto, to preserve the $\not\!\!E_T$ measurement.

The EM1_EISTRKCC_MS trigger requires that both MRBS loss and microblanking not occur together during a beam crossing, and therefore many of the events can have Main Ring contamination as a result of the trigger veto. However, since an accurate $\not\!\!E_T$ measurement is necessary for W boson identification, a full Main Ring veto cut would appear to be necessary for all candidate events. That is, only events with no MRBS loss and no microblanking would be retained.

These cuts are insufficient, however, for two reasons: it is possible for Main Ring contamination to remain beyond the microblanking window due to long recovery times for the calorimeter preamps. The residual energy affects both the $\not\!\!E_T$ measurement and the energy flow measurement, which is expected to be quite sensitive to calorimeter fluctuations. Furthermore, a significant number of good events can be lost due to inefficiency in the full Main Ring veto. Both of these effects can be seen in Fig. 4.1, which shows the summed E_T for all towers near the Main Ring, defined as

$$E_T^{MR} = \sum_{\eta=-1.3,\phi=\pi/4}^{\eta=+1.3,\phi=3\pi/4} E_T^{tower} \tag{4.9}$$

Notice that a fraction of the events that pass the MRBS loss and microblanking cuts nonetheless contain large amounts of negative E_T^{MR}, indicating residual Main Ring contamination. Notice also that the distribution of events that fail the Main Ring veto shows a peak at $E_T^{MR} = 0.0$, which demonstrates the inefficiency of the cut. For the purpose of improving the efficiency without compromising the rejection, the Main Ring veto was discarded in favor of a

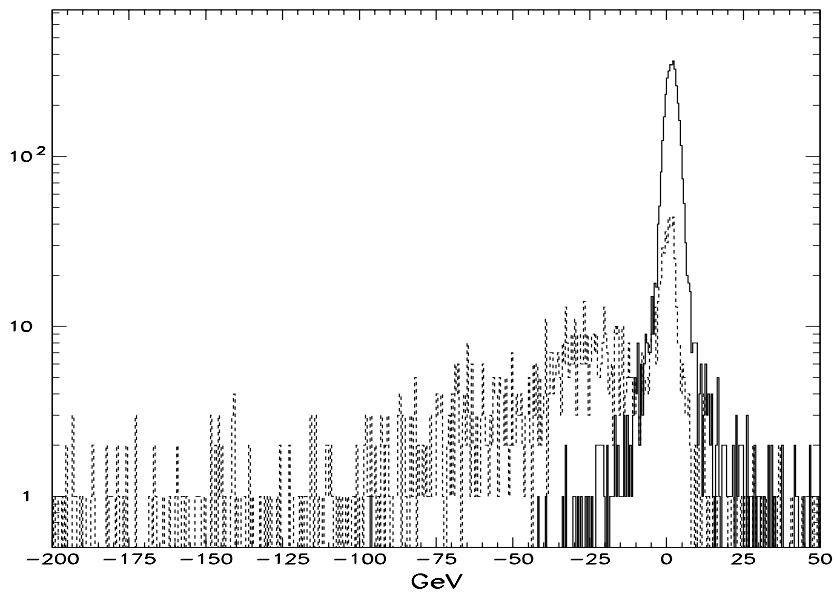

Figure 4.1. Summed E_T per event for towers near Main Ring, defined by $|\eta| < 1.3$ (the range of η spanned by the Main Ring) and $\frac{\pi}{4} < \phi < \frac{3\pi}{4}$. The solid pattern denotes events which pass the MRBS loss and microblanking cuts, while the dashed pattern denotes events which fail one or both cuts. The straight line indicates the E_T cut placed on all events in place of the Main Ring veto.

restriction on E_T^{MR}. As shown in Fig. 4.1, the restriction is $E_T^{MR} > -10$ GeV.

4.3.2 Jet Quality Cuts

Since jets are rather loosely defined objects, the cuts made on them are necessarily loose as well. The primary purpose of the jet quality cuts is to help ensure that events are free from fake jets reconstructed around hot cells in the calorimeter; only real energy clusters should remain.

The first cut is a restriction on the fraction of jet energy from the EM layers in the cluster. This is a basic hot cell cut which operates under the premise that if a hot cell (or localized group of hot cells) dominates the jet E_T, the EM fraction of that jet will be severely skewed toward the low or high end of the

EM scale, depending upon the location of the cell(s). The cut is defined as

$$0.05 < \frac{E_{jet}^{EM}}{E_{jet}^{TOTAL}} < 0.95 \tag{4.10}$$

For obvious reasons, this cut is not applied to jets which are also electron candidates.

The second cut is the hot cell fraction cut. It is designed to identify fake jet candidates whose E_T is dominated by a single, isolated hot cell (which is the most common type of hot cell), whereas real jets should have the majority of energy distributed over several cells. The cut is defined by the ratio of the most energetic cell in the cluster (E_{cell1}) to the second most energetic cell (E_{cell2}). The limit is

$$\frac{E_{cell1}}{E_{cell2}} < 10.0 \tag{4.11}$$

The last cut is an additional precaution against Main Ring contamination. An event that coincides with a Main Ring blast normally has many spurious jet candidates. Their removal is accomplished through the Coarse Hadronic fraction, which is the fraction of jet energy located in the CH layers. Since the CH layers are designed to measure the tail end of the jet shower, a typical real jet will only have a small fraction of its total energy measured there. The CH fraction cut is

$$\frac{E_{jet}^{CH}}{E_{jet}^{TOTAL}} < 0.4 \tag{4.12}$$

The above three cuts are applied to all jet candidates in the event. If any jet candidate fails any single cut, the entire event is dropped from the analysis. The combined efficiency of these cuts is ~96%[57].

4.3.3 *Electron Quality Cuts*

The requirements made on electron candidates are, in general, much more strict than those made on jets. This is due to the high precision with which EM showers can be measured, both in shape and in location, and to their highly localized nature of showers from true electrons.

There are two initial cuts for the electron. The first is a kinematic requirement on the electron candidate E_T. W bosons are massive objects ($M_W \simeq 80$ GeV), and so for $W^{\pm} \rightarrow e^{\pm}\nu$, the decay electron is expected to have high E_T. Thus, in order for an electron to be considered a decay object from a W boson, it must have E_T>25 GeV. The electron E_T distribution is shown below for the HLP electron candidates. It has a Jacobian shape with a peak at 40GeV, well above the trigger E_T threshold.

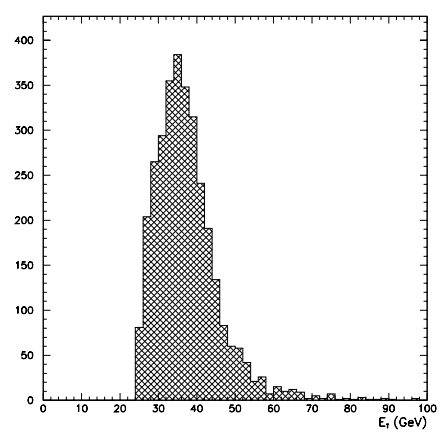

Figure 4.2. Electron E_T distribution for candidate W boson events from the HLP stream.

The second is a fiducial cut on the pseudorapidity (η_e) of the electron. All electron candidates whose reconstructed η_e coincides with the Intercryostat Region (ICR) are rejected due to poor EM coverage there. The partial EM

coverage in the regions defined by $1.1 <| \eta |< 1.5$ degrades the electron shower measurements such that no electron identification is possible within those limits. Further, all candidate events with forward electrons ($| \eta |> 2.5$) are rejected as well. For $| \eta |> 2.7$, the segmentation of the third calorimeter layer (EM3) is increased to 0.1×0.1 from 0.05×0.05 due to space constraints, thus hampering shower measurements there. Electron identification is further hampered by large energy depositions from spectator interactions near the beam line and corresponding loss in the trigger efficiencies in this region. The total kinematic and fiducial acceptance for electrons from $W^{\pm} \rightarrow e^{\pm}\nu$ events is $\sim$46%[60].

Next are a set of electron *quality cuts* that help decide whether an electron candidate sufficiently resembles a "true" electron as defined by Monte Carlo studies. The first of these is the EM fraction cut, described in Sec. 4.2.2. A more stringent cut of EM fraction >0.95 is invoked to suppress background from jets that fluctuate electromagnetically.

The second cut is a shower shape requirement. Test beam electrons were used to measure the development of electron-induced calorimeter showers. The shower shape was compared to Monte Carlo electron showers using a simulated detector. These were found to be in good agreement[58], so the Monte Carlo was used to generate sufficient statistics for shower shape measurements.

The shower shape is parameterized in 41 variables: the fraction of cluster energy contained in EM layers 1,2 and 4, the fractional energy in each layer 3 cell in a 6×6 array of cells centered on the highest energy tower in the cluster, the logarithm of the cluster energy, and z position of the event vertex[58]. The 41 variables are organized into a covariant matrix M. For a sample of N Monte

Carlo electrons, M is defined as

$$M_{ij} = \frac{1}{N}\sum_{n=1}^{N}(x_i^n - \langle x_i \rangle)(x_j^n - \langle x_j \rangle) \tag{4.13}$$

where $x_{i(j)}^n$ is the i'th(j'th) shower parameter for the n'th electron and $\langle x_{i(j)} \rangle$ is the mean value of i'th(j'th) parameter for the sample. For each electron candidate in the HLP data, the 41 parameters are calculated and an electron likelihood variable is constructed, similar to a χ^2 variable, which reflects the degree of agreement between the data candidate and the Monte Carlo sample for each parameter. The likelihood variable, χ_H^2, is determined by

$$\chi_H^2 = \sum_{i,j}(y_i - \langle x_i \rangle)H_{ij}(y_j - \langle x_j \rangle) \tag{4.14}$$

where $y_{i,j}$ is the i'th(j'th) shower parameter for the electron candidate and $H = M^{-1}$. A cut is placed on the candidate shower shape by imposing an upper limit on χ_H^2, also called an *H-matrix* χ^2. For this analysis, the requirement is $\chi_H^2 < 100$.

An important distinction between jets and electrons is that, while jets are composite objects comprised of many particles, electrons are single particles and should therefore induce extremely localized calorimeter showers relative to jets. This distinction led to the development of the cluster *isolation* cut, which requires that the electron cluster be relatively isolated from other large energy depositions in the calorimeter. If a cone of radius $R = 0.4$ is constructed around the electron cluster centroid and the tower energy summed within that cone, 90% of the EM energy in that sum must reside within an inner cone of radius $R = 0.2$. Events in which the electron candidate is not isolated to this

degree are dropped. The application of this cut in the software is

$$f_{\rm iso} = \frac{E^{total}_{(R<0.4)} - E^{EM}_{(R<0.2)}}{E^{EM}_{(R<0.2)}} < 0.1 \tag{4.15}$$

Another important feature of true electrons is the necessary presence of a track pointing to the calorimeter cluster from the event vertex. The degree to which the track vector matches the location of the shower centroid is a means of discriminating electrons from photons. While photons, produced either directly or through π^o meson or η meson decay, do not leave tracks in the central detector, there may nonetheless appear to be an associated track if some other charged particle is emitted nearby. This source of background can be greatly suppressed by requiring a good match between the track and the cluster centroid. For electron candidates in the Central Calorimeter, this match is quantified by the expression[59].

$$\sigma^{CC}_{trk} = \sqrt{(\frac{\Delta\phi}{\delta\phi})^2 + (\frac{\Delta z}{\delta z})^2} \tag{4.16}$$

where

$$\begin{aligned} \Delta\phi &= \phi_{track} - \phi_{clus} \\ \Delta z &= z_{track} - z_{clus} \end{aligned} \tag{4.17}$$

and $\delta\phi$ and δz are the errors in these quantities. For electron candidates in the Endcap Calorimeter, the expression changes to

$$\sigma^{EC}_{trk} = \sqrt{(\frac{\Delta\phi}{\delta\phi})^2 + (\frac{\Delta R}{\delta R})^2} \tag{4.18}$$

where

$$\begin{aligned} \Delta R &= \sqrt{(\Delta x)^2 + (\Delta y)^2} \\ \Delta x &= x_{track} - x_{clus} \\ \Delta y &= y_{track} - y_{clus} \end{aligned} \tag{4.19}$$

The requirement on both track matches is the same, however, with the upper limit set as $\sigma_{trk}^{EC,CC} < 10.0$.

The last electron quality cut is a method of suppressing fake electrons caused by localized clusters of hot cells in the EM layers of the calorimeter. Hot cells are typically isolated individually – in some instances small groups of 2 or 3 hot cells are found. Larger clusters of hot cells can occur in rare cases where a certain part of the detector, such as a BLS crate, goes bad during a run. In such cases, the entire run is typically thrown away and is not put into any of the streams. To help guard against the single or small groups of EM hot cells being mistaken for a real electron, a cut is placed on the number of cells contributing to the candidate cluster. This last cut is $N_{cells} > 20$.

For each candidate event, there must be one and only one electron that passes all of these cuts (primarily to reject $Z \rightarrow e^+e^-$ events). The combined electron ID efficiency for this set of cuts is 91.3% for electrons in the CC and 83.2% for electrons in the EC[58].

4.3.4 $\not\!\!E_T$ Cut

Since there are no measurable quantities for neutrino's, except for $\not\!\!E_T$ (and $\phi_{\not\!\!E_T}$), there are no quality cuts available of the sort used on electron candidates. However, a kinematic cut can be applied under the same rationale as was used for the electron. The requirement for the neutrino is $\not\!\!E_T$ >25 GeV. The $\not\!\!E_T$ distribution for the candidate events is shown in Fig. 4.3.

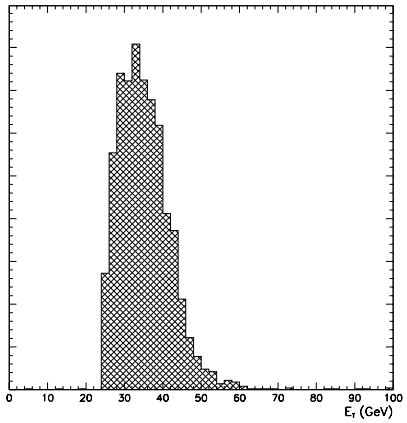

Figure 4.3. Missing E_T distribution for candidate W boson events from the HLP stream.

4.3.5 W Reconstruction

If an event passes all of the above cuts, a W boson reconstruction is attempted from the electron and neutrino. The reconstruction calculations are described in Appendix A. The strategy is to determine the z component of the neutrino momentum (p_z^ν) from a W boson mass formula assuming a constant W mass (M_W) of 80.22 GeV/c^2. It is possible that the resulting quadratic expression for p_z^ν yields imaginary solutions. In this case, M_W is increased by 5 GeV/c^2 and the quadratic form evaluated again. If the solutions are still imaginary, the process is iterated until real solutions are found, subject to the constraint $M_W < 100$ GeV/c^2. If this limit is violated before real solutions can be found, the event is assumed not to represent a real W boson and is discarded.

The last cut for defining the $W + jets$ event sample is on the W boson transverse mass (M_T^W). Events in which M_T^W is either too low or too high are assumed to be background from QCD or $W \rightarrow \tau\nu \rightarrow e\nu\nu$ production. The constraint is 45 GeV/c^2 $< M_T^W <$ 105 GeV/c^2. The M_T^W distribution for all

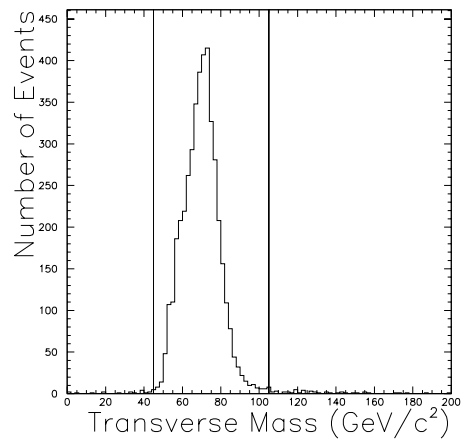

Figure 4.4. W boson transverse mass distribution for all events in which a W could be reconstructed. The lines at 45 GeV/c^2 and 105 GeV/c^2 represent the M_T^W restrictions on the data.

remaining candidate events prior to this cut is shown in Fig. 4.4.

4.4 Analysis Requirements

Events which pass all of the above cuts are considered as real W+jets events. This sample forms the candidate sample for the color coherence analysis. Additional cuts are imposed, however, to clean up the final event sample.

4.4.1 Multiple Interactions

During a $\overline{p}p$ bunch crossing, there is no guarantee that only one proton will collide inelastically with only one antiproton. The average number of interactions per crossing varies with the instantaneous luminosity of the beam as[52]

$$\overline{n} = \sigma \mathcal{L} t \tag{4.20}$$

where $\overline{n}$ is the average number of interactions, σ is the cross section for inelastic collision as measured by the Level 0 counters[2]), $\mathcal{L}$ is the instantaneous luminosity (interactions per unit area per second), and t is the bunch crossing time ($t = 3.5\mu$s[44]). At $\mathcal{L} = 5 \times 10^{30}$ cm^{-2}s^{-1}, the average number of interactions is $\overline{n} = 0.75$. By contrast, at $\mathcal{L} = 10 \times 10^{30}$ cm^{-2}s^{-1}, $\overline{n} = 1.5$. During Run 1B, $\mathcal{L}$ varied from 1×10^{30} cm^{-2}s^{-1} to 20×10^{30} cm^{-2}s^{-1}, so a high proportion of events contain two or more interactions, called *multiple interaction events.*

Multiple interactions are detrimental to the color coherence analysis. Although additional interactions are most likely to be soft, there can be additional low-E_T jet production in the event resulting from secondary collisions. The presence of these jets contaminates the energy flow measurement of the W+jets process and complicates recognition of the color coherence pattern. For multiple interaction events with no associated secondary jet production, there is still contamination in the event energy flow. Although the particle distribution for soft secondary interactions is expected to be uniform on average, event-by-event fluctuations in that distribution, combined with the significant increase in the global energy level in the calorimeter, sufficiently compromises the ability to identify the desired energy flow patters as to make multiple interaction events unsuitable for the analysis.

Unfortunately, there is no method for unambiguously identifying multiple interaction events. Secondary interactions deposit additional energy in the calorimeter, and the the maximum center-of-mass energy is 1800GeV per interaction, which would mean that secondary interactions can be identified in any event where the total energy in the calorimeter is greater than 1800 GeV. However, the actual center-of-mass energy is typically far less than the maxi-

[2] $\sigma = 46.7$mb[61]

mum, so this strategy is not useful for most events.

A probability method of flagging multiple interaction events has been developed at DØ that designates a relative probability for secondary interactions in an event based on analysis of specific event quantities[62]. These quantities are:

- total energy in the calorimeter
- number of interaction vertices reconstructed by the central tracker
- number of tracks used by tracker in vertex reconstruction
- displacement of Level 0 vertex from central tracker vertex (if only one vertex found by tracker)

This utility, called the Multiple Interaction Tool, returns an integer from 0 to 4 (called the MI Flag). Values from 1 to 4 represent increasing relative probability that an event contained more than one interaction. A value of MI Flag = 1 indicates the event was most likely the result of a single interaction, while a value of MI Flag = 4 indicates an event most likely contained multiple interactions. The result MI Flag = 0 indicates that not enough information was available to make a determination. This can happen if, for example, the tracker temporarily malfunctioned so that no vertex information was available or if there were too few hits in the Level 0 counters for it to measure a vertex.

To maximize the probability for single interaction in the $W + jets$ events used in the analysis, only events with MI Flag = 1 are retained. The distribution of MI Flag values is shown in Fig. 4.5a, as well as the average MI Flag value as a function of $\mathcal{L}$ for the candidate events in Fig. 4.5b.

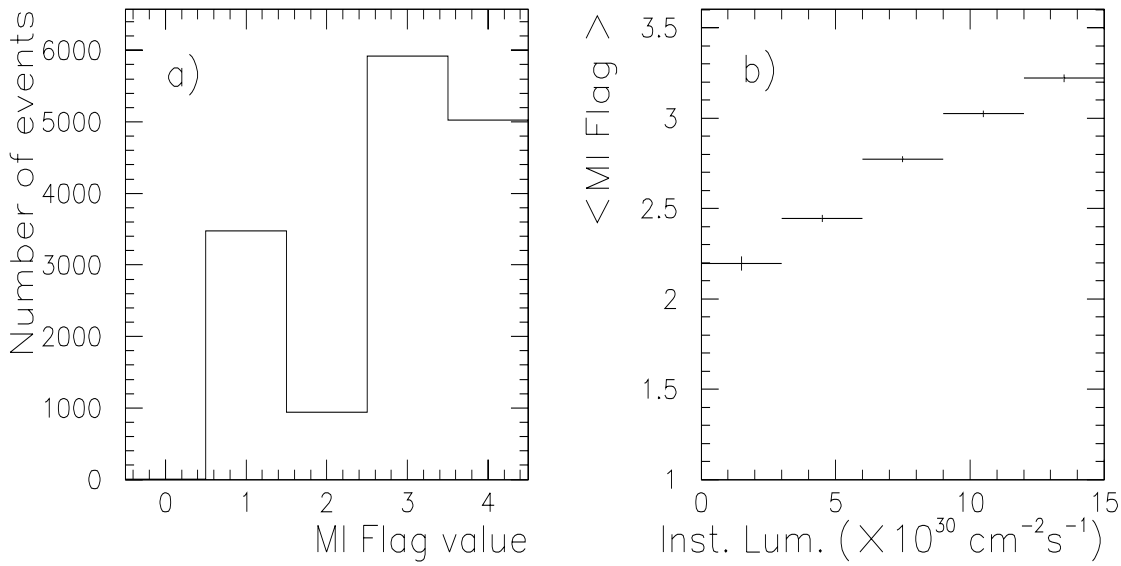

Figure 4.5. a) Distribution of MI Flag values for surviving event candidates. b) Average MI Flag value as a function of $\mathcal{L}$.

4.4.2 W Boson Transverse Momentum

A minimum p_T cut is imposed on the reconstructed W boson in all surviving events. The constraint is p_T^W >10GeV/c, which is away from the jet reconstruction threshold. The distribution of p_T^W in the data is shown in Fig. 4.6.

4.4.3 Vertex Position

When a particle impinges on the calorimeter, the induced shower develops in approximately the same direction as the particle. The projective shape of the calorimeter towers was designed so that particles emanating from an interaction vertex near $z = 0.0$ cm (the center of the detector) induce showers along the tower directions. For such vertices, physics $\eta \sim$ detector η. However, for

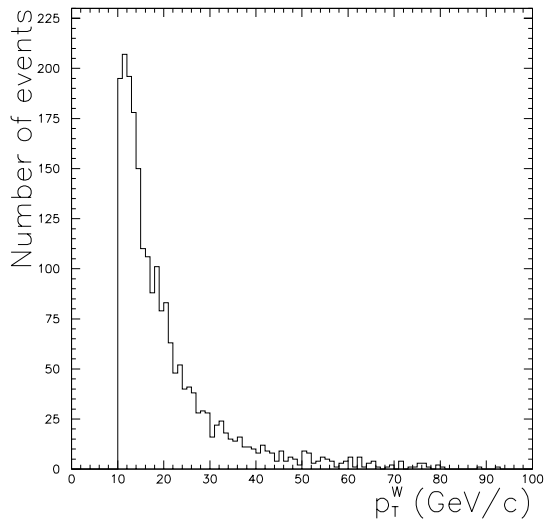

Figure 4.6. Distribution of p_T^W in $W + jets$ events, after the 10 GeV/c cut.

vertices displaced along the z direction (i.e. $\mid z \mid > 0$ cm), there is a mismatch incurred between the physics η and detector η values (particularly for central values of detector η) and a corresponding loss in the projective nature of the calorimeter towers with respect to shower directions. Therefore, a restriction is placed on allowed vertex displacements in the z direction. Events are kept only if $\mid z_{vertex} \mid < 20$ cm, where z_{vertex} is the z component of the interaction vertex. The choice of 20 cm was made to balance the need to preserve the projective nature of the towers with the need to avoid too much loss in statistics. A correction for the towers based on the physics η/detector η mismatch is described in the next chapter. The difference between physics η and detector η is shown in Fig. 4.7.

4.4.4 W-Jet Azimuthal Correlation

Since the energy flow pattern around the most energetic jet in the event is to be compared with the energy flow pattern around the W boson in the color

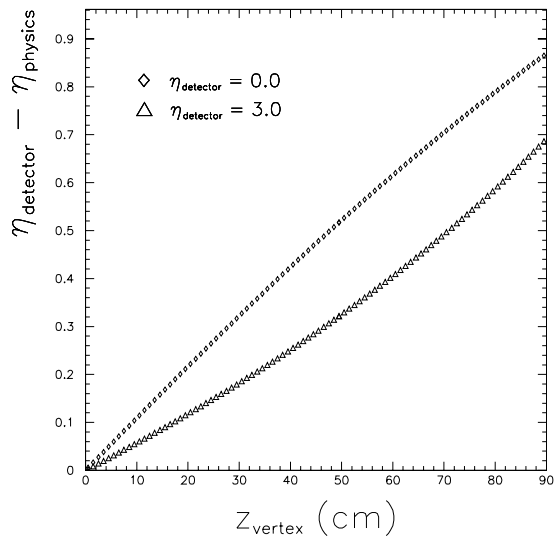

Figure 4.7. Mismatch between physics η and detector η as a function of z component of the event vertex for $\mid z_{vertex} \mid < 90$ cm. Differences are plotted for $\eta_{det} = 0.0$ and $\eta_{det} = 3.0$ for comparison.

coherence analysis, it is necessary to maximize the distance in ϕ between the tagged jet and W, thereby reducing the overlap between the two regions of interest. Ideally, this would entail a tight back-to-back cut in ϕ between the tagged jet and the W boson. However, making such a stringent requirement would severely restrict the radiation from the jet in the ϕ direction, biasing the energy flow measurement. Therefore, a very loose back-to-back cut is placed on the events that does not bias the energy flow. The requirement is $\frac{\pi}{2} < \mid \phi_W - \phi_{jet} \mid < \frac{3\pi}{2}$. The ϕ separation between the W and the tagged jet is shown in Fig. 4.8.

4.4.5 Rapidity Restriction

Restrictions are imposed on the rapidity of the W boson and the tagged jet to keep them confined to the central region of the detector. This is because the energy flow measurement (described in Chapter 6) extends to 1.5 units in η be-

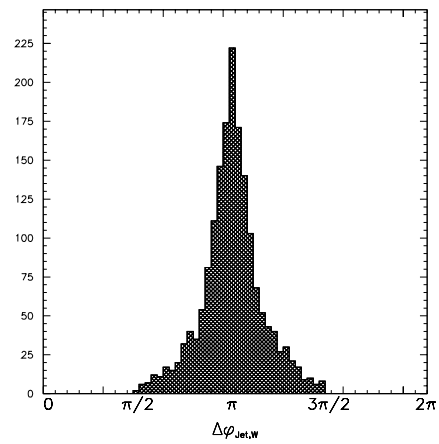

Figure 4.8. Azimuthal separation of W boson and tagged jet in W+jets events. Note the strong peak at π, which is represents the kinematically most probable configuration, even in the absence of a tight back-to-back restriction.

yond each object. It is desirable to keep this region away from the far forward regions of the detector, where cell sizes change several times (thus changing tower definitions) and where particle showering in the calorimeter spills over into surrounding cells frequently. It is also the region in which spectator interactions contribute most to tower energy measurements. Therefore, each event is required to have a central W boson and tagged jet, defined by $\mid y_W \mid < 0.5$ and $\mid \eta_{jet} \mid < 0.5$.

4.5 Summary

A summary of the cuts used in this analysis is presented in Table 4.1 below. The surviving events form the core analysis sample. There are ~250 events remaining in this data set.

Table 4.1. Summary of cuts used in acquiring W+jets events for the analysis

W **Parameters**	**Cut Value**
Electron χ^2	<100
Electron σ_{trk}	<10
Electron EM Fraction	>0.95
Electron σ_{trk}	<10
Electron $f_{\rm iso}$	<0.1
Electron $N_{\rm cells}$	>20
Electron E_T	>25GeV
Electron $\mid \eta \mid$	<1.1 or between 1.5 and 2.5
$\not{E}_T$	>25GeV
M_T^W	>45GeV and <110GeV
p_T^W	>10GeV/c
$\mid y_W \mid$	<0.7
Jet Parameters	
$N_{\rm jets}$	≥ 1
Jet EM Fraction	<0.95 and >0.05
Jet CH Fraction	<0.4
Jet Hot Cell Fraction	<10
$\mid \eta_{\rm jet} \mid$	<0.7 (tagged jet)
Event Parameters	
$\Delta\phi_{W,Jet}$	$> \pi/2$ and $< 3\pi/2$
MI Flag	$=1$
Main Ring E_T	> -10GeV
Event Luminosity $\mathcal{L}$	$< 8 \times 10^{30}$ cm^{-2}s^{-1}
$\mid z_{\rm vertex} \mid$	<20cm

CHAPTER 5

CORRECTIONS TO THE DATA

Since the color coherence pattern sought in this analysis results from soft radiation (producing low energy particles), it is expected to be sensitive to low energy detector-induced effects such as electronic noise. These effects were studied to determine their contributions to measured energies and to develop a set of corrections to compensate for such contributions. This is necessary in order to remove spurious contributions to the tower energies which could compromise the color coherence measurement. The detector effects can be divided into two categories, *pedestal offsets* and *zero suppression* effects. These are discussed separately. There is an additional, unrelated correction to be made to help remedy the mismatch between physics η and detector η for events with offset vertices, which is detailed following the detector corrections.

5.1 Pedestal Offsets

There are three sources of energy measured in a calorimeter cell: energy from a particle traversing the calorimeter, energy from nuclear β decay in the uranium absorber plates, and electronic noise from the cell itself. Approximately every other day during collider operation, the energy of each cell is measured for a short time with no beam in the Tevatron, thus isolating the uranium/electronic noise contribution. For each cell, the mean of the distribution (called the

pedestal) and standard deviation (called the pedestal width, or σ_{ped}), are calculated. The pedestal mean and width are stored in a database for use during physics runs.

For every event during a physics run, the measured energy (in ADC counts) of each cell is reduced by its pedestal value at the hardware level (prior to processing by the trigger framework). This is pedestal subtraction. Its purpose is to "zero" the calorimeter so as to eliminate uranium/electronic noise contributions.

If the reduced cell energy is within $\pm 2\sigma_{ped}$ of zero, the cell is assumed to have an energy of zero and it is suppressed (not read to tape). This reduces the number of cells to be read out by about a factor of 10, greatly reducing the time required for recording interesting events. The effects of this zero suppression are discussed in the next section.

Calibration runs used to measure the pedestals are performed during *quiet time* - meaning no beam in the Tevatron or in the Main Ring. During physics runs, therefore, pedestal offsets are possible due to beam effects, such as *pileup energy*.

5.1.1 Pileup Energy

Pileup in the calorimeter is the result of capacitance in the Baseline Subtraction (BLS) sampling circuit. Signals from the calorimeter cells are sampled just prior to a beam crossing (to measure the baseline level) and again 2.2μs after. The voltage difference is proportional to the charge collected by the capacitive circuit. The circuit then requires some finite time ($\sim$few μs) to discharge the capacitors (baseline restoration). The baseline restoration time, by design, is much longer than the 3.5μs beam crossing time. This results in an approxi-

mately flat baseline for subsequent beam crossings. During any beam crossing, however, the BLS does exhibit some capacitive discharge, lowering the baseline by some amount during the charge collection. Therefore, for each cell that is hit during a beam crossing whose BLS is still in the process of discharging, the total charge collected by the BLS will be reduced by the falling baseline due to the slow discharge in the capacitive circuit from previous crossings. The net result is a reduction in the measured energy for those cells that is not accounted for in the pedestal subtraction.

5.1.2 Luminosity Dependence

The probability for n interactions during a beam crossing can be approximated by the Poisson probability function[52]

$$f_{\overline{n}}(n) = \frac{\overline{n}^n e^{-\overline{n}}}{n!} \tag{5.1}$$

where $\overline{n}$ is the average number of interactions per crossing at the instantaneous luminosity ($\mathcal{L}$) of that crossing (described in Sec. 4.4.1). The probability for *at least one* interaction during a crossing, therefore, is

$$f_{\overline{n}}(> 0) = 1 - f_{\overline{n}}(0) = 1 - e^{-\overline{n}} \tag{5.2}$$

with the luminosity dependence embedded in the definition for $\overline{n}$. At $\mathcal{L} = 5 \times 10^{30}\mathrm{cm}^{-2}\mathrm{s}^{-1}$, for example, $f_{\overline{n}}(> 0) = 0.53$. Thus, for any random crossing at this luminosity, there is a 53% probability that the previous crossing contained an interaction. This is also, then, the percentage of events at this

luminosity that will contain some pileup contamination. For contrast, at $\mathcal{L} = 10 \times 10^{30}\text{cm}^{-2}\text{s}^{-1}$, $f_{\overline{n}}(> 0) = 0.78$, indicating that the pileup contribution in the data increases with luminosity.

5.1.3 Pileup Correction

Since pedestal offsets directly influence energy measurements, several sets of corrections were developed to reduce their effect on the W+jets data. This entailed measuring the average pedestal offset for each cell at various luminosities and storing the averages, cell by cell, for use as correction factors.

The measurements were performed using Run 1B non-zero suppressed *zero bias data.* The term zero bias indicates events that were recorded at specified time intervals during a data-taking run with no specific trigger requirements, and thus no trigger biases.

Zero bias data are needed to avoid triggered high-E_T objects in the calorimeter which would overwhelm the pedestal offsets to be observed. The lack of zero suppression, while increasing event size and processing time, allows for determination of offsets for all cells for every event (thus reducing the number of events needed to obtain good statistics) and avoids any biases towards higher energy cells due to suppression of lower energy cells. Calibration pedestals are subtracted in the hardware at runtime.

Zero bias data, although void of any triggered events, may nonetheless contain a substantial fraction of events with inelastic collisions, particularly at higher luminosities. These events are vetoed using the following offline requirements:

- No reconstructed jets

- No hits in the Level 0 scintillation counters
- No Central Detector tracks

These cuts help ensure that the calorimeter was "empty" for these events, thus isolating the pedestal offsets from any real energy resulting from collisions.

Five sets of zero bias data were used to measure the pileup contributions, each corresponding to a specific luminosity. The average luminosities of the samples are $3\times10^{30}\mathrm{cm}^{-2}\mathrm{s}^{-1}$, $5\times10^{30}\mathrm{cm}^{-2}\mathrm{s}^{-1}$, $7\times10^{30}\mathrm{cm}^{-2}\mathrm{s}^{-1}$, $10\times10^{30}\mathrm{cm}^{-2}\mathrm{s}^{-1}$, and $14\times10^{30}\mathrm{cm}^{-2}\mathrm{s}^{-1}$. For each event in a sample, a restriction was imposed such that $|\mathcal{L}_{event} - \langle\mathcal{L}_{sample}\rangle| < 0.3$ to minimize luminosity-dependent pedestal shifts within each sample.

Fig. 5.1 shows the distribution of cell energies in the calorimeter for three of the data sets, corresponding to $\mathcal{L} = 3\times10^{30}\mathrm{cm}^{-2}\mathrm{s}^{-1}$, $5\times10^{30}\mathrm{cm}^{-2}\mathrm{s}^{-1}$, and $10\times10^{30}\mathrm{cm}^{-2}\mathrm{s}^{-1}$. The energy per cell, averaged over all ϕ for several hundred events, is plotted as a function of η.

Note that, for any value of η, the cell energy drops with increasing luminosity. This reflects the fact that the probability for inelastic $\overline{p}p$ scattering during a beam crossing increases with $\mathcal{L}$.

For all luminosities, the energy distribution falls sharply with increasing $|\eta|$. Low-E_T scattering dominates the $\overline{p}p$ beam crossings, resulting in large numbers of soft particles which populate the forward regions of the detector. Therefore, cells in the forward regions are more likely to be hit in consecutive crossings than more central cells, resulting in greater pileup at higher $|\eta|$ regions.

For the W+jets events, all calorimeter cells are corrected for the pedestal offsets, so that

$$E_{corr} = E_{uncorr} - \langle E_{ped}\rangle \tag{5.3}$$

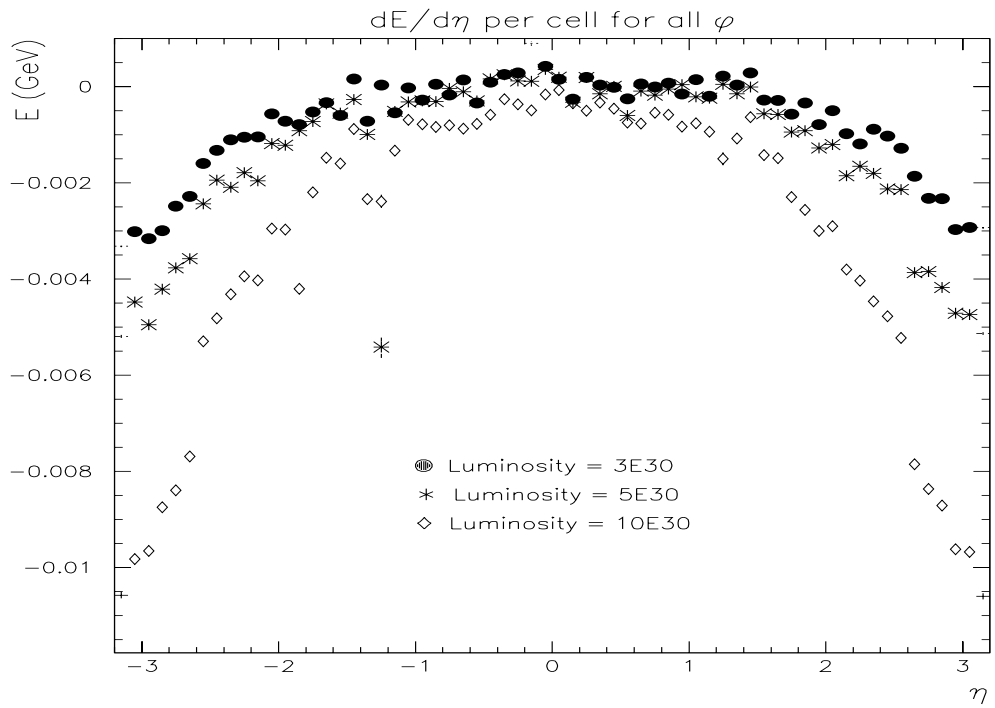

Figure 5.1. Pedestal offset energy, per cell, as a function of η for three luminosities (averaged over all ϕ).

where E_{uncorr} is the measured energy for a particular cell, $\langle E_{ped} \rangle$ is the mean pedestal offset for that cell, and E_{corr} is the cells' corrected energy after subtraction of the offset. By matching the luminosity of the W+jets event to the nearest luminosity at which pedestal offsets were measured and using those offsets for that event, $\mathcal{L}$-dependent effects from pileup were corrected.

5.2 Zero Suppression

Cells with energies within $\pm 2\sigma_{ped}$ of zero were not read out (i.e. zero suppressed). Due to uranium noise in the cells, the pedestal distribution is not Gaussian, but has a positive tail. This positive tail means that the average energy (following the hardware pedestal subtraction) within $\pm 2\sigma_{ped}$ is slightly negative, and so the effect of zero suppression is to artificially add small pos-

itive amounts of energy to the calorimeter at readout time. This additional contribution can be significant at the tower level, where measured energies can be quite low, and hence must be corrected for in this analysis.

5.2.1 Zero Suppression Correction

This correction is determined using calorimeter cell information from zero bias events recorded during a global (physics) run. The goal is to estimate the average energy per cell for cells that are zero suppressed in the zero bias data and add that energy to zero suppressed cells in the W+jets events. Since this average energy is negative, the effect on the W+jets data will be to lower the overall energy distribution, thus helping to isolate the low-lying energy flow pattern due to color coherence.

For a sample of zero suppressed zero bias events at the same luminosity (with no interaction during the beam crossing), the energy of each cell can be expressed as

$$N_{\langle}E_{<}\rangle + N_{>}\langle E_{>}\rangle = N_t(E_p) \equiv E^{\mathcal{L}}_{zsp} \tag{5.4}$$

where $N_{<(>)}$ is the number of times the cell was suppressed (unsuppressed), $\langle E_{<(>)}\rangle$ is the mean energy of the cell when it was suppressed (unsuppressed), N_t is the total number of events in the sample, and E_p is the mean pedestal offset energy (pileup) of the cell at the luminosity of the sample (discussed in the previous section).

The quantity $\langle E_{<}\rangle$ is the correction factor required to offset the additional uranium noise energy due to zero suppression. In parallel with the pileup calculation, a correction is constructed for each cell and for various luminosities. The luminosities of the data used to calculate the zero suppression correction

must match those used in the pileup correction so that the equality in Eq. 5.4 remains true.

Sufficient zero suppressed zero bias data exist for only three of the luminosities used in the pileup calculation: $\mathcal{L} = 3\times10^{30}\mathrm{cm}^{-2}\mathrm{s}^{-1}$, $\mathcal{L} = 7\times10^{30}\mathrm{cm}^{-2}\mathrm{s}^{-1}$, and $\mathcal{L} = 10\times10^{30}\mathrm{cm}^{-2}\mathrm{s}^{-1}$. For each of the three sets of data, $\langle E_< \rangle$ is determined on a cell-by-cell basis through the expression

$$< \langle E_< \rangle = \frac{N_t(E_p) - N_> \langle E_> \rangle}{N_<} \tag{5.5}$$

and then stored in a data file.

5.3 Combined Results

The pedestal corrections were applied to zero suppressed data to minimize the effects of pileup and uranium noise on a cell–by–cell basis as follows:

$$\begin{aligned} &\text{Cell suppressed:} && E_{corr} = E_{uncorr}(=0) - E^{\mathcal{L}}_{ped} + E^{\mathcal{L}}_{zsp} \\ &\text{Cell not suppressed:} && E_{corr} = E_{uncorr} - E^{\mathcal{L}}_{ped} \end{aligned} \tag{5.6}$$

where E_{uncorr} is the uncorrected cell energy, $E^{\mathcal{L}}_{ped}$ and $E^{\mathcal{L}}_{zsp}$ are the pedestal offset (pileup) and uranium noise cell corrections at the luminosity closest to the luminosity of the event, and E_{corr} is the corrected cell energy.

To test the effectiveness of the corrections, they were applied to an independent sample of zero suppressed zero bias data with $\mathcal{L} = 3 \times 10^{30}\mathrm{cm}^{-2}\mathrm{s}^{-1}$. Fig. 5.2 shows the average cell energy as a function of detector η before and after the corrections. There is clear improvement in the η dependence of the energies, as demonstrated by both the shape and level of the distribution.

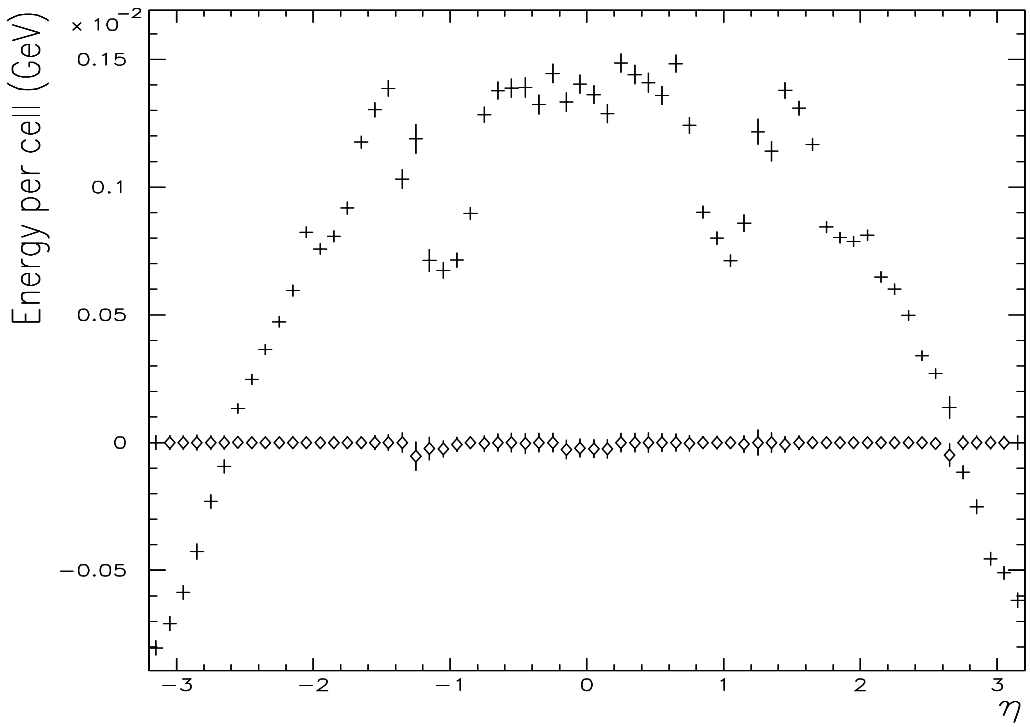

Figure 5.2. A sample of zero suppressed zero bias data, demonstrating the effect of the pedestal corrections. The crosses represent the uncorrected data, while the diamonds represent the same data after application of both corrections described in the text.

5.4 Offset Vertex Correction

In the previous chapter, the change in physics η with respect to detector η due to vertex displacement was described. A restriction on the displacement was imposed to minimize this mismatch. However, since the projection for each calorimeter tower is defined relative to the center of the detector and not the event vertex, this projective nature is still compromised whenever the vertex is offset from the detector center. For large objects such as jets this is generally not a serious problem, since the jet cone is large enough to encompass most particles that cross towers in the calorimeter. This analysis, however, relies on the measurements of individual tower locations and energies, making an

accurate tower definition essential. The standard detector-oriented definition of the towers is therefore discarded in favor of one that accounts for the vertex offset on a cell-by-cell basis.

The Cartesian coordinates are known for each cell in the calorimeter. For each event, the positions for all of the cells are redefined relative to the event vertex by the formula

$$x_i^{phys} = x_i^{det} - x_i^{vtx} \tag{5.7}$$

where x_i^{phys} are the Cartesian positions corrected for the vertex offset x_i^{vtx}, and x_i^{det} are the original Cartesian positions defined by the detector. These new positions are then transformed into the standard physics coordinates η and ϕ by

$$\begin{aligned} \eta_{phys} &= -\ln[\tan(\theta_{phys}/2)] \\ \phi_{phys} &= \arctan \tfrac{x_2^{phys}}{x_1^{phys}} \end{aligned} \tag{5.8}$$

where

$$\begin{aligned} R_{phys} &= \sqrt{(x_1^{phys})^2 + (x_2^{phys})^2 + (x_3^{phys})^2} \\ \theta_{phys} &= \arcsin \tfrac{R_{phys}}{x_3^{phys}} \end{aligned} \tag{5.9}$$

The new physics coordinates are then truncated into integer variables and the new towers are defined the same as the detector towers were, i.e. all cells with the same integer values for η_{phys} and ϕ_{phys} are summed to form physics towers. This new projection is thus correct for each tower relative to the event vertex. The vertex-corrected towers are then used in the subsequent investigation of soft particle distributions in the W+jet analysis sample.

CHAPTER 6

ANALYSIS OF THE DATA

6.1 Overview

As discussed in Chapters 1 and 2, color interference effects among partons in hadron-hadron interactions result in a non-isotropic distribution of soft particles in the event. Specifically, soft particle production is expected to be suppressed in regions transverse to the plane of the event. For interactions in which the final state contains a W boson and opposing parton, there is the further expectation that particle production should be minimal in the vicinity of the boson due to the lack of color flow activity there. These two notions drive the analysis strategy for the W+jets sample. The study of color interference effects in the data centers on a measurement of the distribution of soft particles that is sensitive to differences in multiplicity between the jet and W boson regions and between the event and transverse planes.

6.2 Construction of the Variables

6.2.1 Particles in the Calorimeter

The most straightforward method of observing particle distributions is to count reconstructed tracks across the various tracking chambers. Unfortunately, the DØ tracking system is ill-suited for such a measurement. Specifically, the VTX

and FDC chambers proved to be unusable for this analysis. Studies of track reconstruction in the VTX have shown that, due to the high hit multiplicity in the wires, most tracks are the result of simple combinatorics in the reconstruction algorithm, rather than the passage of actual particles[64]. Additional studies have shown that, for electrons with an associated CDC track, there is a corresponding track in the VTX only $\sim$15% of the time[64], hence the efficiency is extremely low. The FDC may not be used because of multiple scattering. There are support structures in place directly in front of the FDC chambers. Particles passing through the supports can undergo multiple scattering interactions and bremsstrahlung in the support material can induce several tracks in the FDC chambers from the emitted secondary particles. While many of these tracks may be eliminated through impact parameter cuts[1], enough survive these cuts as to render track distribution measurements in the FDC unreliable. That leaves only the CDC, which has a fiducial area that is too small to merit its consideration in this analysis.

For these reasons, the tracking detectors are discarded in favor of the calorimeter, which is the heart of the DØ detector. The calorimeter is segmented in very small units (each tower covers $\Delta\eta\times\Delta\phi = 0.1\times0.1$), providing a reasonable tool for measuring the directions of soft particles passing through the cells. The calorimeter is extremely hermetic, unlike the tracking chambers, and provides large fiducial coverage. A further advantage over the tracking chambers is that both charged and neutral particles may be measured with the calorimeter. This analysis therefore measures the pattern of the ensemble of particles in an event by measuring the pattern of energy those particles

[1]The impact parameter is defined as the distance of closest approach of a track to the interaction vertex. FDC tracks induced by secondary particles frequently have large impact parameters, indicating that they did not come from the interaction vertex.

deposit in the calorimeter cells. The assumption is that this energy distribution is representative of the distribution of primary particles in an event. This assumption may be challenged by noting that pedestal fluctuations (e.g. from residual uranium noise or electronic noise) can contribute low levels of energy throughout the calorimeter on an event-by-event basis. In any particular event, therefore, the energy distribution can be strongly influenced by these contributions.

This complication can be minimized, however, by selecting towers with energies significantly higher than the noise contributions. In this analysis, only towers with $E_T >$ 250 MeV are used in the measurements. The variable E_T was chosen for boost invariance. The 250 MeV threshold was chosen to reduce the contribution due to pedestal fluctuations. After the pedestal offsets were corrected in the zero bias sample, the tower energies were measured to determine the variation in residual energy. The tower distributions have widths

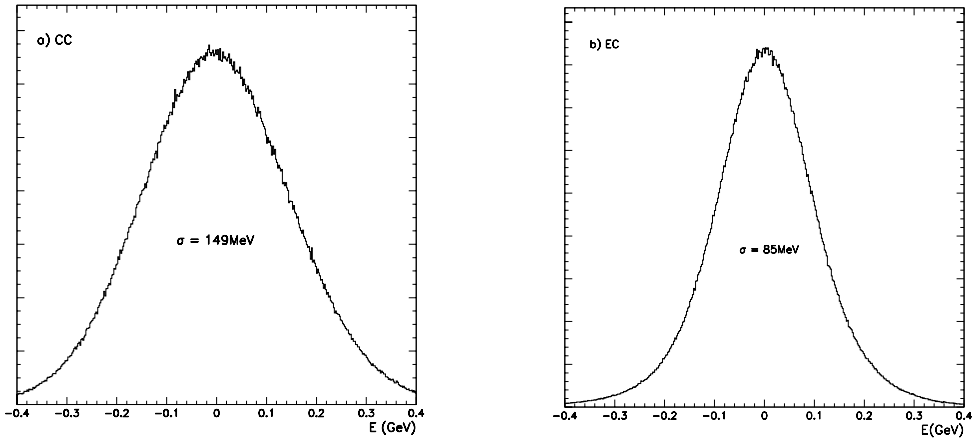

Figure 6.1. Residual tower energy from zero bias data for all towers in a)the Central Calorimeter and b)the Endcap Calorimeters.

$\sigma \simeq$150 MeV and 85 MeV (in energy) in the CC and EC, respectively. With an E_T threshold, the residual noise contributes most in the central region,

decreasing in the forward regions. This is due to the increasing energy required for a tower to pass the E_T threshold as η increases. A higher E_T threshold would reduce the noise contributions even further, but the number of towers surviving higher thresholds is small enough to compromise the measurements. A discussion of the effect of the E_T threshold on the measurements is reserved until later in the chapter.

The method of analysis is to measure the distribution of towers around the W boson and the opposing jet and compare them. For each event, these distributions are constructed in two regions of equal area in (η,ϕ) space – one centered on the W boson location and one centered on the tagged (opposing) jet location. The tagged jet is selected by choosing the leading–E_T jet in the event. The comparison of these distributions acts as a probe of color coherence effects in the data. Color coherence in $W + jets$ events is expected to result in a depletion of particle production at large angles relative to the event plane, i.e. the transverse plane. The indication of this effect in the data should be a similar pattern of energetic towers in the jet region *as compared to the W boson region.*

6.2.2 Annular Regions

The relevant variables used in the measurement are shown in Fig. 6.2, which depicts a $W + 1jet$ event in the center-of-mass frame. The proton and antiproton beams are shown to indicate the directions of the initial-state colliding partons. The final state parton which fragments into the tagged jet retains a color connection to the beam fragments. The color flow in such an event is therefore determined by the location of the tagged jet relative to the beam direction.

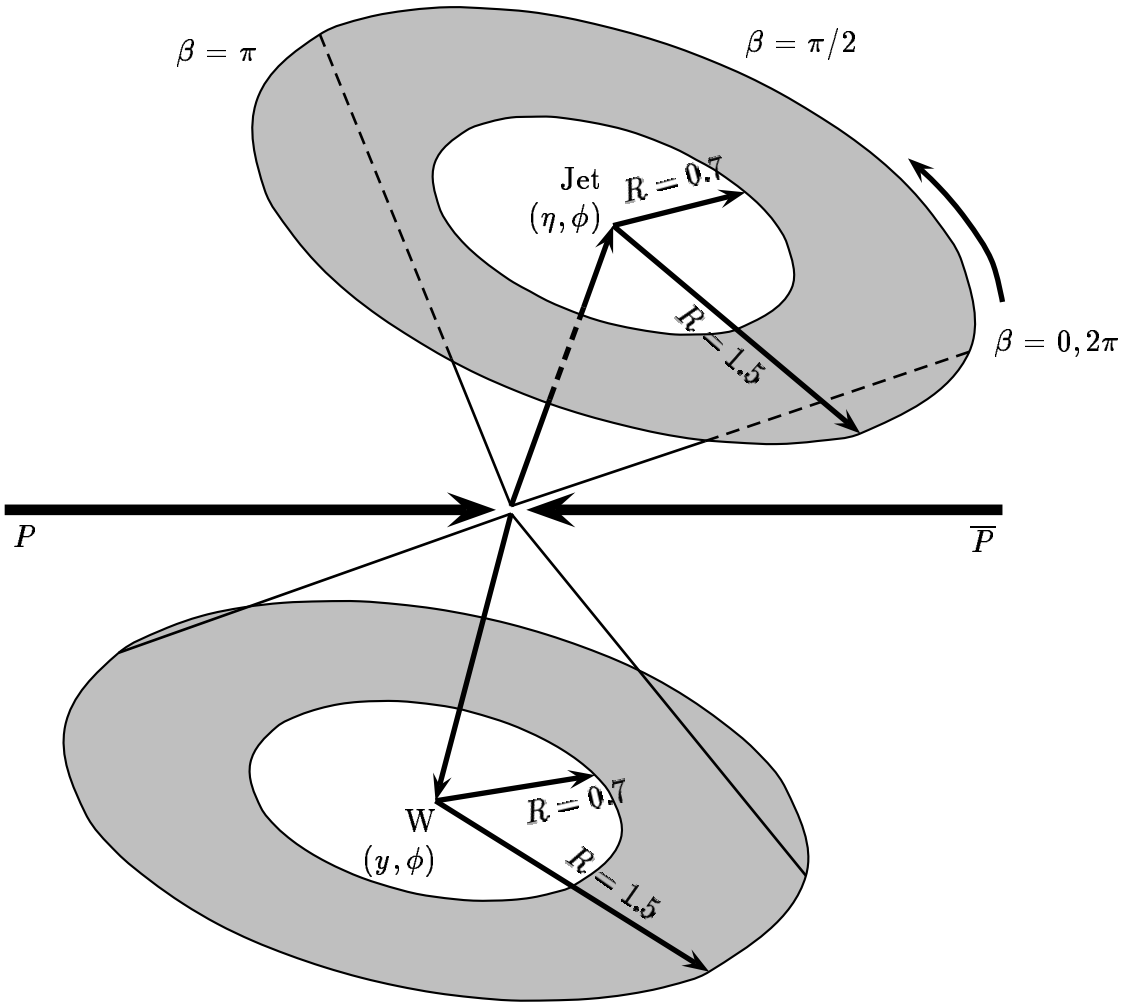

Figure 6.2. Kinematics and variables relevant for energy flow analysis

Once the W boson and the opposing jet have been located in the event, circular—shaped annular regions are drawn around each in (η,ϕ) space. The inner radius R of each region is 0.7 and the outer radius is 1.5, where

$$R = \sqrt{\Delta\eta^2 + \Delta\phi^2}. \tag{6.1}$$

The inner radius was chosen to match the reconstruction radius for the jet, so that energy measurements in the jet annulus are not driven by high energy particles within the jet itself. Although there is no reason a priori to expect that color coherence effects should be absent within the jet cone, the primary objective in this dissertation is the study of soft particle production between hard partons, so the exclusion of energetic particles associated with the jet is required. The measurement of energy flow within the jet, however, remains as a potential secondary analysis. The outer radius was chosen to minimize overlap between the W and jet regions while retaining reasonable statistics.

The outer radius of the annulus in the transverse plane is defined entirely by the ϕ coordinate in the detector. With this radius set to be 1.5, then, each annulus covers just less than one hemisphere of the detector in the ϕ direction ($2R < \pi$). In an event in which the jet and the W boson are perfectly back-to-back in ϕ (i.e. $\Delta\phi_{Jet,W} = \pi$), there is no overlap between the jet and W annuli. However, the extremely loose $\Delta\phi_{Jet,W}$ restriction imposed on the event sample results in a majority of events in which the jet and the W boson are not back-to-back, as shown below in Fig. 6.3. In these events, there is some annular overlap on one side. Any reduction of the outer radius to eliminate the overlap region would significantly reduce the space available for the energy flow measurement. The effect is accounted for, however, by assigning all towers

in the shared region to the nearest object.

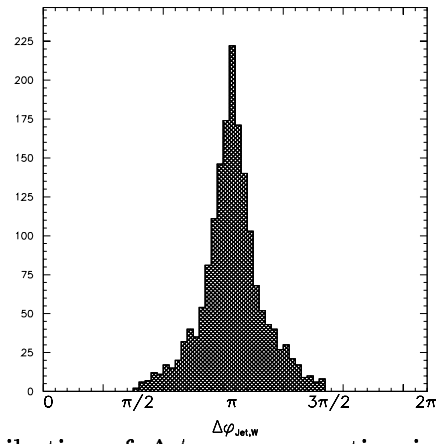

Figure 6.3. Distribution of $\Delta\phi_{Jet,W}$ separation in $W + Jets$ sample. The distribution peaks at π, but extends out to the limits imposed on the data of $\pi/2$ and $3\pi/2$.

6.2.3 The β Variable

An associated angle, β, is defined around the annulus such that $\beta = 0$ and $\beta = \pi$ correspond to the two beam directions (and therefore the event plane), while $\beta = \pi/2$ and $\beta = 3\pi/2$ point to the transverse plane. For every tower in an event, β is determined as follows:

$$\beta_{W,(jet)} = \arctan\left(\frac{\Delta\phi_{W,(jet)}}{\Delta\eta_{W,(jet)}}\right), \tag{6.2}$$

where

$$\begin{aligned} \Delta\phi_{W,(jet)} &= \phi_{tower} - \phi_{W,(jet)} \\ \Delta\eta_{W,(jet)} &= \mathrm{sign}(\eta_{W,(jet)}) \cdot (\eta_{tower} - \eta_{W,(jet)}) \end{aligned} \tag{6.3}$$

The unit multiplier $\mathrm{sign}(\eta_{W,(jet)})$ is a bias introduced in the definition for $\Delta\eta$ so that $\beta_{jet} = 0, 2\pi$ always points towards the beam *nearest* to the jet, while $\beta_W = 0, 2\pi$ always points towards the beam *nearest* to the W boson. These

regions will be referred to as the *near-beam region*, and the region defined by $\beta = \pi$ will be referred to as the *far-beam region*. The near-beam region, by definition, is smaller in phase space than the far-beam region. Furthermore, the far-beam region passes through the central rapidity region of the detector ($\eta = 0$), while the near-beam region is confined entirely to the forward detector regions. Differences in the energetic tower multiplicities are therefore predicted between the near-beam and far-beam regions, so a differentiation is made in the analysis.

If the cylindrical calorimeter is unfolded and laid flat, the disks can be seen as circular rings on an $\eta - \phi$ plane and the near and far-beam regions can be clearly seen. This projection is shown below in Fig. 6.4. In this example, the W boson and the tagged jet are perfectly back-to-back in ϕ, so there is no overlap between the annuli. Since they are located in opposite sides of the calorimeter in η, the locations of the near-beam and far-beam regions are not the same.

6.2.4 The β Distribution

Following the construction of the two annuli, each annulus is sliced radially into equal sections of β. Symmetry of the annuli with respect to ϕ is exploited by folding each region about the symmetry axis, i.e. the semiannular region from $\beta = \pi$ to $\beta = 2\pi$ is folded into the semiannular region from $\beta = 0$ to $\beta = \pi$ for the W and jet annuli separately. This effectively doubles the event statistics, which is important in light of the few events remaining in the analysis sample. This technique is acceptable for W+jets events since there is no color connection between the W boson and opposing jet. This would not necessarily be true for dijet events, for example, in which color connections are possible

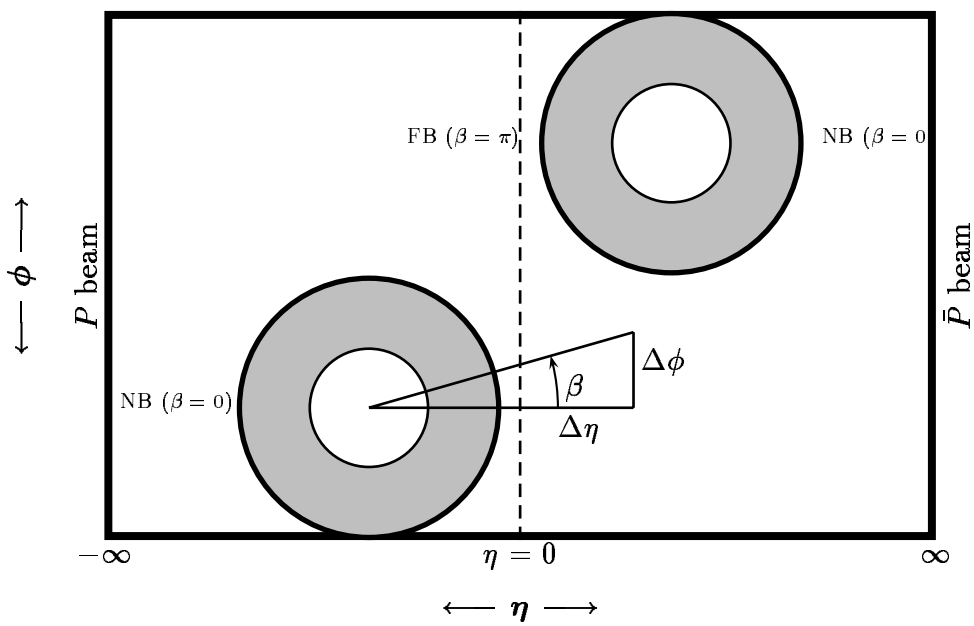

Figure 6.4. Calorimeter view of energy flow variables. Notice that the near-beam (NB) and far-beam (FB) definitions are reversed for the two disks, due to the sign of η_{Jet}, y_W

between the primary jets. The range of β in the folded semiannular region is 0–π, so that $\beta = 0$, $\beta = \pi/2$, and $\beta = \pi$ uniquely define the near-beam, transverse, and far-beam regions, respectively.

For each annulus, the number of towers with $E_T > 250$ MeV is summed in each β section. This number acts as a measure of the number of particles that were produced in each section for the event. Two distributions result,

$$\frac{dN^{Jet}_{towers}}{d\beta} \text{ and } \frac{dN^{W}_{towers}}{d\beta}. \tag{6.4}$$

These are the distributions to be compared for the purposes of removing detector-related effects, thereby illuminating any observable tower patterns in the events. A direct comparison of the W and jet β patterns is provided by the simple division of the two distributions,

$$\frac{d(N^{Jet}_{towers}/N^{W}_{towers})}{d\beta}. \tag{6.5}$$

From theoretical considerations, the expectation is that color coherence will lead to a depletion in the division pattern in the region of the transverse plane ($\beta = \pi/2$) and relative to the event plane ($\beta = 0, \pi$). Additionally, the normalization of the ratio is expected to exceed 1.0 due to greater expected particle multiplicity in the jet annulus than the W annulus.

6.3 Results from Data

The β distributions for the W boson and the tagged jet separately are shown below in Fig. 6.5a and Fig. 6.5b. The number of towers above threshold has been normalized to the total number of available towers in each β bin, so that the figures depict the fraction of towers above threshold for the each region. These curves represent the averages of all of the 254 events in the analysis sample. The vertical error bars on all points represents the statistical error only, while the horizontal error bars represent the bin widths in β.

The most prominent feature of both curves is a strong peaking near $\beta \simeq \pi/2$. This is due to the tight restriction on η_{Jet}, the pseudorapidity of the tagged jet. Events that satisfy this restriction are unlikely to exhibit hard radiation from the jet in the longitudinal direction (i.e. in the event plane), since such radiation would tend to push the jet in a forward direction and out

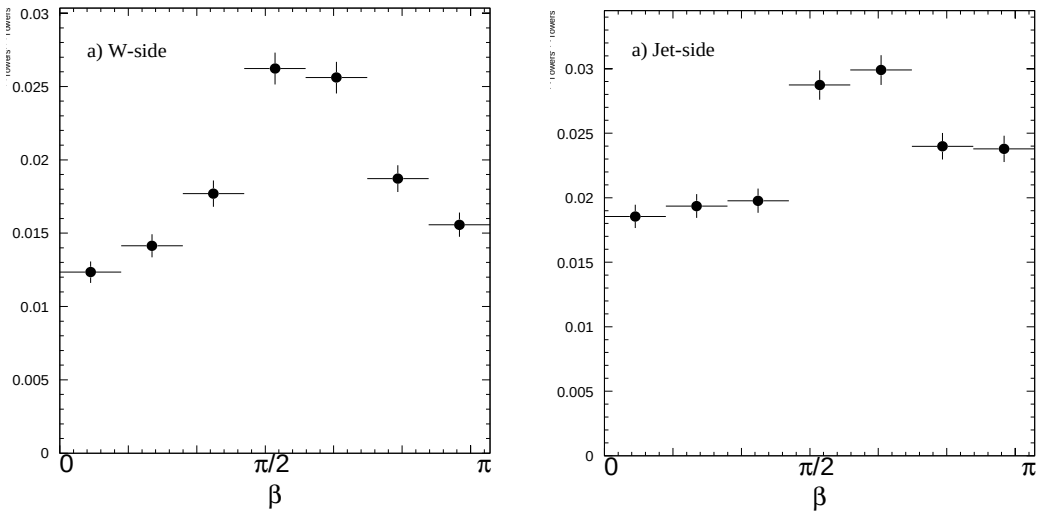

Figure 6.5. Number of towers above 250 MeV E_T threshold, normalized to the total number of towers, for a) the tagged jet region, and b) the W boson region. These plots are averaged over the whole analysis sample.

of the $|\eta|<0.5$ region. Therefore, hard radiation from the jet is more likely to be produced in the transverse (ϕ) direction, where there is little restriction on the jet location. In addition to the effects of hard radiation, there is another kinematic effect of the tight η_{Jet} (and y_W) bound – the transverse plane of each annulus (at $\beta \simeq \pi/2$) corresponds to the most central region of the calorimeter. In this region, less energy is required for a tower to pass the 250 MeV E_T threshold than is required for more forward towers. There are thus more towers in the central region capable of passing the threshold than in the forward regions and, therefore, more towers above threshold in the transverse region of the annuli. Also prominent in these figures is the difference in level in the two event-plane regions. The jet distribution exhibits a much higher fraction of towers above threshold than does the W boson distribution in the near-beam and far-beam regions.

The division of Figs. 6.5a and b is shown below in Fig. 6.6. Here, all of the

features of the W–Jet comparison are present. The error bars represent the propagation of the statistical errors from each distribution through the division. The first observation is that the resulting β pattern *has* a varying shape and that the entire pattern level is above 1.0. This is an excellent indication that the DØ calorimeter is sensitive to E_T differences at the 250 MeV level. A flat ratio pattern at 1.0 would have indicated that the calorimeter could not differentiate energy depositions between the W and jet regions at that level, perhaps due to insufficient resolution or large noise contributions.

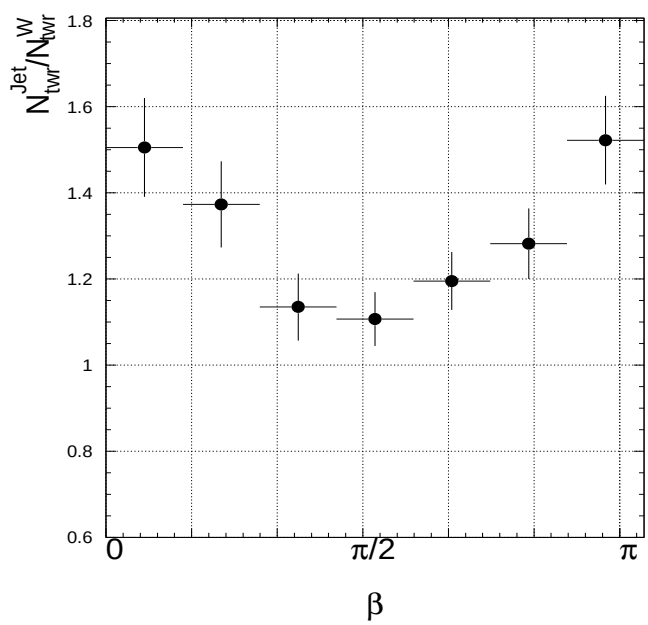

Figure 6.6. Division of jet and W patterns, illuminating differences in energetic tower distributions as a function of the angular variable β.

Aside from providing evidence that the calorimeter *has* the required sensitivity, the overall normalization is otherwise unremarkable. It signifies that there is more radiation on the jet side of the event than on the W boson side, which is expected. The shape of the curve, however, has relevant physics implications. There is clear enhancement of tower multiplicity in the two event

plane regions, with a drop in the transverse region to a level such that the jet and W boson regions have similar multiplicities. The nonuniformity of the pattern suggests that the distribution of energy around the jet is not isotropic, once detector effects have been accounted for. Specifically, the distribution in the transverse plane is depleted with respect to the event plane. In fact, the energetic tower multiplicity in the transverse plane around the jet is only slightly higher than around the nonemitting W boson.

There is a caveat to consider, however. Although dividing the jet and W boson distributions removes most detector effects, there can be contributions to the ratio β distribution due to event-by-event mismatch between the W boson and jet rapidities. As Fig. 6.7 depicts, in any event either object can be as much as 0.5 units in rapidity more forward than the other. This is

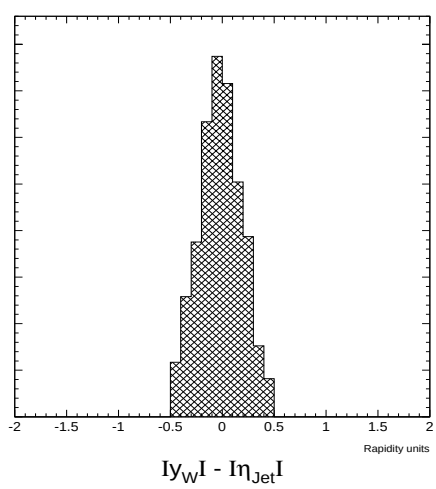

Figure 6.7. Rapidity difference between W boson and jet. Negative entries indicate events in which the tagged jet is more forward than the W boson, while positive entries signify events in which the W boson is more forward.

a potential problem if there are η-dependent calorimeter effects that have not been accounted for. Two such effects, event pileup and zero suppression effects, have been corrected for. However, residual contributions could remain from

these effects and there could be further effects as well, such as η dependence in the calorimeter response. For example, if the calorimeter response at $|\eta|=2.0$ is higher than at $\eta=0.0$, then the number of towers above the 250 MeV threshold at $|\eta|=2.0$ would be artificially enhanced with respect to $\eta=0.0$.

The calorimeter response to low–energy particles at DØ is unfortunately unknown, and so any η dependence in the low–energy response that might exist is unmeasurable. However, a secondary study using *minimum bias* events was performed to determine if η-dependent detector effects could cause the pattern observed in Fig. 6.6.

6.3.1 Minimum Bias Comparison

Minimum bias events are events whose only trigger requirement is an inelastic $\overline{p}p$ collision during a beam crossing, as indicated by the Level 0 scintillation counters. There is thus no bias toward any particular physics process – the event is recorded regardless of what occurred during the collision. Since the cross section for the most common hard scattering processes (low-E_T dijet production) is much lower than the total $\overline{p}p$ cross section, minimum bias events are highly unlikely to contain any hard scattering remnants (such as jets). The vast majority therefore contain only soft scattering, in which the momentum transfer Q^2 is much less than $\sqrt{s}$, resulting in low-p_T final states (see Fig. 6.8 for a rough depiction). The transverse energy of the particles emitted in such events is distributed approximately uniformly in η and ϕ. Color coherence effects are not expected to produce any measurable pattern in these types of events, which makes them very useful as a check on the pattern in the W+jets events.

It is necessary to know if it is possible that the W+jets β pattern is not

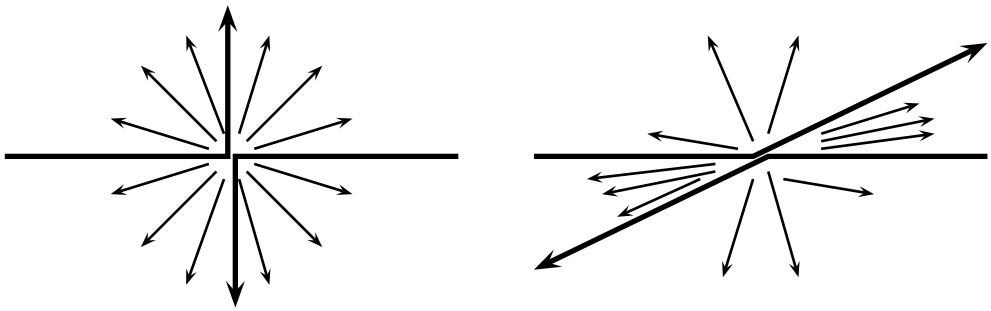

Figure 6.8. Hard (a) and soft (b) $\overline{p}p$ scattering.

due to any interesting physics (such as color coherence), but can be attributed merely to detector effects. If this is true, then the W+jets β pattern should be reproducible at some level in events in which no interesting physics exists, such as minimum bias events.

Events were chosen from a large sample of minimum bias triggers with the following criteria:

- Multiple Interaction Flag = 1
- No Main Ring activity (as defined in Chapter 4)
- $\mid z_{vtx} \mid$<20 cm
- No reconstructed jets

Pedestal offset and zero suppression corrections were applied to all remaining events.

In the W+jets sample, annular regions are constructed around the W boson and tagged jet. Minimum bias events have no such objects with which to center these regions, so random locations must be chosen at which to place them. One random location is designated as the "W" and one as the "jet".

These locations must be representative of W boson and jet locations in W+jets data in order to accurately assess the contribution of residual detector effects. Therefore, weights were applied to the generation of fake W boson and jet locations in minimum bias data to reflect actual W+jets topology. Once an (η,ϕ) coordinate is chosen for each annulus, the analysis proceeds the same as for the W+jets sample. Figs. 6.9a and 6.9b show the comparison of azimuthal and rapidity separation of the W boson and tagged jet between the min bias events and W+jets events.

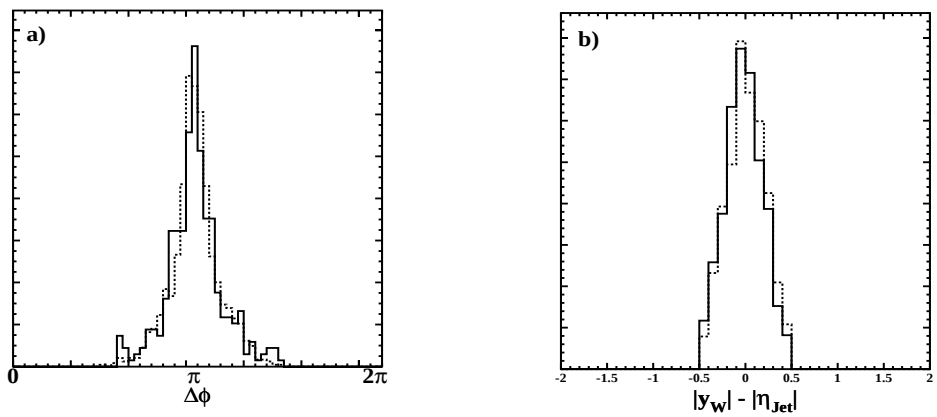

Figure 6.9. a)Distribution of $\Delta\phi$ for the W boson and jet for W+jets (solid line) and fake W+jets locations from min bias (dashed line) data. b)Distribution of $\mid y_W \mid - |\eta_{Jet}|$ for W+jets (solid) and min bias (dashed) data. Negative values in second plot indicate events in which the tagged jet was more forward than the W boson, and vice versa for positive values.

The comparison of the β distributions in Fig. 6.10 shows extremely different energetic tower patterns for the min bias data relative to the W+jets data. Within statistical errors, The min bias β pattern is a uniformly flat distribution with ratio values of $\simeq$1.0. This is evidence that there is a real effect in the W+jets data, one that may have residual detector-related contributions but which cannot be attributed solely to detector effects.

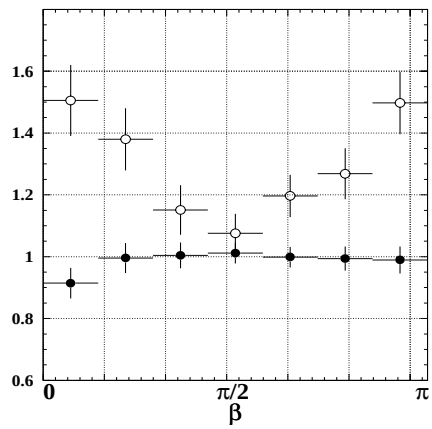

Figure 6.10. Distribution of towers above threshold around the tagged jet divided by the distribution around the W boson in W+jets data (open circles) as compared to the distribution of towers above threshold around the "jet" divided by the distribution around the "W" in min bias data (closed circles).

6.4 PYTHIA *Monte Carlo Simulation*

The β distributions from W+jets data are compared with predictions from the PYTHIA Monte Carlo simulation program as a means of understanding the pattern observed in data. PYTHIA is an excellent choice for this comparison due to the many options it provides the user with respect to angular ordering and fragmentation implementations. PYTHIA simulates hard scattering to leading-order and is capable of approximating color coherence effects during parton evolution in both the initial and final states. It employs the Lund string model by default in the fragmentation process, but also contains the full machinery for independent fragmentation if the user desires.

PYTHIA approximates color coherence through angular ordering and azimuthal correlations. At each gluon branching, an opening angle is generated subject to the constraint set by the previous branching (the AO constraint). The azimuthal angle of the emitted gluon is chosen uniformly for branchings from the initial-state partons. For branchings from final-state partons, how-

ever, the azimuthal angle is influenced by the color partner of the emitting parton. This influence is manifested as a probability distribution for the azimuth that is maximized in the plane formed by the emitting parton and its color partner and in the region between them (as described in Chapter 2).

W+jets events were simulated with PYTHIA through the leading-order processes $q\overline{q} \rightarrow Wg$ and $qg \rightarrow Wq$ for $\overline{p}p$ interactions at Tevatron center-of-mass energies. Three classes of events were generated – one with coherent parton evolution and string fragmentation, one with incoherent parton evolution and string fragmentation, and one with incoherent parton evolution and independent fragmentation. They will be referred to as samples I, II, and III, respectively. These three classes represent various "levels" of color coherence implementation, and allow explicit testing of the nonperturbative fragmentation contributions independent of the partonic shower development while fixing all other event characteristics. PYTHIA thus provides an internally consistent platform for probing color coherence effects. The number of simulated events is 25K for sample I and 15K each for samples II and III.

6.4.1 Detector Simulation

Events were generated at the particle level and then processed with the Shower Library detector simulator[65]. Shower Library is a database of detailed calorimeter shower information from the mixture-level GEANT detector simulation for about 1.2 million particles. Mixture-level GEANT is a simulation of the detector in which the calorimeter layers are treated as a uniform mixture of uranium and liquid argon, as opposed to separate uranium absorber and liquid argon gap regions. These particles are binned according to specific kinematic variables: z vertex displacement, pseudorapidity, momentum, particle type (electromag-

netic, hadronic, or muon), and azimuthal angle. The lowest momentum bin is 100-320 MeV. For each particle, the energy and location of each cell associated with its calorimeter shower is stored, up to a maximum of 42 cells. For each particle in a Monte Carlo event, a random shower from the Shower Library is chosen, subject to the requirement that the Monte Carlo particle and the Shower Library particle that initiated the shower belong to the same bin in each of the five kinematic variables above. The energy of the shower is scaled according to the Monte Carlo particle energy and the shower cell information is then stored in the event.

This method results in an "approximation of an approximation" for the DØ detector, but is expected to be precise enough for the study of large ensembles of particles. Shower Library has been shown to give results that are in excellent agreement with the full GEANT detector simulation for comparisons of total event energy, total event E_T, ICD/MG energy, $\not{E}_T$, and dijet invariant mass[65]. Further, there is internal consistency among the three PYTHIA samples, and so comparisons among them are sensitive only to differences in the particle generation and not the detector simulation.

There is an additional feature of the detector simulation to be considered. The DØ detector contains a small uninstrumented region of the electromagnetic calorimeter coverage, and another small uninstrumented region of the hadronic coverage. The locations of these regions can be seen in Fig. 6.11. The x-axis of this figure is marked in units of IETA, while the y-axis labels the various contributing layers to a given tower (the ϕ coordinate is not shown). The missing hadronic section spans the range IETA=9 to IETA=12 (and -9 to -12 in the half not shown), while the missing electromagnetic section spans IETA=12 to IETA=14 (and -12 to -14). These correspond to regions *between* the CC

Figure 6.11. Schematic depiction of layer structure in IETA of calorimeter towers (1/2 of detector shown).

and EC cryostats. The ICD and MG layers were included to compensate for the measurement loss in this region, and they have proven quite valuable in improving the hadronic coverage. This is not so for the electromagnetic coverage, however, where less ICD and MG coverage is available and much electromagnetic energy is lost in the intervening material. In the real detector, the sampling weights for the ICD cells were increased to help compensate so that jet energy measurements would not suffer. However, this was not done to the same degree in the detector simulation, and the result is that the detector response at the tower level is quite low in the uninstrumented electromagnetic region for Monte Carlo events ($\sim$50%). Due to the response mismatch between data and Monte Carlo, this region is eliminated from the β measurements in

both. Thus, *no* towers are included in the β distributions for IETA=$\pm$ 12, 13, or 14.

6.5 *Analysis of* PYTHIA *Events*

Events in all three samples were reconstructed with the DØRECO package following the Shower Library simulation. They were then subjected to the same set of cuts as the data events, with the exception of the multiple interaction flag cut. Since there is no timing information available for the Level 0 scintillation counters in the Monte Carlo events, no multiple interaction probability is calculable. However, no multiple interaction events were generated, so this cut would be unneeded anyway. Sample I had 4026 events surviving all cuts, Sample II had 2639 events, and Sample III had 2679 events.

6.5.1 *Kinematic Comparison with Data*

In order to have confidence that PYTHIA represents the W+jets production well, certain kinematic comparisons must be made with the data similar to those made with the full GEANT simulation, but oriented toward W+jets events. Many event characteristics (e.g. $\not{E}_T$) should be similar between PYTHIA and data if PYTHIA, combined with Shower Library, models the W+jets production well.

As seen in Figs. 6.12a – 6.12d and Figs. 6.13a – 6.13b, agreement between data and Monte Carlo is generally good. However, there do seem to be some discrepancies in the W boson p_T and tagged jet E_T comparisons (Figs. 6.13c and 6.13d). This may be due to differences in jet reconstruction efficiency between data and particle-level Monte Carlo, and due to calorimeter noise effects in data that do not contribute to the Monte Carlo events at reconstruction time.

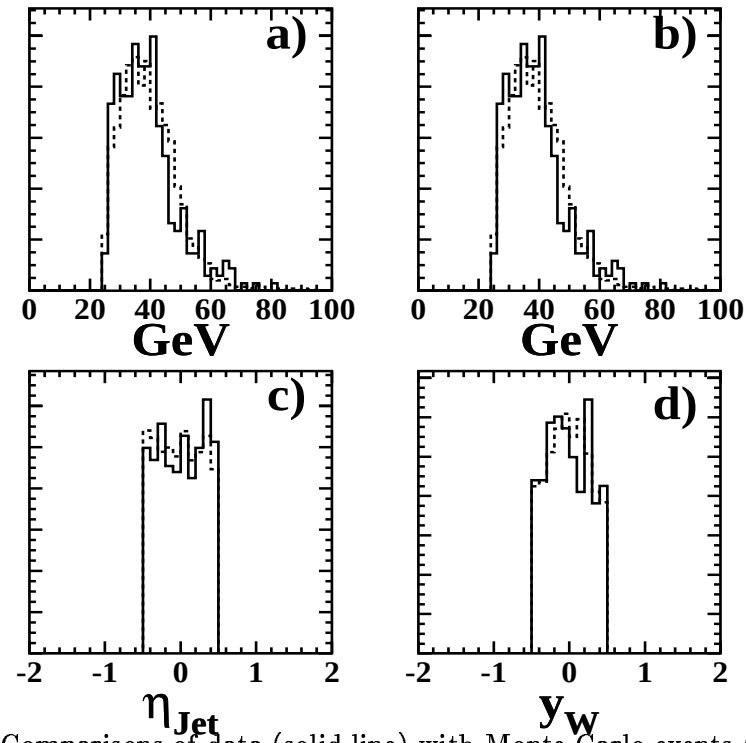

Figure 6.12. Comparisons of data (solid line) with Monte Carlo events (dashed line) for **a)**Electron E_T, **b)**$\not{E}_T$, **c)**Tagged jet η, and **d)**W boson rapidity.

Noise effects are added to Monte Carlo events, but only post-DØRECO (see next section). A further contribution could be relatively tight restrictions on the W boson p_T and jet E_T during generation (necessary to maximize the efficiency for events passing all analysis cuts). Adjusting the jet E_T requirement up to 10 GeV brings the distributions into satisfactory agreement (see Figs. 6.14a and 6.14b). This change is reflected in all subsequent measurements.

6.5.2 Calorimeter noise

As detailed earlier, all calorimeter cells in the collider data are corrected for zero suppression effects and pedestal offsets. This has the effect of zeroing the average cell energy distribution (in the absence of real particles). Fluctuations

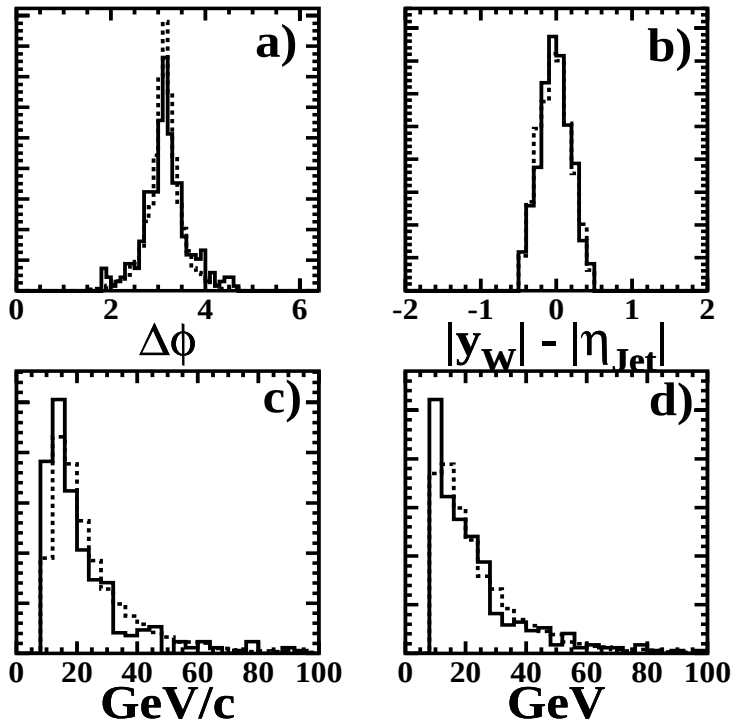

Figure 6.13. Comparisons of data (solid line) with Monte Carlo events (dashed line) for **a)**Azimuthal separation of W boson and tagged jet, **b)**Rapidity separation of W boson and tagged jet, **c)**W boson p_T, and **d)**Tagged jet E_T.

around zero remain, however, due to residual calorimeter noise. This noise is not modelled in the detector simulation, and must therefore be specifically added to the Monte Carlo cells for each event. The best way to accomplish this is to overlay noise contributions from real collider data. In such a case, calorimeter noise affects the Monte Carlo events in the same way as it does data.

Fortunately, the non-zero suppressed zero bias sample used to derive the pedestal offset correction is the best source for residual noise. Once the cells in this sample have been corrected for pedestal offsets, the only energy remaining is that due to noise. For each event, then, all cells were corrected and the residual energies were written to a data file. There were approximately 1700

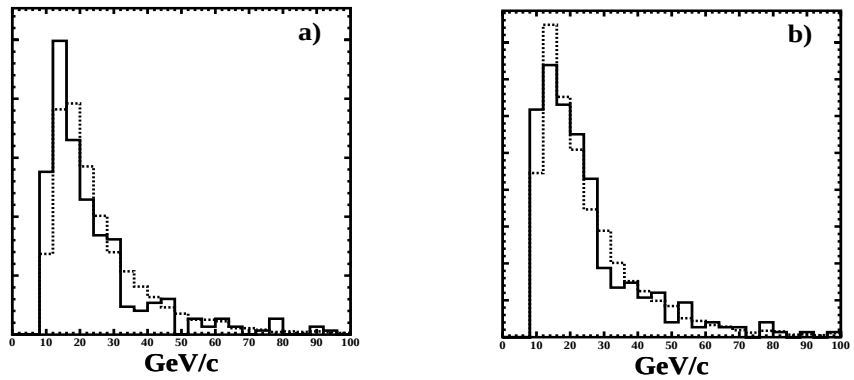

Figure 6.14. Comparisons of data (solid line) with Monte Carlo events (dashed line) after new tagged jet E_T cut for **a)**W boson p_T and **b)**tagged jet E_T.

good events in the zero bias sample, which resulted in approximately 1700 files of calorimeter noise energy.

For each Monte Carlo event, a zero bias data file was read in and the energy of each zero bias cell was added to the appropriate Monte Carlo cell. All Monte Carlo cells were then zero suppressed in the same manner as the collider data were. The 2σ threshold was determined from the zero bias data. The RMS for each zero bias cell was calculated after summing over the 1700 events:

$$(RMS)_{cell} = \sqrt{\langle E_{cell}^2 \rangle - \langle E_{cell} \rangle^2} \tag{6.6}$$

The RMS for a particular cell was taken as σ for the energy distribution of that cell for all events. This is correct for Gaussian distributions and is the same strategy as was used in the collider data.

6.6 *Results from* PYTHIA

For each PYTHIA sample, β distributions were constructed as they were in the data: annular regions were drawn around the W boson and tagged jet, towers

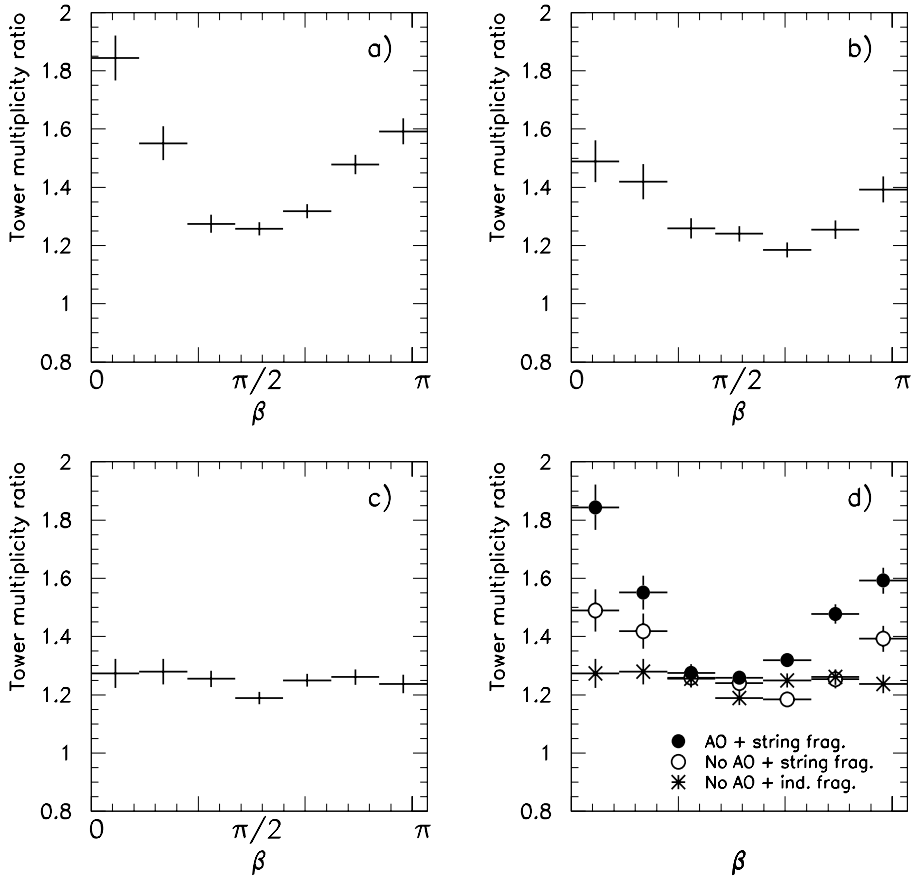

Figure 6.15. Divisional β distribution for PYTHIA samples – a)**Sample I** (angular ordering and string fragmentation), b)**Sample II** (no angular ordering, but still with string fragmentation), c)**Sample III** (no angular ordering and independent fragmentation), and d)**All** samples overlayed.

with E_T>250 MeV were summed in each region for all events as a function of β, and the jet distribution was divided by the W boson distribution to reveal the pattern differences in β.

Figs. 6.15a-c show the results for the three PYTHIA samples, while Fig. 6.15d shows the comparison of all three samples. The curves in Fig. 6.15a and Fig. 6.15b both exhibit the same general features as the curve in data – the overall normalization is higher than 1.0 and there is a pronounced dip in the

transverse plane. Fig. 6.15c, by contrast, is relatively flat across the range of β. These observations lend confidence to the assertion that the level of the β pattern in data is due to particle multiplicity differences between the W boson and jet annuli (as opposed to some unaccounted for detector or kinematic effect).

6.6.1 Particle-Level Measurement

It is instructive to compare the β patterns of energetic towers in the PYTHIA samples with detector simulation to β patterns of energetic *particles* in the samples. In this way, color coherence effects can be observed in PYTHIA directly at the particle level and also effects of the detector simulation on the particle-level distributions may be monitored.

The technique for measuring the β distribution of particles in the PYTHIA samples is the same as for the tower measurement. That is, for every particle above some E_T threshold in a PYTHIA W+jets event, β is determined as follows:

$$\beta_{W,(jet)} = \arctan\left(\frac{\Delta\phi_{W,(jet)}}{\Delta\eta_{W,(jet)}}\right), \tag{6.7}$$

where

$$\begin{aligned} \Delta\phi_{W,(jet)} &= \phi_{particle} - \phi_{W,(jet)} \\ \Delta\eta_{W,(jet)} &= \mathrm{sign}(\eta_{W,(jet)}) \cdot (\eta_{particle} - \eta_{W,(jet)}). \end{aligned} \tag{6.8}$$

The annular construction and subsequent measurement proceeds just as for the tower β measurement. For consistency, the W boson in the particle-level events is reconstructed from its decay products, rather than using its known trajectory. Jets in particle-level events are reconstructed with a variant of the cone algorithm that employs particles instead of towers. The cone radius (R=0.7) and reconstruction threshold (E_T>8 GeV) were chosen to be the same

as in the data. Particle–level events were subjected to the same fiducial and kinematic cuts as the Shower Library events — detector–specific cuts such as electron quality cuts and jet quality cuts were not imposed.

The most obvious question regarding the particle measurement is what E_T threshold to use, or why use a threshold at all? Clearly, it is most straightforward to simply count all particles, without the use of an E_T cut. This does not provide the best means for comparing the particle β pattern with the Shower Library tower β pattern, however. Selecting only towers with E_T>250 MeV in the calorimeter is sure to bias the E_T distribution of particles to higher values.

A secondary study was conducted to explore potential particle E_T thresholds that would be comparable to the tower E_T threshold. Sample I was used for this purpose. For all events, the η and ϕ of each particle was converted into integer values that correspond to the tower coordinate system, IETA and IPHI. An E_T distribution was created for those particles whose (IETA,IPHI) location matched a tower with E_T>250 MeV. The results are shown below in Figs. 6.16a and 6.16b. The E_T distribution for all particles peaks at ~200

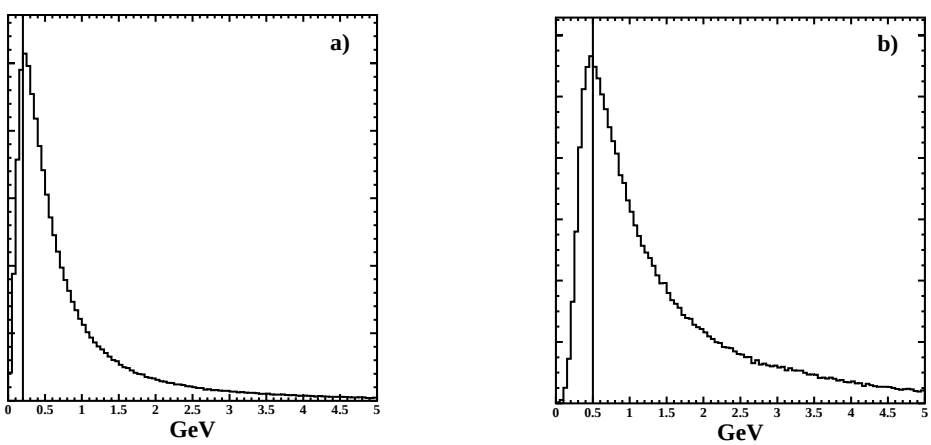

Figure 6.16. E_T distribution for a)all particles and b)particles with a matched tower above 250 MeV in E_T.

MeV, while the E_T distribution for particles depositing E_T>250 MeV into a single tower peaks at ~500 MeV. Both distributions drop sharply below the peak value. Therefore, if a 500 MeV threshold was imposed on the particles for the purposes of a β measurement, the efficiency would be good for measuring the pattern of particles believed to result in towers with E_T> 250 MeV. This is admittedly a rough estimate of the particle-level threshold, but is nonetheless a reasonable guide to the particle-level pattern selected by the calorimeter–level measurement.

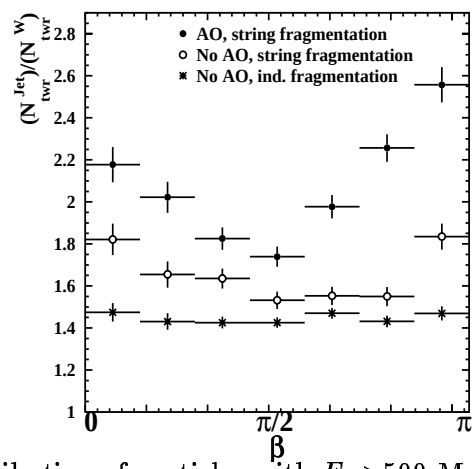

Figure 6.17. Distribution of particles with E_T>500 MeV for all three PYTHIA samples.

Fig. 6.17 shows the $\frac{\text{Jet}}{\text{W}}$ β distributions for all three PYTHIA samples. The trends in these distributions are very similar to what is seen at the calorimeter level. The pattern for Sample I shows a large dip in the transverse plane. The shape is much less pronounced in Sample II, while the shape for Sample III is flat. It is noteworthy that the overall level for these curves is higher than is seen in the towers measurements. This is likely due to the noise contributions and Shower Library smearing in the calorimeter towers, which are symmetric in ϕ. Towers with little particle energy can still pass the 250 MeV threshold

with sufficient positive noise fluctuations and Shower Library smearing. The combined result of these effects is additional towers with E_T>250 MeV in both the tagged jet and W boson event regions, which serves to drive the $\frac{\text{Jet}}{\text{W}}$ normalization closer to one.

Given the rough estimate of the particle E_T threshold, care should be exercised in comparing the particle and calorimeter β patterns. In particular, it is important to know if the particle pattern is stable over some range of E_T cuts, so that the comparison is useful even if the chosen threshold has some associated error. The peak region of Fig. 6.16b spans the range 400 MeV–600 MeV in E_T. Particle β patterns were therefore measured for E_T thresholds of 400 MeV and 600 MeV for comparison with the 500 MeV pattern. An additional β plot was constructed with no threshold, to observe the pattern for *all* particles. Results are shown below in Fig. 6.18. There is virtually no change in the

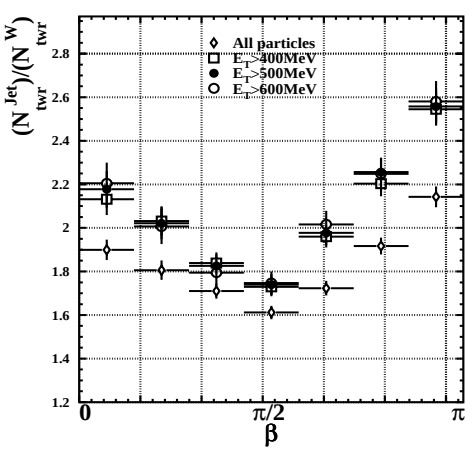

Figure 6.18. Distribution of particles for various E_T cuts in Sample I.

pattern for E_T cuts from 400 MeV to 600 MeV. This is evidence that the peak value of 500 MeV is a reasonable value for comparison with the calorimeter pattern. With no E_T cut, however, the pattern is slightly altered. In addition to a drop in the overall level, the pattern also shows less variation between the

event plane and the transverse plane.

6.6.2 Particle-Calorimeter Comparison

The comparison of particle-level patterns with calorimeter-level patterns is made for a particle E_T cut of 500 MeV. The progression of the particle-level pattern studied in the previous section leads to the conclusion that a variation of ± 100 MeV from this value is not significant.

It has been established that the particle-level distributions exhibit higher overall levels than the Shower Library distributions. All distributions are therefore normalized to equal area so that the shape differences may be studied independent of level differences. Within errors, the patterns agree quite well for Samples II and III. There appears to be some shift in the pattern for Sample I, however. The particle-level pattern shows an asymmetry which favors the far-beam side of the distribution, while the Shower Library pattern shows an asymmetry to the near-beam side.

6.7 Color Coherence in the Collider Data

Two alterations have been introduced into the analysis through an investigation of the Monte Carlo simulation – a higher E_T cut has been placed on the tagged jet and a low-response region has been removed from the detector. Before comparing the β patterns in PYTHIA with that in data, a check should be made to determine how these secondary cuts affect the pattern previously observed in the data. The comparison is shown in Fig. 6.20. The only difference between the two patterns is a slight enhancement of the near beam with the secondary cuts that is still within the statistical error.

The comparisons may now be made of the various PYTHIA simulations with

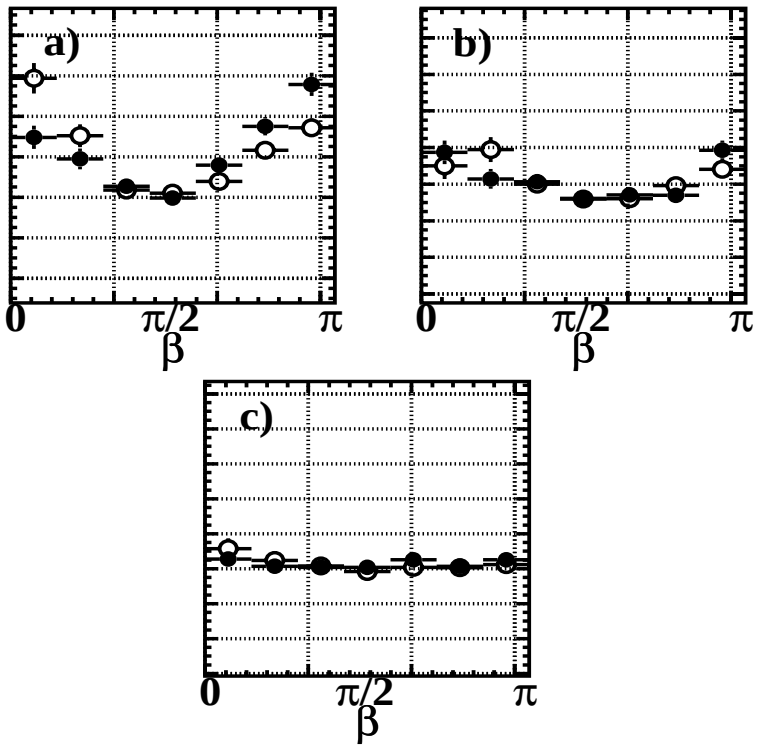

Figure 6.19. Comparison of particle-level β distributions (closed circles) and Shower Library β distributions (open circles) for a) Sample I, b)Sample II, and c)Sample III. All distributions are normalized to equal area.

data at the detector level. The PYTHIA β distributions are known to have a higher overall normalization than in data. However, it is the relative *shapes* of the distributions that are central to this analysis. For this reason, the normalization for all β distributions has been changed so that all distributions have equal area (as was done for the particle-level/Shower Library comparison). With the normalization set the same for all samples, shape differences are highlighted in the comparisons, thus isolating the physics of interest. Figs. 6.21– 6.23 show the comparisons of PYTHIA with data. In all plots, the closed circles represent the collider data and open circles represent the PYTHIA samples. All errors are statistical.

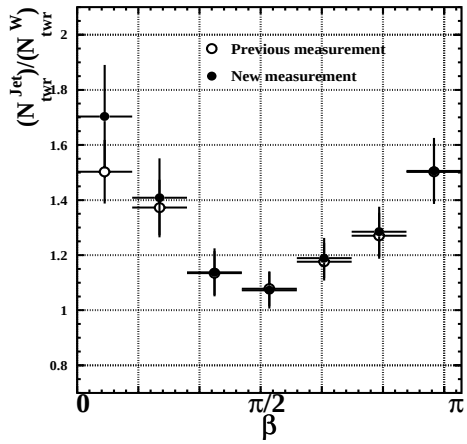

Figure 6.20. Energetic tower distribution in data with new changes (closed circles) and without new changes (open circles).

The shape from Sample I (Fig. 6.21) agrees well with the shape from data. All PYTHIA points are within one sigma of the data points. The distribution of towers around the jet in data shows pronounced depletion in the region transverse to the plane of the event as compared to the distribution around the W boson. This indicates preferential energy flow in the plane of the event in the data W+jets events and is adequately reproduced by PYTHIA for the first sample. The asymmetry favoring the near–beam side of the distribution is equally represented in both PYTHIA and data.

The shape for Sample II (Fig. 6.22) agrees less well with the collider data. The same global features are present, but the curvature is less pronounced. This shows that the energetic tower distribution around the jet in this sample is more uniform than in data or in the first sample. There is thus less preference for event–plane radiation in Sample II relative to the transverse plane.

Lastly, Sample III exhibits a shape in β (Fig. 6.23) that diverges from the shape in data markedly. Specifically, there is no significant variation in β of the Sample III line shape, implying no preference at all for radiation in the event

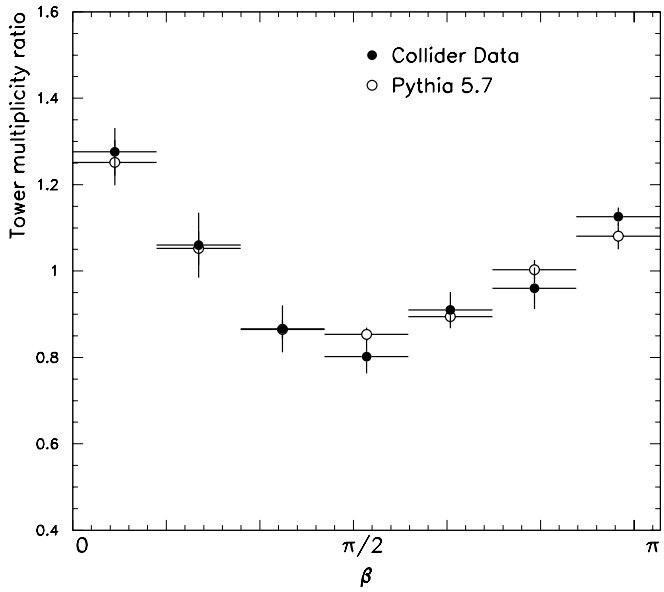

Figure 6.21. Comparison of normalized β distributions for data and PYTHIA Sample I (angular ordering and string fragmentation).

plane in the vicinity of the jet. In other words, while the scattering process results in more radiation in the vicinity of the final-state hard parton than the of the W boson (as was seen from the overall pattern level), it seems to distribute that radiation in an isotropic fashion so that the distribution in the jet annulus is otherwise indistinguishable from the distribution in the W boson annulus. This prediction contrasts with observations from data, in which the shape of the β distribution as well as the level distinguishes the two.

6.8 Threshold Dependence

As was previously mentioned, the 250 MeV E_T threshold for the towers was chosen as a balance between the need to minimize noise contributions and the need to retain reasonable statistics. There is otherwise nothing particularly enlightening about the choice of 250 MeV. To demonstrate this, and to

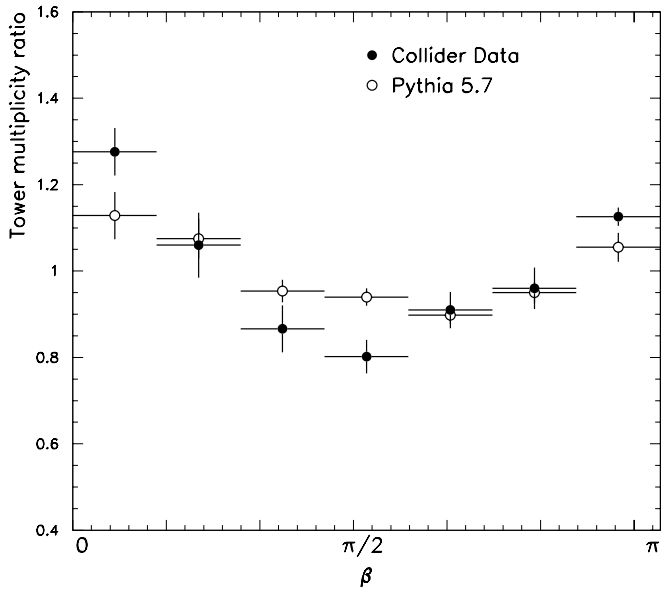

Figure 6.22. Comparison of normalized β distributions for data and PYTHIA Sample II (no angular ordering, but with string fragmentation).

simultaneously demonstrate the noise effects on the signal, β measurements were made in the data for several tower E_T thresholds from 0 MeV up to 350 MeV. The combined results are shown in Figs. 6.24a and b. The change in the β pattern can be seen in these figures as the threshold is varied by 50 MeV increments. With the threshold set at 0 MeV, the measurement probes the distribution of *all* towers with positive E_T. There is no noticeable deviation from a straight line. As the threshold is increased up to 150 MeV (Fig. 6.24a), there is a corresponding increase in the near-beam and far-beam ratio values. As Fig. 6.24b shows, the pattern is stable in the near-beam region for thresholds of 200 MeV and greater, while the far-beam region continues to rise. The statistics are quite low for thresholds above 250 MeV, however.

These figures demonstrate that the characteristic β pattern seen for the 250 MeV E_T threshold is present for a range of thresholds, and that the chosen

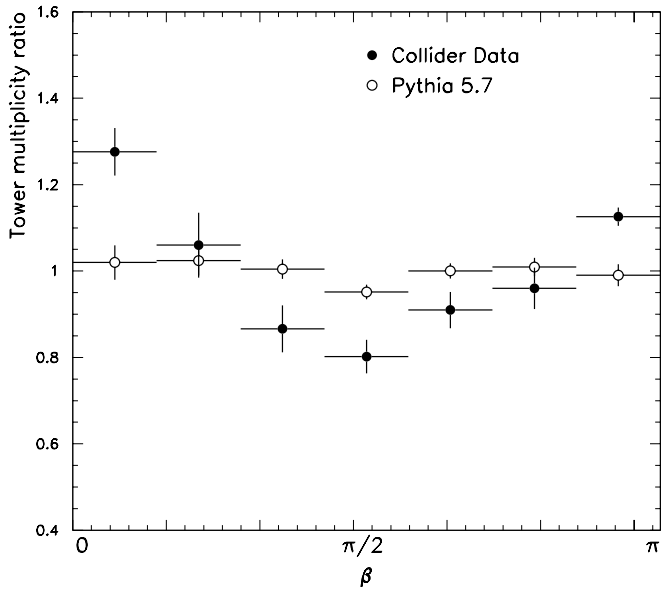

Figure 6.23. Comparison of normalized β distributions for data and PYTHIA Sample III (no angular ordering and independent fragmentation).

value for the analysis is not unique in its ability to exhibit transverse-plane depletion in the distribution of towers. A similar comparison may be made with the PYTHIA events to demonstrate the effects of noise and calorimeter showering as a function of threshold. Sample I is chosen for this comparison because color coherence is explicitly included in this sample and has been observed in both particle and tower distributions. Fig. 6.25 shows that, with a 0 MeV threshold, the observed pattern is washed out, resulting in a pattern very similar to the one seen in PYTHIA events with incoherent parton evolution and independent fragmentation (Sample III). Recall that the particle-level pattern with 0 MeV threshold had a clear signal, whereas none is seen at the calorimeter level. The noise in the cells and particle showering in the calorimeter can result in many low-E_T towers spread out over the event which pass low-E_T thresholds. The presence of these towers drives the Jet/W ratio closer to 1.0

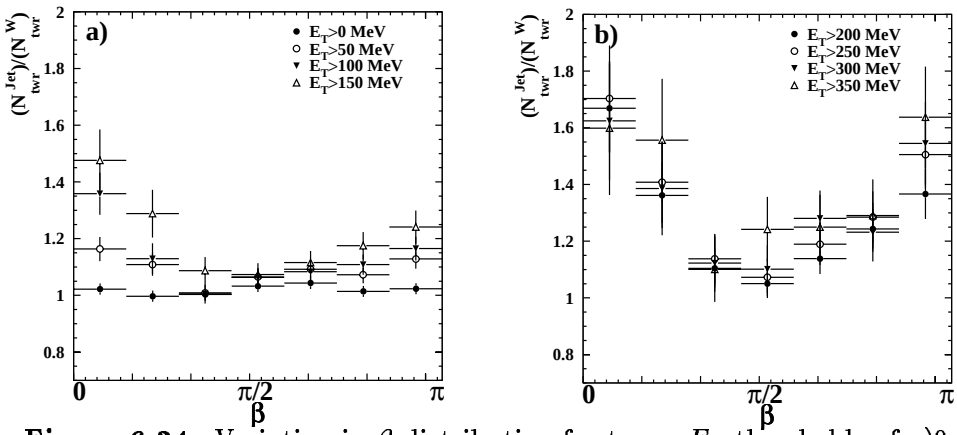

Figure 6.24. Variation in β distribution for tower E_T thresholds of a)0 MeV to 150 MeV and b)200 MeV to 350 MeV.

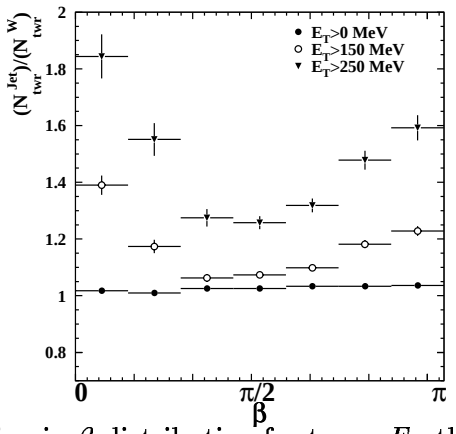

Figure 6.25. Variation in β distribution for tower E_T thresholds of 0 MeV, 150 MeV, and 250 MeV in Sample I from PYTHIA.

for these thresholds. As the threshold is increased up to 250 MeV, however, the characteristic pattern becomes clear.

6.9 Systematic Uncertainties

Thus far, all errors shown for the β plots have been statistical only. It is expected that statistical errors should dominate any systematic uncertainties due to the low event statistics in the data. The sources of systematic uncertainty investigated for this analysis are identified as: trigger biases, contamination

from background to W+jets events, uncertainty in the pileup and zero suppression corrections, changes in calorimeter response as a function of η, luminosity dependence of the data signal, and ambiguity in the reconstructed W boson rapidity.

The first has already been mentioned – events are selected based on kinematic cuts such that the Level 2 trigger is ~100% efficient, so no trigger bias is present. The kinematic matching of data and Monte Carlo (such as for electron E_T and $\not\!\!E_T$) helps confirm this. The rest are described separately.

6.9.1 Background Contamination

The primary background to W+jets events is dijet production in which one of the jets mimics the characteristics of a W boson decay electron. The $\not\!\!E_T$ typically arises from the response difference between the two jets when one fluctuates to a high electromagnetic fraction (and thus becomes an electron candidate). The method of determining the background, which is described in detail in [66], is to construct $\not\!\!E_T$ distributions from two W+jets candidate samples (using a trigger *without* a $\not\!\!E_T$ cut) – one in which the electron candidate passes all requirements (and therefore contains real and fake W+jets events) and one which contains almost all background (by selecting electron candidates with *very* poor electron characteristics). The shape of the $\not\!\!E_T$ distribution in the background sample in the region above 25 GeV (the lower limit in the analysis) then describes the background contribution in the sample with real and fake electrons. The two $\not\!\!E_T$ distributions are area normalized in the low $\not\!\!E_T$ region, and the normalization factor is used to extract the background fraction in the analysis sample (whose trigger *has* a $\not\!\!E_T$ threshold).

The cuts imposed on W+jets candidates for this analysis are extremely tight

so as to reduce the background fraction as much as possible. This is because, for a dijet background event which survives all cuts, a W boson would be reconstructed most likely in the ϕ hemisphere of the fake electron. The presence of a jet on the side of an event where a W boson was reconstructed would result in a contamination of the β measurement for the fake W boson annulus. The event selection strategy was therefore centered on reducing the background to insignificant levels. The background analysis process was applied to events with color coherence W+jets selection cuts, and the resulting background estimate was ~2%[67]. This is a very low fraction, especially in light of the event count in the analysis sample (254). So, the expectation is that two or three events in the analysis sample are actually dijet events.

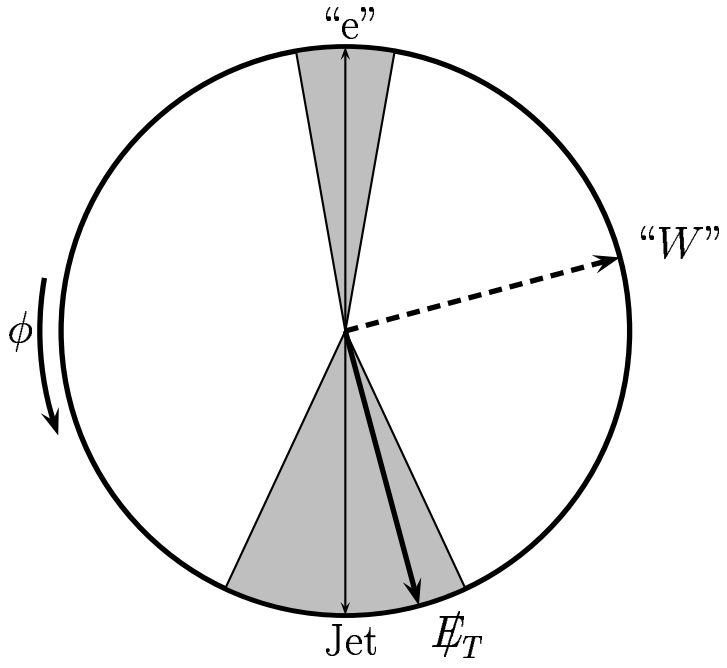

Figure 6.26. Example of fake W boson reconstruction from a dijet event in the ϕ plane (beam direction perpendicular to page).

The kinematics of a fake W boson reconstruction from a dijet event are shown in Fig. 6.26. The two jets are generally produced back-to-back in the ϕ direction and the $\not\!\!E_T$ vector usually points near the hadronic jet. The jet mimicking the electron must be very narrow to pass the electron isolation requirement. The W boson reconstructed in such an event will be located somewhere in the ϕ hemisphere of the fake electron, the exact coordinate depending upon the $\not\!\!E_T$ vector.

With such a low background fraction, it is not possible to acquire a sample of background events and measure the β distribution of energetic towers in them. As a conservative approximation, however, the jet distribution in the W+jets events may be used for this purpose. In each W+jets event in the analysis sample, a random ϕ coordinate is chosen that is within $\pi/2$ of the tagged jet. This coordinate, along with the η of the tagged jet, can serve as the location for a new annular region corresponding to a fake W boson location. This region will obviously contains contamination from the tagged jet distribution, which is also what happens in background events – the fake W boson annulus contain contamination from the jet mimicking the electron. A "background" β measurement is then made by:

$$R_\beta = \frac{N_\beta^{Jet}}{N_\beta^{\text{“}W\text{''}}}, \tag{6.9}$$

where N_β^{Jet} and $N_\beta^{\text{“}W\text{''}}$ are the number of towers above threshold in a particular bin of β in the tagged jet and fake W boson annuli, respectively. The resulting pattern, Fig. 6.27, has no distinguishing characteristics. This distribution was then subtracted from the analysis sample β pattern at the 2% level to determine the effect on the β measurement in data. The result is shown in Fig. 6.28.

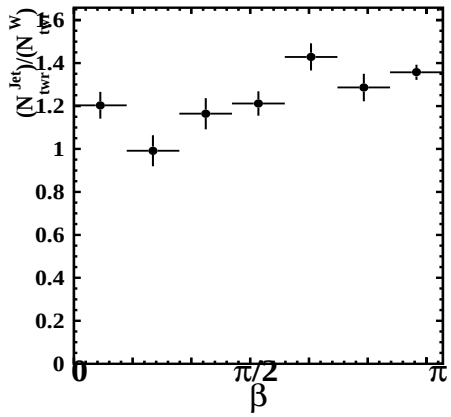

Figure 6.27. Distribution in β of simulated background sample.

There is no statistically significant change in the observed β pattern when the

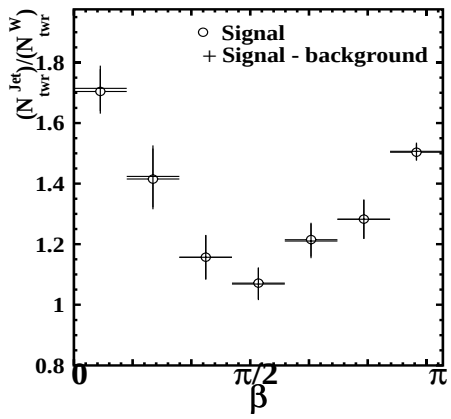

Figure 6.28. Effect of approximated background subtraction in β measurement.

background was subtracted. The two distributions agree to the point that a systematic error assigned for the background contribution is not warranted.

6.9.2 Pileup and Zero Suppression

The pileup and zero suppression corrections have been shown to reduce their contributions to cell energies to less than 1 MeV/cell. Errors in this correction are therefore not expected to significantly affect the β measurement in W+jets

data. Some potential sources of error in these corrections are unaccounted for luminosity dependence, drift in the pedestal offsets in time, and event-by-event fluctuations in the noise.

To determine if a systematic error is needed for these corrections, they were varied by $\pm 50\%$ The comparisons are shown in Fig. 6.29. There are point-to-

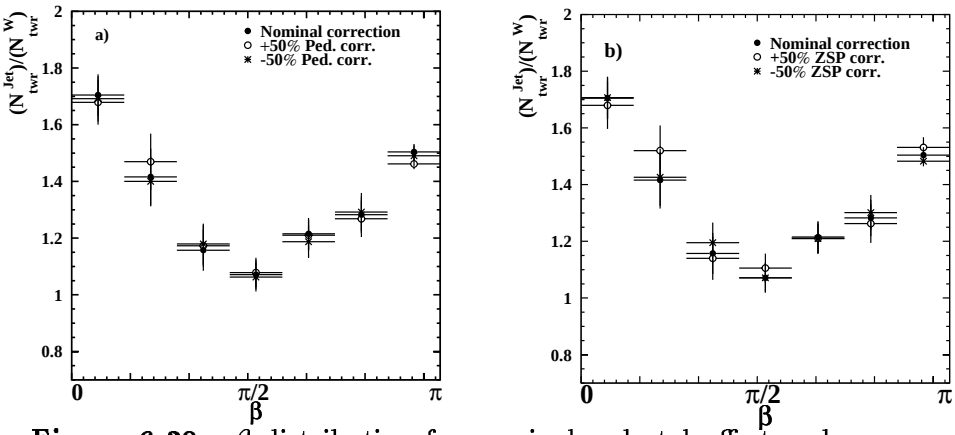

Figure 6.29. β distribution for nominal pedestal offset and zero suppression corrections compared with a)$\pm 50\%$ in the pedestal offset correction and b)$\pm 50\%$ in the zero suppression (ZSP) correction.

point fluctuations observed, but with the exception of the second bin, these are all quite small compared to the statistical errors, and no global shift in the pattern is demonstrable.

6.9.3 Calorimeter Response

The main concern here is that the calorimeter response is not uniform as a function of η (disregarding the regions with no EM coverage which have been removed).It is necessary to see how the η dependence of the response can affect the β measurement in both data and Monte Carlo.

Excepting the uninstrumented region, the Shower Library calorimeter response is flat to within $\pm 5\%$. This was determined by calculating the ratio

of tower energy to particle energy for the Shower Library events as a function of η. The response in data was determined with γ+1 jet and dijet events by measuring the E_T mismatch between the photon and jet (or the trigger jet and the other jet for dijet events) as a function of jet η[68]. The response there is also flat to within $\pm 5\%$. Corrective factors were applied to cell energies in Monte Carlo and data to reduce this to $\pm 1\%$ and new β distributions were measured. The multiplicative correction was derived by fitting the response curve as a function of η and multiplying the cell energies by the inverse of this function. The comparison of β patterns with and without the corrective factors indicates the sensitivity of the measurement to response fluctuations at the 5% level. Both comparisons (shown in Fig. 6.30a and Fig. 6.30b) show virtually

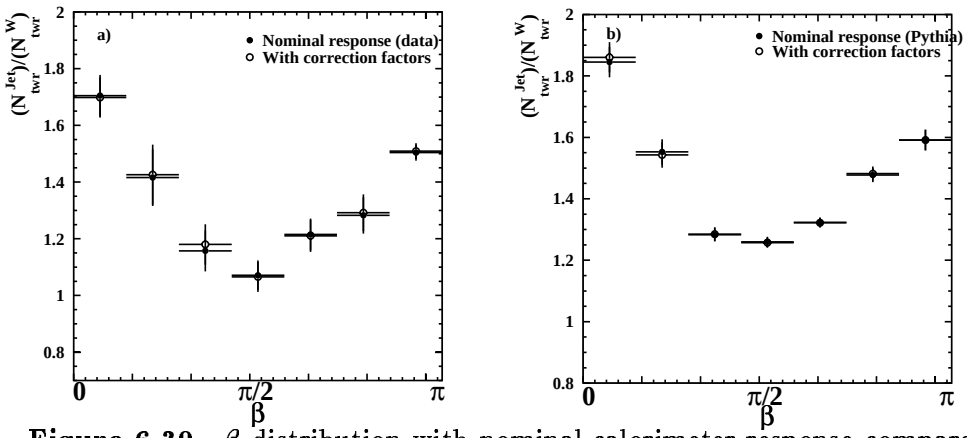

Figure 6.30. β distribution with nominal calorimeter response compared with distribution with corrective factors for a)Data and b)PYTHIA Sample I (Samples II and III give similar results).

no alteration in the β pattern, demonstrating the stability of the measurement with respect to changes in the calorimeter response for both data and PYTHIA.

6.9.4 Luminosity Dependence

The DØ multiple interaction tool (MI tool) is used to preferentially select events with only one interaction in an event. The use of this tool was described in Chapter 4. The MI tool assumedly has some efficiency associated with it which is unknown. Monte Carlo events would be needed to measure this efficiency, but at the present no known generator models minimum bias events accurately enough to perform this measurement. However, the assumption is that the MI tool is less effective at high luminosities because of the presence of more multiple interaction events, some small fraction of which will be flagged as single interaction events. The high luminosity events in the analysis sample are therefore susceptible to being misidentified as having a single interaction. Multiple interaction events are detrimental to this analysis because of the extra energy in them due to the additional scattering(s).

An easy way to check whether or not multiple interaction contamination affects the analysis is to split the sample into high and low luminosity halves and look for differences in the β measurements. The mean luminosity for the W+jets sample is 6.0, so the sample was split into one half with $\mathcal{L}>6\times10^{30}$ cm^{-2}s^{-1} and one half with $\mathcal{L}<6\times10^{30}$ cm^{-2}s^{-1}. The comparison of the two halves is shown in Fig. 6.31 below. The two halves of the sample have approximately the same number of events. Aside from a fluctuation in the next-to-last bin, the two distributions agree quite well.

To be sure that this comparison is not being driven by events in the vicinity of the mean, another comparison was made for events with $\mathcal{L}>8\times10^{30}$ cm^{-2}s^{-1} and $\mathcal{L}<5\times10^{30}$ cm^{-2}s^{-1}. The results can be seen in Fig. 6.32. This comparison bears strong resemblance with the comparison of Fig. 6.31, indi-

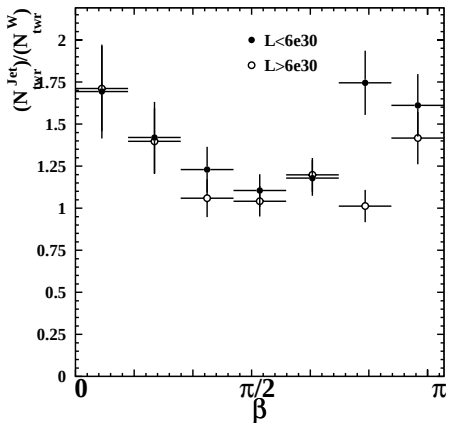

Figure 6.31. Dependence of the signal in data on event luminosity.

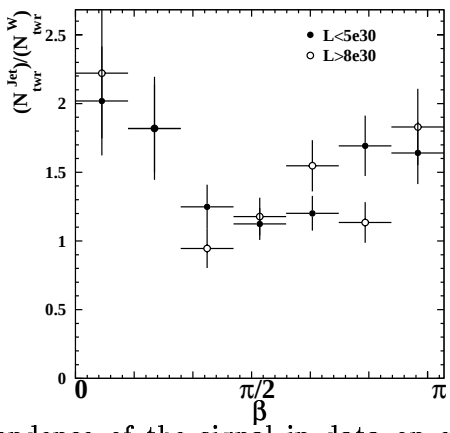

Figure 6.32. Dependence of the signal in data on event luminosity, second comparison.

cating no significant luminosity dependence in the data. It is worth noting that the event-plane regions in this comparison exhibit a higher ratio value than in the previous comparison or in the global analysis sample. A closer investigation of this effect revealed that a number events in the medium luminosity range (5-8$\times 10^{30}$cm^{-2}s^{-1}) exhibited more towers above threshold in the W boson annulus than in the jet annulus, counter to the color coherence assertion. However, these events were revealed to contain jets which strayed into the W boson region of the event. These jets were not the jets tagged for

the jet annulus, but rather additional jets present in the events. They thus contributed towers to the W boson annulus. Such events are present in the high and low luminosity samples, as well, but in smaller numbers. They exist in the PYTHIA events also.

Ideally, a sample with much greater statistics would be used to search for luminosity dependence. The low event count in the analysis sample makes it difficult to separate it into parts. There is one method available, however, which increases the statistics without altering the physics under study. Increasing the rapidity window for both the jet and the W boson to ± 0.7 from ± 0.5 roughly doubles the number of events, but does not alter the physics. This can be seen in Fig. 6.33a, in which the β pattern for the wider window is compared with the standard pattern. They agree quite well. The luminosity dependence

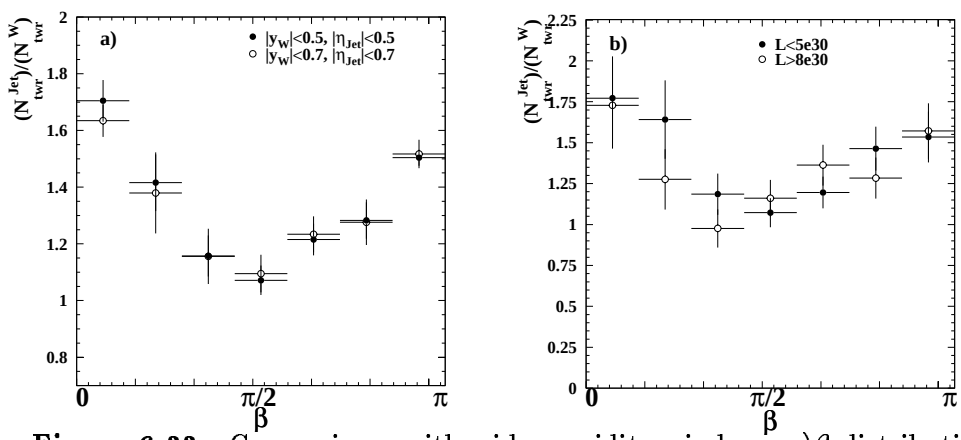

Figure 6.33. Comparisons with wider rapidity window. a)β distribution with rapidity window of ± 0.5 (closed circles) and ± 0.7 (open circles). b)Dependence of the signal on event luminosity for wider rapidity window.

in this larger sample is shown in Fig. 6.33b. The two curves agree very well, lending further evidence to the assertion that the signal is stable over a wide range of luminosities. Fluctuations between low and high luminosities (such as for the sixth bin in Fig. 6.31) are accounted for in the statistical errors.

6.9.5 *W Boson Rapidity*

The reconstruction of the W boson results in a twofold ambiguity in its rapidity. Monte Carlo events indicate that the solution with the smaller absolute rapidity is closer to the actual rapidity approximately 2/3 of the time. Since data and PYTHIA have the same electron and $\not\!\!E_T$ kinematics, this ratio is assumed to be valid for the data as well. The best way to investigate the effects of this choice is to compare with β distributions using the actual W boson rapidity. This is of course not possible in the collider data, so such an exercise with the PYTHIA samples would not be particularly useful. However, since the same strategy is used in data and in the three PYTHIA samples, no systematic bias is introduced in the analysis.

It is also important to recall that the W boson is used in this analysis only as a template against which the physics around the tagged jet is studied. Its location is thus used only to locate some "empty space" in the detector that is relatively free of hard scattering remnants. The ϕ coordinate of the W boson is mainly used for this purpose, since it defines the plane of the event and indicates where to look to find the opposing jet. The rapidity of the W boson, however, is useful only in that it helps define the center of the annular region within the rapidity limits (± 0.5). In reality, the β measurement should not be strongly correlated with this variable, since it does not determine the color flow in any way. Hence, rapidity fluctuations within the narrow window studied are not expected to alter the measurement in a meaningful way.

To study this, the analysis procedure was repeated on the data and PYTHIA samples I and II with the W boson annulus centered at a *random* location in rapidity, within the ± 0.5 window. The ϕ location from the W boson was

unchanged, as was the centroid of the jet annulus. Fig. 6.34 shows the results for data as compared with the standard method of calculating the W boson rapidity, while Figs. 6.35a and 6.35b show the same for PYTHIA. Deviations

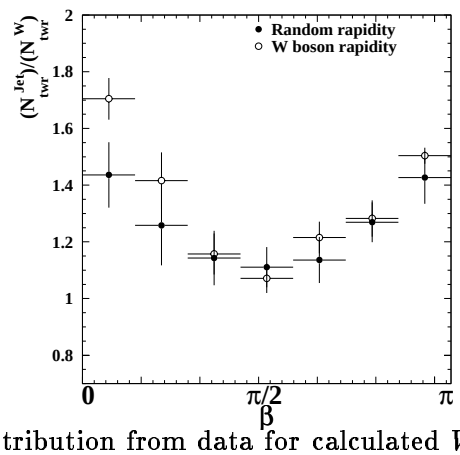

Figure 6.34. β distribution from data for calculated W boson rapidity (open circles) and random W boson rapidity (closed circles).

do appear in each of the comparisons, but the global shapes remain the same. The comparison of data with PYTHIA for this alternate method thus shows similar trends as the comparison with the standard method (see Figs. 6.36a and 6.36b). These comparisons stress that the data agree better with PYTHIA with

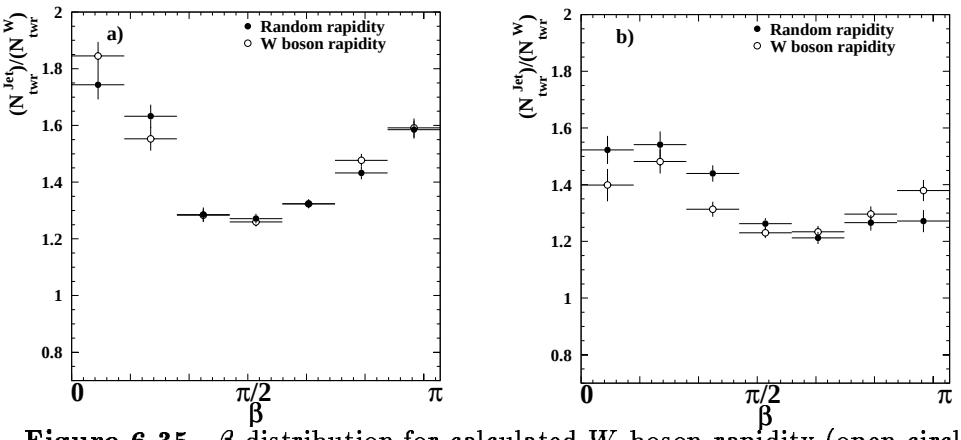

Figure 6.35. β distribution for calculated W boson rapidity (open circles) and random W boson rapidity (closed circles) from a)PYTHIA Sample I and b)PYTHIA Sample II.

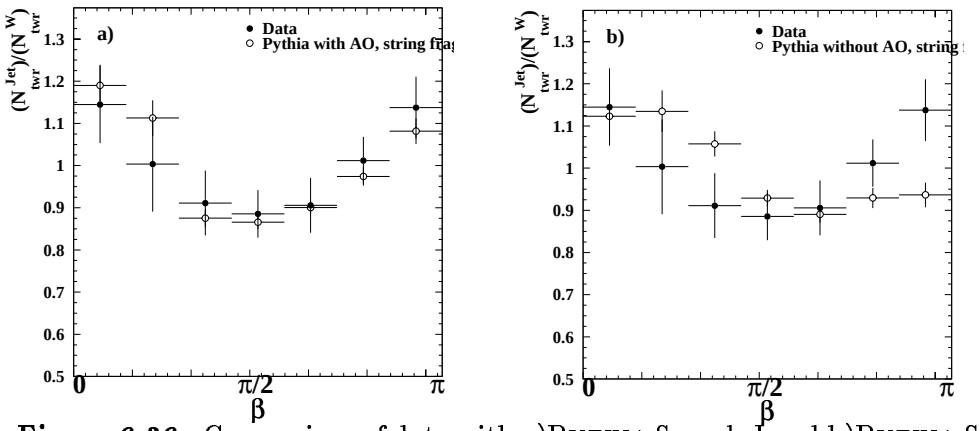

Figure 6.36. Comparison of data with a)PYTHIA Sample I and b)PYTHIA Sample II when the W boson rapidity is randomly generated.

coherent parton evolution and string fragmentation than string fragmentation alone regardless of the rapidity coordinate chosen for the W boson annulus (within the ± 0.5 window).

6.9.6 Summary of Systematics

Several potential sources of systematic uncertainty have been studied for this analysis. While some minor variations in the observed patterns is observed, none of the systematics alters the original comparisons of data with the PYTHIA simulations. In particular, some point-to-point variations are seen for some of the sources studied, but none demonstrates conclusively any systematic bias in the study.

CHAPTER 7

SUMMARY AND CONCLUSION

This dissertation represents the first attempt at studying color coherence effects in W+jets events, and the first attempt at studying non-perturbative contributions to particle distributions in hadronic collisions. Although this investigation is far from complete, sufficient progress has been made to report the current findings in a cohesive manner.

The distribution of energy in the calorimeter was measured in W+jets events as a means of observing the distribution of particles in these events. W+jets events were used so as to exploit the colorless nature of the W boson, which acts as an unbiased probe of the distribution of energy in the vicinity of the tagged jet. Towers with E_T>250 MeV were chosen to measure the energy distribution in the vicinity of both the W boson and tagged jet. The division of these distributions as a function of the angle β shows the topological features of the distribution of these energetic towers.

The DØ detector has proven an excellent facility for making such a measurement. The segmentation and resolution of the calorimeter has allowed for unambiguous discrimination of low–energy tower patterns. The low noise in the detector has also aided this discrimination. Additionally, the comprehensive trigger framework allowed for relatively quick identification of useful events.

The pattern seen in data was proven not to be the result of simple kine-

matics or detector effects. It further proved stable when subjected to various changes in detector response, uranium noise and pileup energy. The extremely tight selection cuts used to form the analysis sample resulted in low statistics, but virtually no background contamination as well.

The divisional β distribution was compared with three Monte Carlo W+jets event samples from the PYTHIA event simulator. One sample employed coherent parton evolution by means of angular ordering and azimuthal correlations in conjunction with the string model for fragmentation. The second employed incoherent parton evolution, but retained the string model for fragmentation. The third employed incoherent parton evolution and independent fragmentation, thus making no use of color connections among partons.

It is instructive to take another look at the comparisons of data with the three PYTHIA samples. A good way to highlight the comparisons is to divide the β distribution from data by that from each of the three simulations. Deviations from a flat line thus indicate the level of dissimilarity of the three with data. The "division of division" curves are shown in Fig. 7.1, Fig. 7.2, and Fig. 7.3.

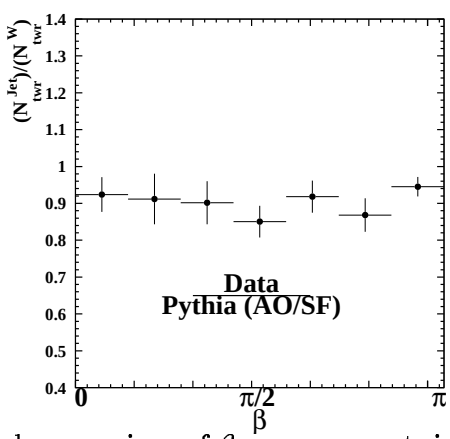

Figure 7.1. Divisional comparison of β measurements in data and PYTHIA with angular ordering (AO) and string fragmentation (SF).

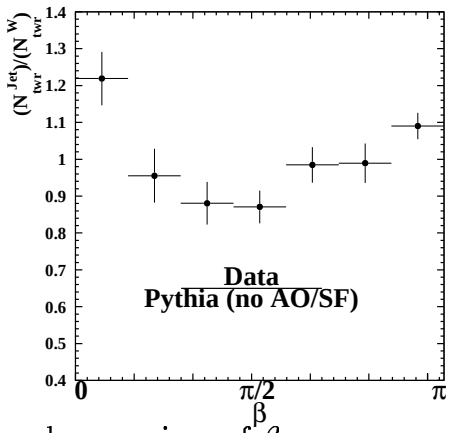

Figure 7.2. Divisional comparison of β measurements in data and PYTHIA without angular ordering, but with string fragmentation.

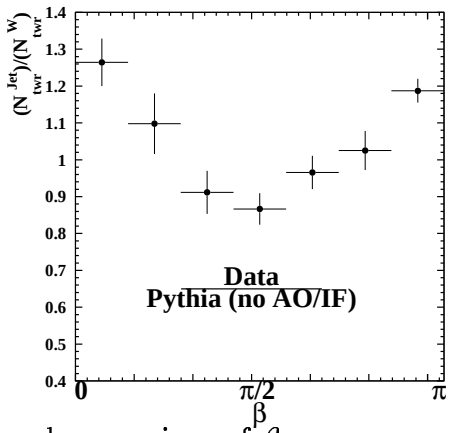

Figure 7.3. Divisional comparison of β measurements in data and PYTHIA without angular ordering and with independent fragmentation (IF).

The comparison of data with the first PYTHIA sample shows very good agreement. The other two show divergences. This is evidence that color coherence at the parton level, combined with string fragmentation, is consistent with DØ W+jets data as modelled by PYTHIA. In other words, the combination of interference effects in the perturbative and non-perturbative regimes is well-modelled by PYTHIA, and can reasonably describe the pattern of energy flow observed in W+jets data. The distribution of towers in PYTHIA was shown to adequately represent the distribution of energetic particles prior to detector

simulation. The agreement with data is indication that the β measurement in data is also representative of the pattern produced at the particle level.

By itself, string fragmentation appears incapable of reproducing the pattern observed in data, as shown in Fig. 7.2. The distribution in the second sample showed similar features in β, but the degree of transverse-plane depletion was less than was observed in the data. This leads to the conclusion that parton-level coherence appears to be important in the evolution from the scattering vertex, which is in keeping with the notion of Local Parton Hadron Duality. Disregard of the color connections among partons appears to have consequences on the particle distributions that string fragmentation alone cannot make up for.

Lastly, the third comparison indicates that color connections of some kind are needed to describe the data. Any pattern produced in this last sample would have been the product of factors other than interference effects, whether at the perturbative or non-perturbative levels. The lack of any significant pattern observed seems to show these factors are insufficient by themselves.

Some caveats are in order with regards to the conclusions just drawn. First, it is possible that lingering luminosity dependence exists in the data. Although there is no direct evidence for it, neither is there a measurement of the efficiency of the multiple interaction tool, which would answer the question. Also, better event statistics would improve the comparisons with Monte Carlo. Expanding the rapidity window has shown to be a possible technique in this area. Lastly, a fourth PYTHIA sample would round out this investigation into the perturbative contributions. A sample with coherent parton evolution and independent fragmentation would provide much information about Local Parton Hadron Duality.

In summary, this dissertation should be viewed as the first step into the rich topic of color coherence at hadronic colliders. There are many unexplored avenues even with W+jets events. For example, it would be interesting to determine if PYTHIA can produce varying β distributions for gluon and quark jets, and if these differences can be found in data. There are also other simulations yet to be compared with. The HERWIG leading-order generator is an obvious choice. It implements color coherence in much the same way as PYTHIA, but uses a different fragmentation scheme and has been shown to reproduce DØ multijet distributions well[20]. There is also ARIADNE, a leading-order simulator that uses a dipole approximation for color connections. Lastly, a next-to-leading order generator exists as well which should be able to model coherence effects.

With the upgrade of the DØ detector, it should be possible to perform this analysis with the superior tracking facilities that will be available. The next run should also provide a great increase in statistics for W+jets events, opening up new areas of study not possible with the current sample. In short, this dissertation has laid the groundwork for color coherence studies in hadronic collisions. It is the hope of the author that it will provide incentive for others to continue the work and to initiate new color coherence studies.

APPENDIX A

Useful Kinematic Quantities for W Bosons

The following are formulae for calculating kinematic quantities useful in the analysis of W boson events. Some are used directly in the color coherence analysis and some are used for consistency checks in the data.

A.1 Transverse Mass

$$M_T^W = \sqrt{2p_T^e p_T^\nu (1 - \cos(\Delta\phi))} \tag{A.1}$$

where

$$\Delta\phi = \phi_e - \phi_\nu \tag{A.2}$$

A.2 Transverse Momentum

$$p_T^W = \sqrt{(p_x^W)^2 + (p_x^W)^2} \tag{A.3}$$

where

$$\begin{aligned} p_x^W &= p_x^e + p_x^\nu \\ p_y^W &= p_y^e + p_y^\nu \end{aligned} \tag{A.4}$$

A.3 Azimuthal Angle

$$\phi_W = \arctan(\frac{p_x^W}{p_y^W}) \tag{A.5}$$

A.4 Rapidity

The calculation of the rapidity, y_W, is not as straightforward as the previous calculations. The expression for rapidity is

$$y_W = \ln(\frac{E_W + p_z^W}{E_W - p_z^W}) \tag{A.6}$$

where $E_W = \sqrt{p_W^2 + M_W^2}$ and $p_z^W = p_z^e + p_z^\nu$. However, as described in Sec. 4.2.3, p_z^ν is not a measurable quantity at DØ, thus complicating calculations for p_z^W and E_W.

Although p_z^ν cannot be measured, it can be calculated, with the help of a few reasonable assumptions, from the basic mass formula

$$\begin{aligned} M_W^2 &= (P_e + P_\nu)^2 \\ &= (E_e + E_\nu)^2 - (\vec{p_e} + \vec{p_\nu})^2 \end{aligned} \tag{A.7}$$

where P_e and P_ν are the electron and neutrino 4-momenta, respectively. The first assumption to be made is that M_W is a known constant. This is reasonable since the world average of $M_W = (80.22 \pm 0.26)$ GeV is well-measured and since small mass differences are inconsequential to this analysis. This leaves p_z^ν as the only unknown in the equation. With the further assumption that $E_e \simeq p_E$, this expression can be evaluated (with a bit of algebra) to

$$[p_T^e]^2(p_z^\nu)^2 + [-2(\frac{M_W^2}{2} + p_x^e p_x^\nu + p_y^e p_y^\nu)p_z^e]p_z^\nu + [E_e^2 \not{E}_T{}^2 - (\frac{M_W^2}{2} + p_x^e p_x^\nu + p_y^e p_y^\nu)^2] = 0 \tag{A.8}$$

which is quadratic in p_z^ν. The solution for p_z^ν, then, is

$$p_z^\nu = \frac{2Xp_z^e \pm \sqrt{(-2Xp_z^e)^2 - 4(p_T^e)^2(E_e^2 \not{E}_T^{\ 2} - X^2)}}{2(p_T^e)^2} \tag{A.9}$$

where

$$X = \frac{M_W^2}{2} + p_x^e p_x^\nu + p_y^e p_y^\nu \tag{A.10}$$

This results in two solutions for p_z^ν and, therefore, a twofold ambiguity in y_W, the W rapidity.

APPENDIX B

A Sample W+jets Event in the Detector

The following three pictures show what a good W+jets event looks like in the detector. The first picture shows the central tracker and calorimeter from the side. There are several tracks emanating from the event vertex in this event, but more interesting to observe is the calorimeter depositions. The top cluster is the deposition from the high-p_T decay electron. All of the energy is seen to be concentrated in the electromagnetic layers of the central calorimeter (as expected for true electrons). On the other side of the event is the jet energy cluster. It reaches from the electromagnetic layers to the outermost coarse hadronic layer. All of the filled regions in this plot represent energy depositions of at least one GeV (the key indicates the energy of each cell). This particular event has several associated with the jet, so this jet is quite energetic for a W boson event.

The second figure shows the calorimeter and central tracking chambers from the end view of the detector. This figure shows the dispersion in azimuthal angle ϕ of the calorimeter energy (η direction is perpendicular to page). The jet is represented by the localized cluster of hadronic and electromagnetic energy, while the electron energy is concentrated in a single slice of mostly electromagnetic energy. In this view, it is also possible to show the location in ϕ of the $\not\!\!E_T$ vector, shown as a thin spike in the plot. Note that the jet, electron, and

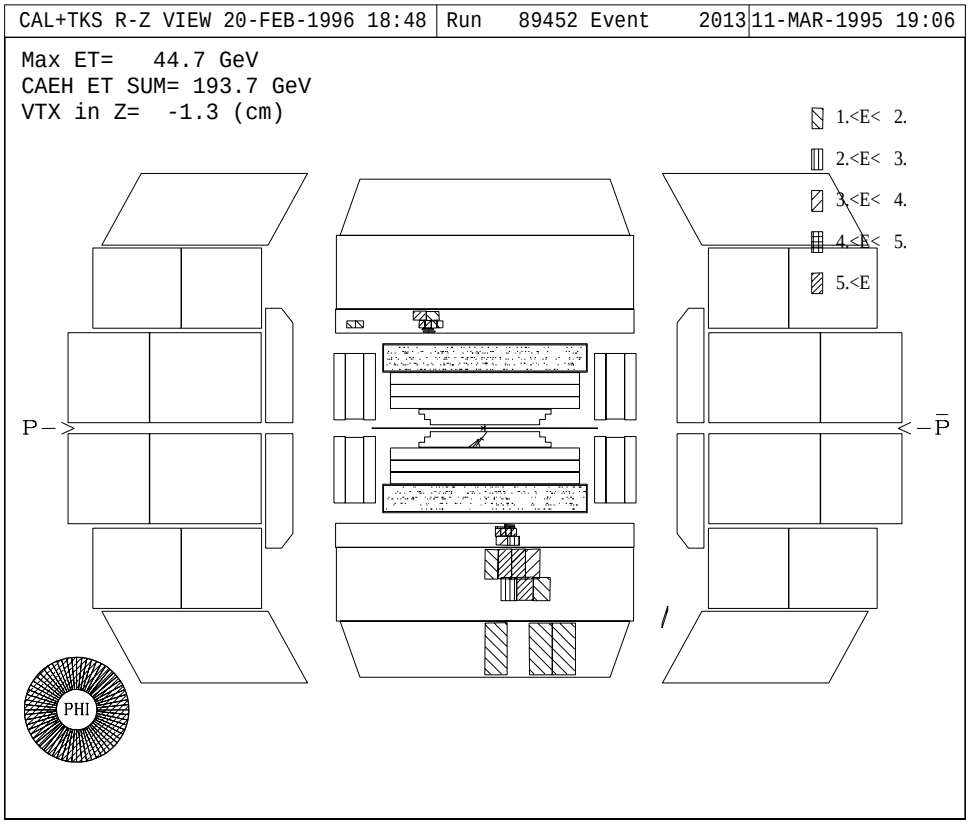

Figure B.1. Side view of event.

$\not{E}_T$ are all approximately equidistant in ϕ. The W boson thus reconstructed from the electron and $\not{E}_T$ is thus almost exactly back-to-back in ϕ with the jet.

Fig B.3 shows the calorimeter unfolded into an (η,ϕ) plane. All towers with at least 200MeV of energy are shown. The jet and electron clusters are clear in this projection. The other towers in the event are due to wide-angle scattering from the hard interaction, spectator interactions, and calorimeter noise.

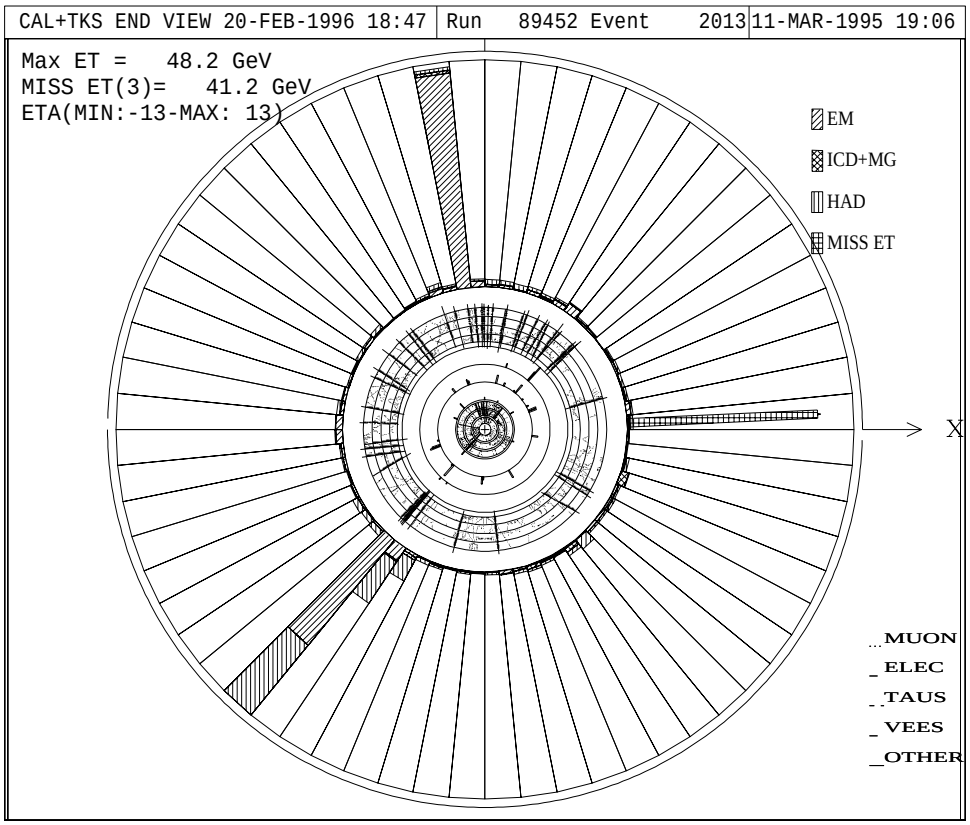

Figure B.2. End view of event.

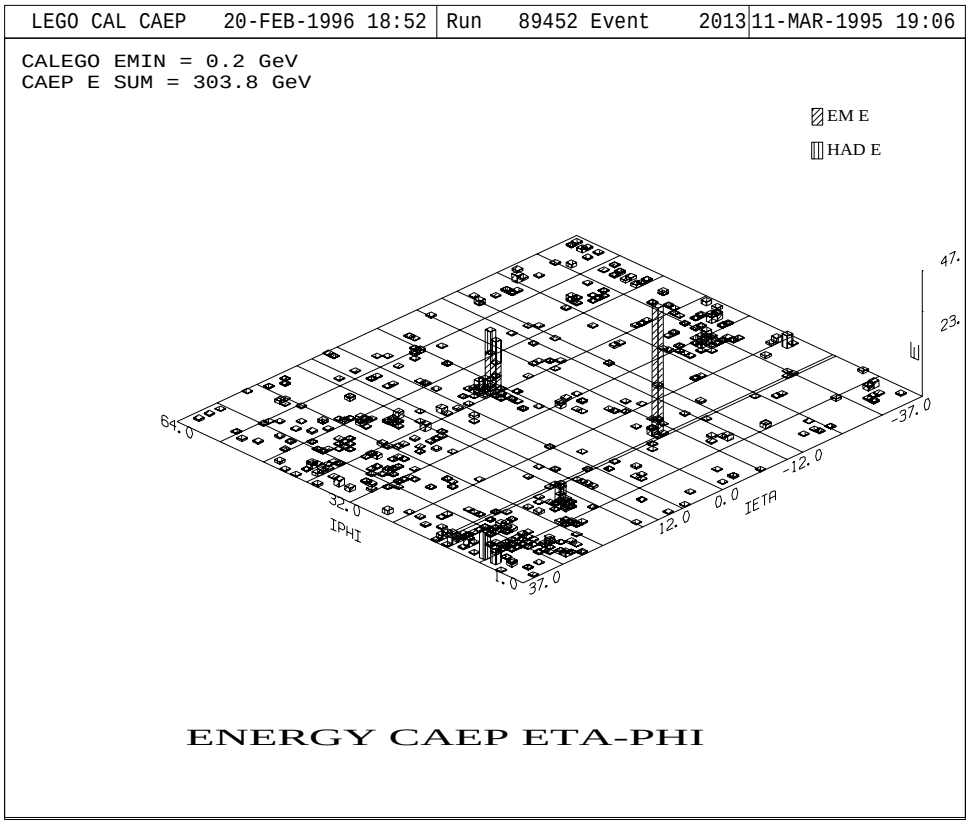

Figure B.3. Calorimeter towers in (η,ϕ) plane.

APPENDIX C

Post-Mortem Analysis

Although the case for color coherence in the data has been made already through the course of this dissertation, the expansion of the rapidity window from ± 0.5 to ± 0.7 (discussed in Chapter 6 for the luminosity dependence) is a viable extension of the analysis that worth considering here. The event sample is substantially increased (to 390 events) while the physics distributions in the data appear to remain statistically unchanged. Therefore, it is worthwhile to revisit the comparisons of the W+jets data with the three PYTHIA simulations. An additional comparison with minimum bias data is also possible with the expanded window.

C.1 Comparison of Data and PYTHIA

The analysis procedure was repeated for all four W+jets samples (data and three PYTHIAsamples) with the rapidity window increased to ± 0.7. Figs. C.1-C.3 show the comparisons of PYTHIA with data. In all plots, the closed circles represent the collider data and open circles represent the PYTHIA samples. All errors are statistical. These comparisons reveal the same features as was seen in Figs. 6.21- 6.23 — the PYTHIA simulation with coherent parton evolution and string fragmentation agrees well with data, while the other two simulations are disfavored. The improved statistics therefore augment the analysis performed

with the narrower rapidity window and demonstrate the stability of the signal for more forward objects.

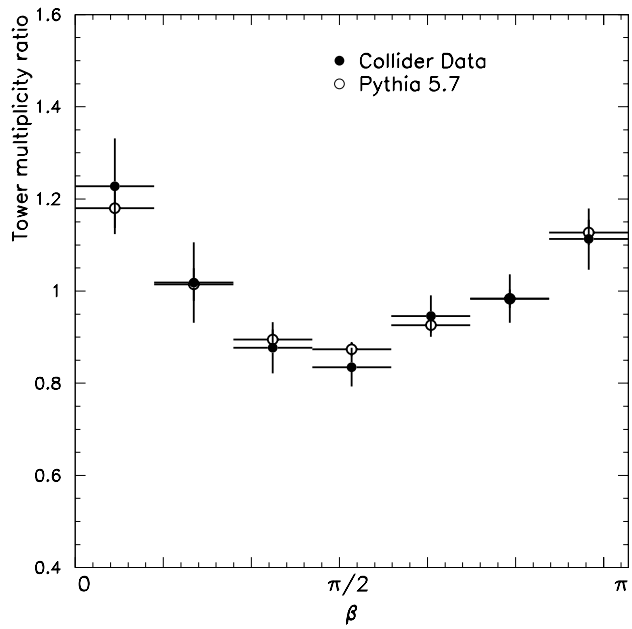

Figure C.1. Comparison of normalized β distributions for data and PYTHIA Sample I (angular ordering and string fragmentation) for the wider rapidity window.

C.2 Minimum Bias Dijet Events

Minimum bias events with two or more reconstructed jets provide a means of comparing the W+jets signal with one in which the W boson is replaced by a jet. It thus probes the assumption that the presence of the W boson results in real variations in tower multiplicity in the W+jets events. Jets in minimum bias events have similar E_T ranges as the W+jets events and are not subject to trigger biases. The expansion of the rapidity window allows this comparison to be made, as insufficient statistics exist for the minimum bias dijet sample with the previous window.

Events for this comparison were selected with the following criteria:

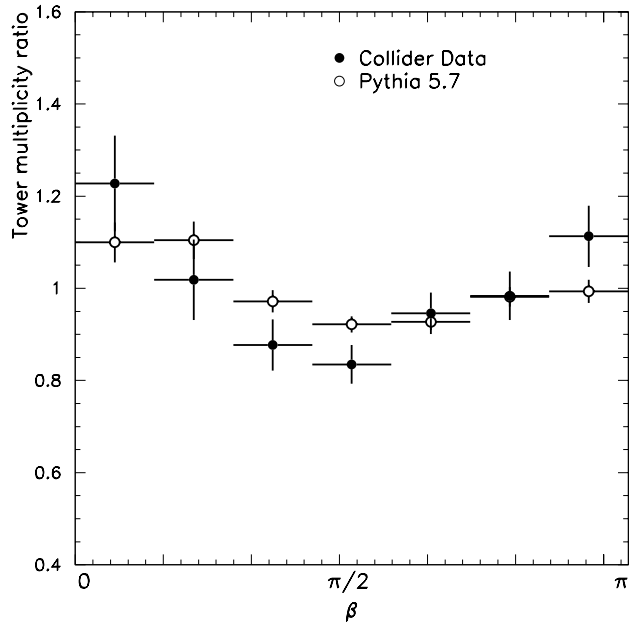

Figure C.2. Comparison of normalized β distributions for data and PYTHIA Sample II (no angular ordering, but with string fragmentation) for the wider rapidity window.

- Multiple Interaction Flag = 1
- Main Ring E_T>-10 GeV
- $\mid z_{vtx} \mid$<20 cm
- $\geq$2 reconstructed jets
- $E_{T\,Jet1}$ >10 GeV and $E_{T\,Jet2}$ >10 GeV
- $\mid \eta_{Jet1} \mid$<0.7 and $\mid \eta_{Jet2} \mid$<0.7
- $\pi/2 < Delta\phi_{Jet1,Jet2} < 3\pi/2$
- Quality cuts for *all* jets in event

In the above list, Jet1 and Jet2 refer to the first and second jets in the event, ordered in descending E_T. Pedestal offset and zero suppression corrections

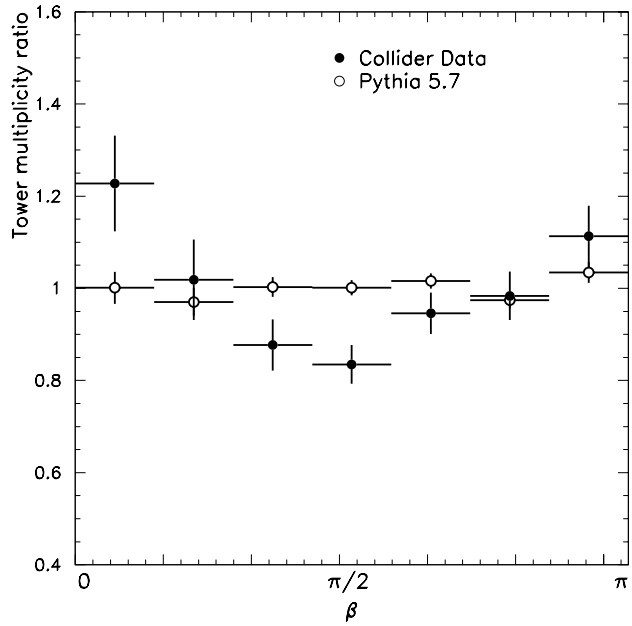

Figure C.3. Comparison of normalized β distributions for data and PYTHIA Sample III (no angular ordering and independent fragmentation) for the wider rapidity window.

were applied to all events.

For these events, the two leading-E_T jets are used for the annuli. The location for Jet 1 is used for the "W boson" annulus and the location for Jet 2 is used for the "tagged jet" annulus. This choice is motivated by the observation that, in W+jets events, the W boson p_T is generally greater than the tagged jet E_T.

The analysis procedure is then used for these events as if they were real W+jets events. The resulting divisional β distribution for the minimum bias dijet events is compared with the W+jets distribution in Fig. C.4. Within statistical errors, the β pattern for the minimum bias dijet data is uniformly flat with ratio values of $\simeq$1.0, similar to the minimum bias pattern with no jets. This is further evidence that there is a real effect in the W+jets data, and demonstrates that there is a substantial difference in the distribution of towers

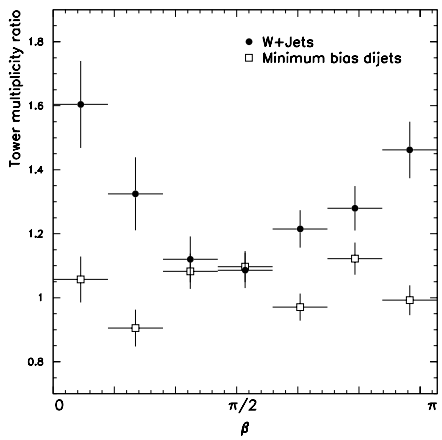

Figure C.4. Divisional β distribution for W+jets data (closed circles) as compared to minimum bias dijet data (open squares).

when a non-emitting W boson opposes the tagged jet rather than another jet.

BIBLIOGRAPHY

[1] M. Gell-Mann and Y. Ne'eman,"The Eightfold Way," Benjamin, 1964.

[2] V. E. Barnes *et al.*, Phys. Rev. Lett. 12, 204 (1964)

[3] M. Gell-Mann, Phys. Lett. 8, 214 (1964)

[4] G. Zwieg, CERN Report 8182/Th. 401 (1964)

[5] J. J. Aubert *et al.*, Phys. Rev. Lett. 33, 1404 (1974)

[6] J. Augustin *et al.*, Phys. Rev. Lett. 33, 1406 (1974)

[7] B. J. Bjorken and S. L. Glashow, Phys. Lett. 11, 255 (1964)

[8] M. Perl *et al.*, Phys. Rev. Lett. 35, 1489 (1975)

[9] G. Arnison *et al.*, Phys. Lett. 122B, 103 (1983)

[10] G. Arnison *et al.*, Phys. Lett. 126B, 398 (1983)

[11] S. Abachi *et al.*, Phys. Rev. Lett. 74, 2632 (1995)

[12] F. Abe *et al.*, Phys. Rev. Lett. 74, 2626 (1995)

[13] O. Greenberg, Phys. Rev. Lett. 13, 598 (1964)

[14] C. Quigg, "Gauge Theories of the Strong, Weak, and Electromagnetic Forces", Addison-Wesley, 1983.

[15] A. Browman *et al.*, Phys. Rev. Lett. 33, 1499 (1974)

[16] D. Griffiths, "Introduction to Elementary Particles", John Wiley and Sons, Inc., 1987.

[17] F. Halzen and A. Martin, "Quarks and Leptons: An Introductory Course in Modern Particle Physics", John Wiley and Sons, Inc., 1984.

[18] Y. Doskshitzer *et al.*, Columbia Univ. Th. Phys., 374, 1987

[19] W. Bartel *et al.* (JADE Collaboration), Phys. Lett. B101, 129 (1981); Zeit. Phys. C21, 37 (1983); Phys. Lett. B134, 275 (1984). H. Aihara *et al.* (TPC/2γ Collaboration), Phys. Rev. Lett. 54, 270 (1985); Zeit. Phys. C28, 31 (1985); Phys. Rev. Lett. 57, 945 (1986). M. Althoff *et al.* (TASSO Collaboration), Zeit. Phys. C29, 29 (1985). P.D. Sheldon *et al.* (MARK2 Collaboration), Phys. Rev. Lett. 57, 1398 (1986). M.Z. Akrawy *et al.* (OPAL Collaboration), Phys. Lett. B247, 617 (1990); Phys. Lett. B261, 334 (1991); P.D. Acton *et al.* Phys. Lett. B287, 401 (1992); Zeit. Phys. C58, 207 (1993). M. Acciarri *et al.* (L3 Collaboration), Phys. Lett. B352 487 (1995).

[20] S. Abachi *et al.*, Fermilab Conf-95/182-E, 1995.

[21] F. Abe *et al.*, Phys. Rev. D50, 5562 (1994).

[22] W.T. Giele, N. Glover, and D.A. Kosower, Phys. Rev. D46, 461 (1992); Phys. Rev. Lett. 73, 2019 (1994).

[23] G. Marchesini and B.R. Webber, Nucl. Phys. **B310**, 461 (1988).

[24] H.-U. Bengtsson and T. Sjöstrand, Computer Physics Commun. **46** (1987) 43.

[25] F.E. Paige and S.D. Protopopescu, BNL report No. 38034 (1986).

[26] R.K. Ellis, G. Marchesini, B.R. Webber, Nuc. Phys. B286, 643 (1987)

[27] F. Fiorani, G. Marchesini, L. Reina, Nuc. Phys. B309, 439 (1988)

[28] G. Marchesini, B.R. Webber, Nuc. Phys. B310, 461 (1988)

[29] A. Bassetto, M. Ciafaloni, G. Marchesini, Phys. Rep. 100, 202 (1983)

[30] Y. Doskshitzer *et al.*, "Basics of Perturbative QCD", Editions Frontieres, 1991.

[31] T. Sjöstrand, Phys. Lett. B157, 321 (1995); M. Bengtsson, T. Sjöstrand, and M. van Zijl, Z. Phys. C32, 164 (1986).

[32] B.R. Webber, Ann. Rev. Nucl. Part. Sci. 36, 253 (1986).

[33] B. Andersson, G. Gustafson, B. Söderberg, Z. Phys. C20, 317 (1983).

[34] B.R. Webber, Nucl. Phys. B238, 492 (1984); T. D. Gottschalk, Nucl. Phys. B239, 325 (1984).

[35] A. Krzywicki, B. Petersson, Phys. Rev. D6, 924 (1972); J. Finnkelstein, R.D. Peccei, Phys. Rev. D6, 2606 (1972)

[36] Torbjörn Sjöstrand, Int. J. Mod. Phys. A3, 751 (1988).

[37] Torbjörn Sjöstrand, CERN-Th.7112/93 (1993)

[38] P. Edén, Lund Th. Phys. 96-20, 1 (1996).

[39] A. Ali *et al.*, Nucl. Phys. B168, 409 (1980).

[40] G. Altarelli, G. Parisi, Nucl. Phys. B126, 298 (1977).

[41] Torbjörn Sjöstrand, private communication.

[42] J. Thompson, *Introduction to Colliding Beams at Fermilab*, Fermilab-TM-1909 (1994).

[43] L. Lederman, *The Tevatron*, Scientific American, March 1991.

[44] S. Abachi *et al.*, Nucl. Intr. Methods A338, 185 (1994).

[45] A.R. Clark *et al.*, Nucl. Intr. Methods A279, 243 (1989).

[46] A.R. Clark *et al.*, Nucl. Intr. Methods A315, 243 (1992).

[47] S. Snyder, *The DØ Detector*, DØ internal publication # 2500, March 1995.

[48] J.F. Detoeuf *et al.*, Nucl. Intr. Methods A279, 310 (1989).

[49] M. Abolins *et al.*, Nucl. Intr. Methods A280, 36 (1989).

[50] D.G. Coyne *et al.*, Phys. Rev. D50, 1261 (1994).

[51] C. Brown, *et al.*, Nucl. Intr. Methods A279, 331 (1989).

[52] G. Eppley, *Multiple Interactions, a Primer*, DØ internal publication # 1856, August 1993.

[53] S. Abachi *et al.*, Phys. Rev. Lett. 75, 1456 (1995).

[54] B. Abbott, *Jet Transverse Energy Shape in $\overline{p}p$ Collisions at sqrts=1.8TeV*, Ph.D. thesis (1994).

[55] M. Aguilar-Benitez *et al.*, Phys. Rev. D50, 1352 (1994).

[56] J. Butler, *Main Ring Deadtime*, DØ internal publication # 1682, February 1993.

[57] M. Bhattacharjee, D. Elvira, G. Blazey, *Efficiencies of the Standard Jet Cuts for Cone Sizes: 0.3, 0.5, 0.7*, DØ internal publication # 2197, July 1994.

[58] M. Narain, *Electron Identification in the DØ Detector*, DØ internal publication # 1548, January 1993.

[59] V. Balamurali, *Search for the Top Quark in the Dielectron Channel in $\overline{p}p$ Collisions at sqrts=1.8TeV*, Ph.D. thesis (1994).

[60] J. Yang, *Acceptance for $W \rightarrow e\nu$ and $Z \rightarrow ee$ at DØ*, DØ internal publication # 2317, November 1994.

[61] J. Bantly *et al.*, *Improvement to the DØ Luminosity Monitor Constant*, Fermilab-TM-1930 (1995).

[62] W. Carvalho and T. Taylor, *Multiple Interaction Tool Study for Run 1B*, DØ internal publication # 2798, December 1995.

[63] M. Kelly, *Test of the Standard Model of Electroweak Interactions by Measuring the Anomolous $WW\gamma$ Couplings at sqrts=1.8TeV*, Ph.D. thesis (1996).

[64] N. Graf, private communication.

[65] W. Dharmaratna, R.Raja and C. Stewart, *The DØ Shower Library – Version 2.0*, DØ internal publication # 1730, May 1993.

[66] S. Abachi *et al.*, *A Measurement of the Rato of $W+1$ Jet to $W+0$ Jet Cross Sections and Comparisons to QCD*, Contributted paper to the 28th Int. Conf. on High Energy Physics, July 1996.

[67] T. Joffe-Minor, private communication.

[68] R. Astur and R. Kehoe, *Determination of the Hadronic Energy Scale of DØ Calorimetry*, DØ internal publication # 2908, May 1996.